

**ENGINEERING GENETICALLY ENCODED BIOSENSORS FOR
QUANTIFYING CELLULAR DYNAMICS**

by

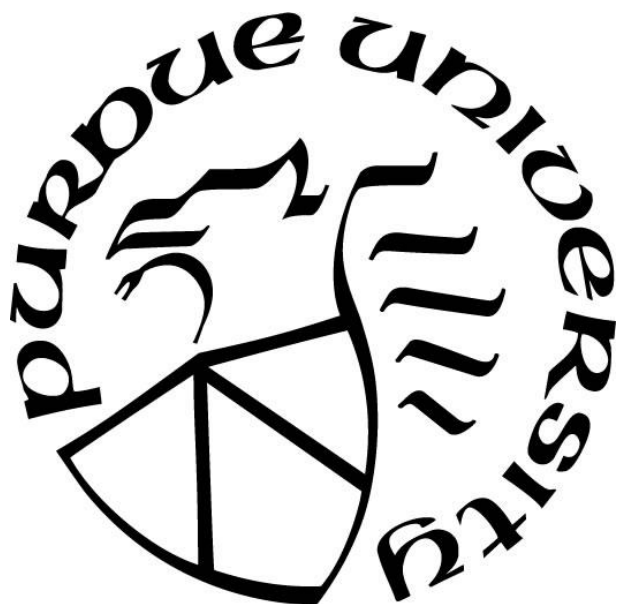
Emily Patten Haynes

A Dissertation

Submitted to the Faculty of Purdue University

In Partial Fulfillment of the Requirements for the degree of

Doctor of Philosophy



Department of Chemistry, Purdue University

West Lafayette, Indiana

August 2019

THE PURDUE UNIVERSITY GRADUATE SCHOOL
STATEMENT OF COMMITTEE APPROVAL

Dr. Mathew Tantama, Chair

Department of Chemistry

Dr. Chittaranjan Das

Department of Chemistry

Dr. Hilkka Kenttämää

Department of Chemistry

Dr. Angeline Lyon

Department of Chemistry

Approved by:

Dr. Christine Hrycyna

Head of the Graduate Program

For Megha Rajendran, Emily Denton, and Rachel Rieke

TABLE OF CONTENTS

LIST OF TABLES	8
LIST OF FIGURES	9
ABSTRACT	12
CHAPTER 1. INTRODUCTION	13
1.1 Fluorescent proteins are biologically compatible sensors	13
1.2 Sensor Designs	14
1.3 Red fluorescent proteins	16
1.4 pH	16
1.5 Red fluorescent proteins to quantify pH <i>in vivo</i>	16
1.6 Receptor trafficking and regulation	17
1.7 Luminescence resonance energy transfer (LRET) for increased signal to background.	18
1.8 Conclusion	19
1.9 References	21
CHAPTER 2. IMAGING PH DYNAMICS SIMULTANEOUSLY IN TWO CELLULAR COMPARTMENTS USING A RATIOMETRIC PH-SENSITIVE MUTANT OF MCHERRY	25
2.1 Introduction	25
2.2 Methods	26
2.2.1 Materials	26
2.2.2 Molecular Biology	27
2.2.3 Protein Expression and Purification	27
2.2.4 Steady-State Fluorescence Spectroscopy	27
2.2.5 Cell Culture and Transfections	28
2.2.6 Neuron and Astrocyte Cultures	28
2.2.7 Coefficient (ϵ) and Quantum Yield (QY)	28
2.2.8 Sensor Characterization in Live Cells	28
2.2.9 Live-Cell Imaging	29
2.2.10 Data Analysis	30
2.3 Results	30
2.3.1 Characterization of mCherryEA as a ratiometric pH sensor	30

2.3.2	Live-Cell Ratiometric Imaging	34
2.3.3	Live-Cell pH Calibration.....	38
2.3.4	Neuronal activity-dependent pH dynamics	44
2.3.5	Metabolism-dependent pH dynamics	49
2.4	Discussion and Conclusion.....	54
2.5	References	56
CHAPTER 3. QUANTIFYING ACUTE FUEL AND RESPIRATION DEPENDENT PH HOMEOSTASIS IN LIVE CELLS USING THE MCHERRY MUTANT AS A FLUORESCENCE LIFETIME SENSOR		
61		
3.1	Introduction	61
3.2	Methods	63
3.2.1	Materials	63
3.2.2	Molecular Biology.....	63
3.2.3	Protein Expression and Purification	63
3.2.4	Steady-State Fluorescence Spectroscopy	64
3.2.5	Crystallization	64
3.2.6	Time-Resolved Spectroscopy with Purified Protein	65
3.2.7	Time-Resolved Spectroscopy with Live Cell Suspensions	65
3.2.8	Mammalian Cell Culture, Transfection, and Live-Cell Imaging	66
3.3	Results	66
3.3.1	Structural analysis of mCherryTYG.....	66
3.4	mCherryTYG is a fluorescence lifetime pH sensor	74
3.4.1	Live-Cell Lifetime Spectroscopy	80
3.5	Multicolor Live-Cell Lifetime Spectroscopy.	84
3.6	Conclusions	91
3.7	References	91
CHAPTER 4. TOWARDS THE DEVELOPMENT OF A RECEPTOR INTERNALIZATION ASSAY WITH PH-SENSITIVE FLUORESCENT PROTEINS		
98		
4.1	Introduction	98
4.1.1	Receptor trafficking and regulation.....	98
4.1.2	Glucose Transporter (GLUT) 4: Trafficking and role in neurodegeneration.....	98

4.1.3	Utilizing the SpyTag/SpyCatcher platform for monitoring receptor internalization ..	100
4.2	Materials and Methods	101
4.2.1	Molecular Biology.....	101
4.2.2	SpyCatcher protein production and purification	102
4.2.3	Steady-State Fluorescence Spectroscopy	103
4.2.4	Mammalian Cell Culture, Transfection, and Live-Cell Imaging	103
4.3	Results	103
4.3.1	Engineering SpyTag-GLUT4 for labeling with pH sensitive fluorescent protein fusion SpyCatcher-pHluorin2	104
4.3.2	Purinergic P2Y receptors and GPCR signaling control	107
4.3.3	Engineering a SpyTag-P2YR11 for labeling with pH sensitive fluorescent protein SpyCatcher fusions	108
4.4	Conclusions and Future Directions	110
	References.....	111
CHAPTER 5. APPLYING LANTHANIDE BINDING TAGS TO ENABLE THE USE OF FLUORESCENT PROTEIN SENSORS IN TR-LRET ASSAYS.....		114
5.1	Lanthanides as LRET donors	114
5.2	Protein kinase A (PKA) in GPCR signaling cascades.....	117
5.3	AKAR2-CR is a well-studied PKA sensor.....	118
5.4	Engineering an LRET-AKAR2CR luminescent indicator for PKA activity.....	119
5.5	Methods	119
5.5.1	Materials	119
5.5.2	Molecular Biology.....	119
5.5.3	Protein expression and purification.....	120
5.5.4	LBT-eGFP Time-Resolved Luminescence Assays	121
5.5.5	AKAR2-CR PKA Assay	121
5.6	Results	122
5.6.1	LBT-eGFP as a TR-LRET model system	122
5.7	LBT-AKARCR as proof-of-concept	126
5.8	Conclusions	129

5.9	References	130
-----	------------------	-----

LIST OF TABLES

Table 1 Engineered Sensors and Advantages	20
Table 2 Data collection and refinement statistics	69
Table 3 Fitted fluorescence lifetime decay components for the purified protein pH calibration .	78
Table 4 Fitted fluorescence lifetime decay components for the pH-clamped E. coli calibration .	78
Table 5 Steady-state properties of fluorescent proteins.....	78
Table 6 LBT FP Primer Design	120
Table 7 LBT AKAR2CR construct design	127

LIST OF FIGURES

Figure 1 Green Fluorescent Protein (GFP) shows the canonical protein scaffold.....	13
Figure 2 Fluorescent protein sensors can be broadly categorized three ways.	15
Figure 3 Characterization of purified mCherryEA in solution.	31
Figure 4 Further characterization of purified mCherryEA in solution	33
Figure 5 mCherryEA reports live-cell pH changes in different cell types	34
Figure 6 Characterization of mCherryEA in live cells	35
Figure 7 mCherryEA expression in HEK-293 cells and primary astrocytes	37
Figure 8 <i>In situ</i> pH calibration of mCherryEA in the cytosol and mitochondria live cells	39
Figure 9 pH titration time course in Neuro2A cells.....	40
Figure 10 pH calibration in Neuro2A cells.....	41
Figure 11 Additional example images demonstrating colocalization of mito-mCherryEA and MitoTracker Deep Red to confirm proper mitochondrial targeting of mito-mCherryEA	42
Figure 12 Activity-dependent pH changes in neurons.....	46
Figure 13 Example of single-cell responses for Figure 8B.....	47
Figure 14 Individual single-cell traces for hippocampal neurons co-expressing mCherryEA in cytosol and ratiometric-pHluorin in mitochondria that were averaged in Figure 8D.....	48
Figure 15 Confocal microscopy	49
Figure 16 Metabolic inhibition causes differential acidification in the cytosol versus mitochondria	51
Figure 17 Representative images showing 60X oil magnification of Neuro2A cells.....	52
Figure 18 The X-ray crystal structure of mCherryTYG (PDB 6M3Z).....	70
Figure 19 Structural comparison between mCherryTYG, wildtype mCherry, and wildtype mOrange.....	71
Figure 20 Steady-state fluorescence spectroscopy characterization of mCherryTYG	72
Figure 21 mCherryTYG exhibits efficient maturation to the red fluorescent form.....	73

Figure 22 pH-dependent fluorescence lifetime of mCherryTYG	77
Figure 23 Fluorescence lifetime decay time constants	79
Figure 24 Fluorescence lifetime is independent of scatter and total intensity in live cell suspensions	79
Figure 25 Fuel and respiration-dependent pH homeostasis	82
Figure 26 Live-cell time-resolved spectroscopy on E. coli suspensions	83
Figure 27 Acute changes in respiration regulates intracellular ATP	86
Figure 28 Non-binding ATeamYEMK mutant controls	87
Figure 29 Simultaneous two-color live-cell lifetime measurements directly correlate intracellular pH and ATP levels	88
Figure 30 Simultaneous measurement of the extracellular and intracellular pH.....	88
Figure 31 Simultaneous two-color live-cell lifetime measurements directly correlate intracellular pH and ATP levels	89
Figure 32 Simultaneous two-color live-cell lifetime measurements directly correlate intracellular pH and extracellular pH	90
Figure 33 SpyTag-SpyCatcher chemistry	101
Figure 34 SpyCatcher-pHluorin fusion retains characteristic pH response <i>in vitro</i>	104
Figure 35 SpyTag-GLUT4-mCherry expression in HEK293a cells.....	106
Figure 36 Zoom in of SpyTag-GLUT4-mCherry/SpyCatcher-ELP-pHluorin2 overlay	106
Figure 37 SpyCatcher staining of SpyTag-P2YR11 in HEK293a cells	109
Figure 38 The ‘antennae’ effect. Lanthanide binding tags (LBTs) containing tryptophan residues act as lanthanide antennas, effectively transferring irradiated light to the metal ion	115
Figure 39 Lanthanide-sensitized luminescence	117
Figure 40 Reporting of PKA activity is possible using the AKAR2-CR FRET sensor	118
Figure 41 Schematic of LBT-eGFP constructs. We successfully tagged sLBT on the N, C and combined of eGFP, as well as a double lanthanide tag dLBT on the N-terminus of eGFP	123
Figure 42 LBT-eGFP gated luminescence.....	124

Figure 43 LBT-eGFP <i>in vitro</i> testing	124
Figure 44 sLBTa-eGFP off-rates after addition of lanthanide chelator DTPA	125
Figure 45 LBT-Tb ³⁺ as a FRET donor	127
Figure 46 In vitro PKA assay with purified wild-type AKAR2-CR FRET sensor	128
Figure 47 Wild type AKAR2CR LRET in Tris buffer	128
Figure 48 AKAR2-sLBTaCR LRET in Tris buffer	129

ABSTRACT

Author: Haynes, Emily, P. PhD

Institution: Purdue University

Degree Received: August 2019

Title: Engineering Genetically Encoded Biosensors for Quantifying Cellular Dynamics

Committee Chair: Mathew Tantama, PhD.

Live-cell imaging with fluorescent protein-based sensors allows us to monitor many dynamic changes *in situ*. The first genetic manipulation of green fluorescent protein to increase brightness initiated a boom, with a myriad of fluorescent protein sensors now available that span the UV, visible and near-IR range; capable of detecting a great number of metabolites, ions, and other biological signaling components with increased spatial and temporal precision. Used for both steady-state and time-resolved approaches, fluorescent proteins can be used in a wide variety of quantitative approaches. Steady-state sensors are typically characterized as intensimetric or ratiometric; and intensimetric sensors are characterized by an increase or decrease in emission intensity in response to analyte. However, moving *in vivo*, concentration and intensity dependence of the fluorophore, sample thickness, and photobleaching are limiting factors. Ratiometric probes respond by an inverse change in excitation or emission profiles in response to analyte, normalizing for bleaching or protein expression effects. As an intrinsic property of fluorophores, fluorescence lifetime does not rely on protein concentration, method of measurement or fluorescence intensity. By monitoring changes in lifetime using fluorescence lifetime spectroscopy, no special ratiometric fluorophores are needed, opening up a wider selection of potential fluorescent sensors. Lifetime and other time-resolved approaches are becoming more and more popular due to ease of quantitation and increased signal to background. Here we present the *in vitro* and live-cell characterization of genetically encoded, ratiometric and lifetime optimized red fluorescent protein pH sensors, a methodology for quantifying receptor trafficking in real time, as well as a lanthanide time resolved imaging approach.

CHAPTER 1. INTRODUCTION

1.1 Fluorescent proteins are biologically compatible sensors

Optimized for use in applications from *in vitro* assays to physiology, fluorescent proteins can be localized to measure biological dynamics both qualitatively and quantitatively^{1,2}. A fluorescent protein is most commonly described as a protein with a fluorescent chromophore protected by an 11-stranded β -barrel structure (Figure 1). This hallmark β -barrel configuration is extremely important, and provides resistance to changes in environment, allowing continued fluorescence even in the presence of salts, denaturants, temperature fluctuations or other factors^{3,4}. Thus, fluorescent proteins are inherently chemically stable, however, continual optimization is ongoing to fulfill other experimental requirements. Ideally, a fluorescent biomarker would also have sufficient brightness, efficient delivery to the target of interest, high affinity and/or specificity, as well as discretely and uniquely signal events with minimal background. Perhaps most importantly, a fluorescent biomarker should not interfere with the environment being studied. Compared to organic dyes or other exogenous fluorophores, fluorescent proteins are easily genetically encoded, and in many cases do not impede the function of the target of interest or disrupt the local environment^{5,6}. This high biocompatibility has made them indispensable in life sciences research, proven by the sea of established protocols showing expression of a target protein tagged with fluorescent proteins allows for labeling of almost any protein of interest in the cell⁷.

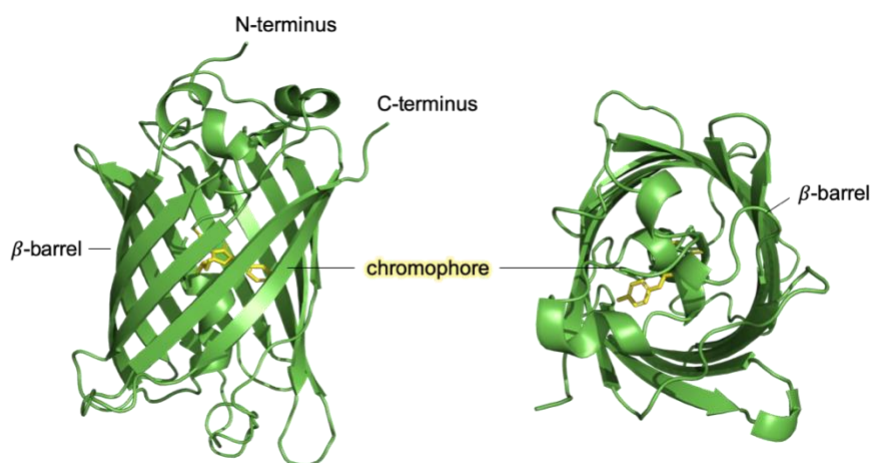


Figure 1 Green Fluorescent Protein (GFP) shows the canonical protein scaffold. A tripeptide chromophore is contained and protected by a β -barrel structure.

Broadly speaking, fluorescent proteins (FPs) are often classified as intensimetric or ratiometric based on signal output¹. Intensimetric FPs show a change in fluorescence intensity in response to an environmental change. Although a single excitation and emission peak provides room spectrally for multiplex imaging with other colored sensors, a change in fluorescence intensity does not account for protein expression levels or photobleaching effects. Ratiometric probes contain dual excitation or emission profiles that change inversely in response to a change in environment. For example, in response to changes in redox environment, the ratiometric protein sensor roGFP shows an increased 400 nm excitation peak in oxidizing conditions and an increased 480 nm excitation peak in reducing conditions⁸. Thus, dual peaks that inversely change with environmental changes can be exploited to normalize for expression or any bleaching artifacts. However, ratiometric FPs require more expansive use of an optical window and can limit co-localization and detection with other FP sensors.

1.2 Sensor Designs

Fluorescent proteins have been engineered to sense a myriad of biological parameters such as pH, ions, and metabolites⁸⁻¹¹. Sensing of these biologically relevant molecules happens one of three distinct ways: 1) By utilizing the intrinsic fluorescent properties of the protein 2) Appending an analyte sensitive domain to a fluorescent protein or 3) Tethering two fluorescent proteins together via a linker for Förster resonance energy transfer (FRET). In FRET based sensors, two spectrally compatible fluorescent proteins are linked in such a way that distance between them is altered in response to an analyte. As energy transfer between a ‘donor’ FP and an ‘acceptor’ FP is only efficient in close proximity and in correct orientation, after donor excitation, the output of acceptor fluorescence relative to the donor can be a quantitative measurement of biological molecules of interest (Figure 2C)^{12,13}. Fluorescent proteins with engineered sensing domains have also been used extensively; circularly permuting the beta-barrel structure can provide controlled fluorescence quenching. Due to solvent-induced non-radiative energy decay after chromophore excitation, an opening in the barrel will decrease fluorescent output. After binding to the ligand, binding domains on circularly permuted FPs undergo conformational changes so that access by solvent into the barrel is restricted, providing increased fluorescence output. For example, a

calmodulin/M13 domain is engineered onto the circularly permuted termini of GFP to create the calcium sensitive GCaMP family (Figure 2B)^{14,15}.

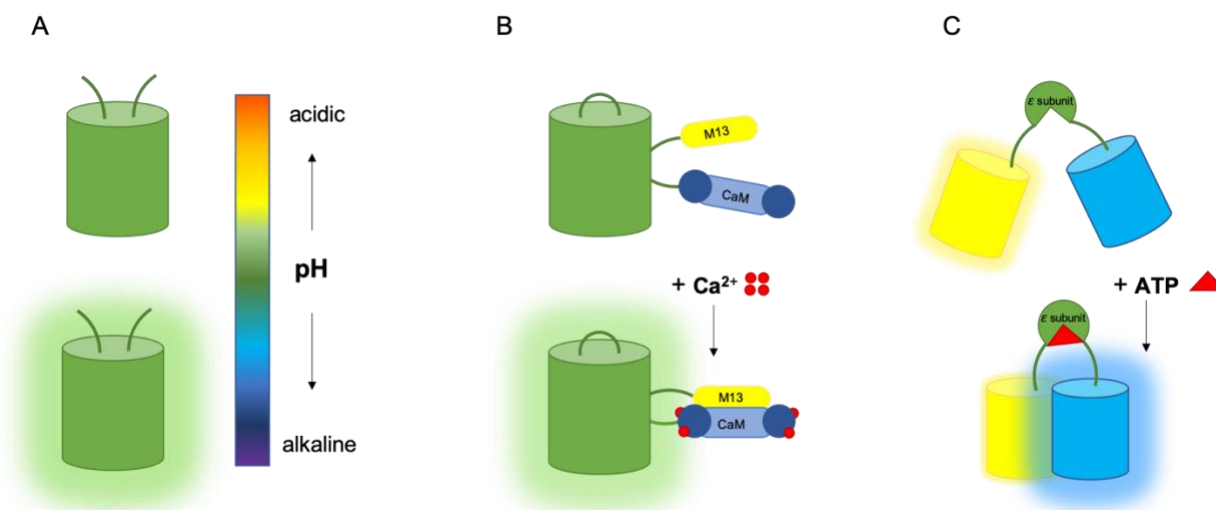


Figure 2 Fluorescent protein sensors can be broadly categorized three ways.

A) Fluorescence output is determined by the intrinsic characteristics of the protein in response to its environment. For example, a change in pH to more alkaline conditions deprotonates the chromophore causing an increase in fluorescence. B) Appending a sensing domain to the barrel induces solvent quenching of fluorescence except in the presence of the analyte. For example, introduction of Ca^{2+} to fluorescent proteins with a Calmodulin/M13 Calcium sensing domain shows an increase in fluorescence in the presence of calcium due to closure of the beta barrel after a Ca^{2+} induced conformational change. C) The termini of two fluorescent proteins are fused to a sensing domain. When in close proximity, fluorescence is non-radiatively transferred to the acceptor. For example, in the presence of ATP, the ATeam FRET sensors bind to the nucleotide, causing a conformational change, bringing the two fluorescent proteins in close enough proximity for FRET to occur¹⁶.

Perhaps the simplest method is utilizing the intrinsic properties of the fluorescent protein itself. For example, all fluorescent proteins are pH sensitive to varying extents¹⁷. Protonation of the chromophore can alter fluorescence output (Figure 2A), and mutating either the chromophore itself, or surrounding residues, can alter the pKa of the FP^{18–20}. Currently, there are limited FPs with chromophore pKas in the biologically relevant range. Additionally, there remains a need for red shifted pH sensors with emission wavelengths that can penetrate through deep tissue as well as provide spectrally compatible multiplex imaging for other visible spectrum sensors *in vitro*^{21,22}.

1.3 Red fluorescent proteins

As one of the founding fathers of fluorescent protein engineering, Roger Tsien began by establishing that a single point mutant (S65T) of the green fluorescent protein (GFP) resulted in significantly increased intensity and photostability compared to the wild type²³. Realizing mutagenesis efforts could manipulate photophysical characteristics without greatly effecting protein stability or function, a massive effort ensued which has resulted in fluorescent protein variants that span almost the entire UV, visible and near-IR spectrum²⁴. Derived from reef corals, red shifted variants have shown value in *in vivo* applications. The absorption of lipids, melanins and hemoglobin decreases significantly in what is known as the “optical window” between 600-1200 nm. With excitation and emission profiles nearing or in this window, red fluorescent (RF) or infrared fluorescent (IRF) proteins are able to penetrate deep tissue without fluorescence contamination from matrix molecules^{6,25}.

1.4 pH

The tight control of intracellular pH is vital for cell health, with aberrant changes in pH associated with a variety of disease pathogenesis including stroke and cancer²⁶⁻²⁹. The compartmentalization of pH within organelles is also critical. For example, pH gradients in the mitochondrial matrix provide the force needed in ATP synthesis and energy production^{30,31}. Likewise, neurotransmission is heavily dependent on pH gradients, with acidity of synaptic vesicles necessary for neurotransmitter loading and subsequent release into the synaptic terminal³². In microbiology, pH mechanisms of neutrophiles allow for survival in acidic environments. For example, the bacterium *H. pylori* maintain a neutral intracellular pH in the stomach of mammals by increasing urease production. The resulting increase in ammonium ions raises local pH and assists in survival³³. Thus, pH regulation plays a crucial role in protein function, metabolic reactions and a wide range of other processes in both mammalian and bacterial cells.

1.5 Red fluorescent proteins to quantify pH *in vivo*

Monitoring perturbations in local pH environments due to cellular activities or diseases, such as increased extracellular acidosis in the tumor microenvironment, would better our understanding

of disease pathology. Live-cell imaging with fluorescent protein-based sensors allows us to monitor pH changes *in situ*; however, there are currently limited options to accurately measure pH dynamics with subcellular resolution in live specimens. Concentration and intensity dependence of the fluorophore, sample thickness, and photobleaching are limiting factors.

Additionally, most of the current genetically encoded pH sensors are generated from GFP, limiting our ability to perform multiplex imaging to monitor pH simultaneously in different compartments¹⁷. There are currently a limited number of RFP pH sensors available. Sensors like pHuji and pHTomato are intensimetric, meaning response from changing pH is translated by an increase or decrease in the intensity of one excitation and emission peak^{18,20}. Intensimetric sensors can be problematic, as they do not account for expression levels or photobleaching in the sample.

Both ratiometric and lifetime sensors resolve these issues. Ratiometric FPs have dual excitation or emission profiles that can be used to normalize artifacts caused by differences in sensor concentration. For example, the red ratiometric pH sensor pHRed has been used to quantify pH fluctuations from *in vitro* assays to cultured neurons^{21,34}. As an intrinsic property of fluorophores, fluorescence lifetime does not rely on protein concentration, method of measurement or fluorescence intensity³⁵. By monitoring changes in lifetime as a function of pH, no special ratiometric fluorophores are needed, opening up a wider selection of potential fluorescent sensors. Presented here are both steady-state and time-resolved approaches for monitoring pH in live cells using red fluorescent protein sensors. Our work expands the toolbox of red fluorescent pH sensors, which can be used in a number of applications, including pH regulated synaptic transmission, endocytic events, and receptor trafficking.

1.6 Receptor trafficking and regulation

As the gatekeepers of cell signaling, membrane receptors are involved in various biological processes from cell-cell communication to initiating intracellular signaling cascades. The G-protein coupled receptor (GPCR) family is the largest cell membrane protein family, whose involvement in cell proliferation and movement has been linked to cancer growth and metastasis, making it a highly lucrative drug target^{36,37}. Unfortunately, the regulation of receptor translocation and recycling is not only not fully understood, but highly debated. The study of trafficking using

antibody targeting is both expensive and makes it cumbersome to temporally resolve receptor translocation in intracellular compartments^{38,39}. Fluorescent proteins can be engineered onto some receptors, but many require termini unencumbered by large fusion proteins for efficient signaling to occur. Short epitope tags like Flag, c-myc and HA are popular due to their relatively low interference with receptor function, however, all rely on high-affinity non-covalent interactions⁴⁰⁻⁴². A covalent interaction could increase signal to background, with only covalently bound molecules remaining after wash steps. SpyTag-SpyCatcher is a genetically-encoded system for covalent modification, which has previously shown minimal interference with receptor signaling⁴³. The SpyTag peptide is paired with a globulin-like protein SpyCatcher, that when in close proximity, forms a spontaneous covalent bond, tagging the receptor termini extracellularly using exogenously prepared biologically compatible materials⁴⁴. More specifically, by fusing a fluorescent protein to the exogenously added SpyCatcher, it becomes possible to track the entire lifetime of a receptor using genetically encoded fluorescent proteins. This would provide increased understanding in receptor signaling dynamics, which could lead to better designed therapeutics or other modulators.

1.7 Luminescence resonance energy transfer (LRET) for increased signal to background

In addition to developing a red fluorescent lifetime sensor, here we explore other time-resolved approaches for quantifying cell dynamics. Although great effort has been dedicated to increasing the brightness of fluorescent protein sensors, many are much weaker than some popular organic dyes or nanoparticles^{23,45,46}. Additionally, resolving dynamics *in vivo* remains difficult due to autofluorescence from intrinsic fluorophores in the cell. Compared to fluorescence lifetimes (nanoseconds), other modes of luminescence emission are much longer lived (millisecond to seconds)⁴⁷, and the extended emission lifetime could outlive nanosecond autofluorescence, greatly increasing signal to background and specificity. Lanthanide metals bound to chelates have luminescence properties that have been exploited for biological assays, however, they are often sold as *in vitro* assay kits and require the use of expensive antibody targets⁴⁸⁻⁵¹. In order to take advantage of already existing FP sensors, we sought to utilize lanthanides to easily convert fluorescent sensors to lanthanide-based TR-LRET sensors.

Förster resonance energy transfer is able to report dynamic changes in distance between two fluorescent molecules. In FRET systems, 'donor' emission overlaps 'acceptor' absorbance. After

donor excitation, the excited-state energy is non-radiatively transferred to excite a nearby acceptor, resulting in a shifted emission output. The Imperiali group has optimized several small peptide chelates of lanthanide metals called lanthanide binding tags (LBTs), which have shown relatively high affinity (nanomolar K_d) and specificity⁵². When excited by UV light, these LBT-bound lanthanides display spectra comparable to spectra from lanthanides bound to organic chelates, with several sharp emission peaks in the visible range. Recently, it has been shown engineering LBT tags onto fluorescent proteins can extend emission lifetime an order of magnitude⁵³. Here we explored a strategy for exploitation of both FRET and lanthanide emission by engineering a LBT tag onto a FRET pair, creating a long-lived triple relay after excitation in the UV.

1.8 Conclusion

The high biocompatibility and stability of fluorescent protein sensors has made them indispensable as a life sciences tool. By utilizing the intrinsic fluorescent properties of the protein, appending an analyte sensitive domain, or tethering two fluorescent proteins together via a linker for Förster resonance energy transfer (FRET), a collection of sensors has been developed to signal a number of cellular dynamics, including metabolism, cell motility and proliferation and apoptosis. However, due to background fluorescence from matrix molecules *in vivo*, there remains a need for red fluorescent protein sensors for light penetration through deep tissue. Here we present two red fluorescent pH sensors, optimized for both steady state characterization (mCherryEA), with ratiometric excitation peaks normalizing for protein expression and photobleaching; and time-resolved methods (mCherryTYG), utilizing the intrinsic property of lifetime to allow quantifiable pH determination across samples and instruments. Additionally, we explore appending pH sensing fluorescent proteins on the termini of receptors to track recycling conditions, as well as provide a novel approach for exogenously tagging receptors using a covalent SpyTag-SpyCatcher system. To further probe advantages of time-resolved techniques, we utilize a lanthanide binding tag to coordinate a terbium in close proximity to eGFP for luminescence resonance energy transfer. After gating background fluorescence with a 100 μ s delay after excitation, dynamic events can be detected with greatly increased signal to background. Here we present fluorescent proteins optimized for both steady-state and time-resolved techniques, allowing broadly applicable characterization both *in vitro* and *in vivo*.

Table 1 Engineered Sensors and Advantages

<i>Engineered Sensor</i>	Description	Advantages
<i>mCherryEA</i>	I158E/Q160A mutant of mCherry	Red, excitation ratiometric: used to quantify pH dynamics using steady-state techniques
<i>mCherryTYG</i>	M66T mutant of mCherry (chromophore mutation)	Red, large pH dependent dynamic range using time-resolved techniques
<i>SpyTag-GLUT4-mCherry</i>	Extracellular loop SpyTagged GLUT4 with a C-terminal mCherry FP fusion	Localization and characterization of receptor recycling activity with small, covalent tags, using steady-state techniques
<i>SpyTag-P2YR11</i>	N-terminally SpyTagged P2YR11	Localization and characterization of receptor recycling activity with small, covalent tags, using steady-state techniques
<i>LBT-eGFP</i>	eGFP with short peptide lanthanide binding tag	Time-resolved LRET greatly reduces background fluorescence from matrix fluorophores
<i>LBT-AKAR2CR</i>	PKA sensor AKAR2CR with short peptide lanthanide binding tag	Time-resolved LRET applied to established fluorescent kinase sensor

1.9 References

1. Bolbat, A. & Schultz, C. Recent developments of genetically encoded optical sensors for cell biology. *Biol. Cell* **109**, 1–23 (2017).
2. Wang, X. *et al.* Recent developments in lanthanide-based luminescent probes. *Coordination Chemistry Reviews* (2014). doi:10.1016/j.ccr.2014.02.001
3. Li, B., Shahid, R., Peshkepija, P. & Zimmer, M. Water diffusion in and out of the β -barrel of GFP and the fast maturing fluorescent protein, TurboGFP. *Chem. Phys.* (2012). doi:10.1016/j.chemphys.2011.11.001
4. Stepanenko, O. V., Stepanenko, O. V., Kuznetsova, I. M., Verkhusha, V. V. & Turoverov, K. K. Beta-Barrel Scaffold of Fluorescent Proteins. Folding, Stability and Role in Chromophore Formation. in *International Review of Cell and Molecular Biology* (2013). doi:10.1016/B978-0-12-407699-0.00004-2
5. Shaner, N. C. *et al.* Improved monomeric red, orange and yellow fluorescent proteins derived from *Discosoma* sp. red fluorescent protein. *Nat. Biotechnol.* **22**, 1567–1572 (2004).
6. Sakaue-Sawano, A. *et al.* Genetically Encoded Tools for Optical Dissection of the Mammalian Cell Cycle. *Mol. Cell* **68**, 626-640.e5 (2017).
7. Giepmans, B. N. G., Adams, S. R., Ellisman, M. H. & Tsien, R. Y. The fluorescent toolbox for assessing protein location and function. *Science* (2006). doi:10.1126/science.1124618
8. Jiang, K. Expression and Characterization of a Redox-Sensing Green Fluorescent Protein (Reduction-Oxidation-Sensitive Green Fluorescent Protein) in *Arabidopsis*. *PLANT Physiol.* (2006). doi:10.1104/pp.106.078246
9. Mahon, M. J. pHluorin2: an enhanced, ratiometric, pH-sensitive green fluorescent protein. *Adv. Biosci. Biotechnol.* **02**, 132–137 (2011).
10. Patel, N. & Gold, M. G. The genetically encoded tool set for investigating cAMP: More than the sum of its parts. *Front. Pharmacol.* **6**, 1–11 (2015).
11. Tantama, M., Martinez-Francois, J. R., Mongeon, R. & Yellen, G. Imaging energy status in live cells with a fluorescent biosensor of the intracellular ATP-to-ADP ratio. *Nat Commun* **4**, 2550 (2013).
12. Mastop, M. *et al.* Characterization of a spectrally diverse set of fluorescent proteins as FRET acceptors for mTurquoise2. *Sci. Rep.* **7**, 11999 (2017).
13. Carlson, H. J. & Campbell, R. E. Genetically encoded FRET-based biosensors for multiparameter fluorescence imaging. *Curr. Opin. Biotechnol.* **20**, 19–27 (2009).

14. Ding, J. J., Luo, A. F., Hu, L. Y., Wang, D. C. & Shao, F. Structural basis of the ultrasensitive calcium indicator GCaMP6. *Sci. China Life Sci.* (2014). doi:10.1007/s11427-013-4599-5
15. Akerboom, J. *et al.* Crystal structures of the GCaMP calcium sensor reveal the mechanism of fluorescence signal change and aid rational design. *J. Biol. Chem.* (2009). doi:10.1074/jbc.M807657200
16. Imamura, H. *et al.* Visualization of ATP levels inside single living cells with fluorescence resonance energy transfer-based genetically encoded indicators. *Proc. Natl. Acad. Sci.* **106**, 15651–15656 (2009).
17. Kneen, M., Farinas, J., Li, Y. & Verkman, A. S. Green fluorescent protein as a noninvasive intracellular pH indicator. *Biophys. J.* **74**, 1591–1599 (1998).
18. Li, Y. & Tsien, R. W. pHTomato, a red, genetically encoded indicator that enables multiplex interrogation of synaptic activity. *Nat. Neurosci.* **15**, 1047–53 (2012).
19. Benčina, M. Illumination of the spatial order of intracellular pH by genetically encoded pH-sensitive sensors. *Sensors (Switzerland)* **13**, 16736–16758 (2013).
20. Shen, Y., Rosendale, M., Campbell, R. E. & Perrais, D. pHuji, a pH-sensitive red fluorescent protein for imaging of exo- and endocytosis. *J. Cell Biol.* **207**, (2014).
21. Tantama, M., Hung, Y. P. & Yellen, G. Imaging intracellular pH in live cells with a genetically encoded red fluorescent protein sensor. *J. Am. Chem. Soc.* **133**, 10034–10037 (2011).
22. Shen, Y., Chen, Y., Wu, J., Shaner, N. C. & Campbell, R. E. Engineering of mCherry variants with long Stokes shift, red-shifted fluorescence, and low cytotoxicity. *PLoS One* **12**, 1–14 (2017).
23. Heim, R. & Tsien, R. Y. Engineering green fluorescent protein for improved brightness, longer wavelengths and fluorescence resonance energy transfer. *Curr. Biol.* (1996). doi:10.1016/S0960-9822(02)00450-5
24. Shaner, N. C., Steinbach, P. A. & Tsien, R. Y. A guide to choosing fluorescent proteins. *Nat. Methods* (2005). doi:10.1038/nmeth819
25. Chu, J. *et al.* Non-invasive intravital imaging of cellular differentiation with a bright red-excitable fluorescent protein. *Nat. Methods* **11**, (2014).
26. Estrella, V. *et al.* Acidity generated by the tumor microenvironment drives local invasion. *Cancer Res.* **73**, 1524–35 (2013).
27. Helmlinger, G., Sckell, A., Dellian, M., Forbes, N. S. & Jain, R. K. Acid production in glycolysis-impaired tumors provides new insights into tumor metabolism. *Clin. Cancer Res.* **8**, 1284–91 (2002).

28. Webb, B. A., Chimenti, M., Jacobson, M. P. & Barber, D. L. Dysregulated pH: a perfect storm for cancer progression. *Nat. Rev. Cancer* **11**, 671–677 (2011).
29. Orłowski, P., Chappell, M., Park, C. S., Grau, V. & Payne, S. Modelling of pH dynamics in brain cells after stroke. *Interface Focus* (2011). doi:10.1098/rsfs.2010.0025
30. Breckwoldt, M. O. *et al.* Mitochondrial redox and pH signaling occurs in axonal and synaptic organelle clusters. *Sci. Rep.* **6**, 23251 (2016).
31. Poburko, D., Santo-Domingo, J. & Demarex, N. Dynamic regulation of the mitochondrial proton gradient during cytosolic calcium elevations. *J. Biol. Chem.* **286**, 11672–11684 (2011).
32. Azarias, G. *et al.* Glutamate Transport Decreases Mitochondrial pH and Modulates Oxidative Metabolism in Astrocytes. *J. Neurosci.* **31**, 3550–3559 (2011).
33. Scott, D. R. *et al.* The role of internal urease in acid resistance of *Helicobacter pylori*. *Gastroenterology* (1998). doi:10.1016/S0016-5085(98)70633-X
34. Godinho, L. F. & Schrader, M. Determination of Peroxisomal pH in Living Mammalian Cells Using pHRed. in *Peroxisomes: Methods and Protocols, Methods in Molecular Biology* (ed. Schrader, M.) **1595**, 181–189 (Springer New York, 2017).
35. Berezin, M. Y. & Achilefu, S. Fluorescence Lifetime Measurements and Biological Imaging. *Chem. Rev.* (2010). doi:10.1021/cr900343z
36. Heng, B. C., Aubel, D. & Fussenegger, M. An overview of the diverse roles of G-protein coupled receptors (GPCRs) in the pathophysiology of various human diseases. *Biotechnology Advances* (2013). doi:10.1016/j.biotechadv.2013.08.017
37. Hauser, A. S., Attwood, M. M., Rask-Andersen, M., Schiöth, H. B. & Gloriam, D. E. Trends in GPCR drug discovery: new agents, targets and indications. *Nat. Rev. Drug Discov.* (2017). doi:10.1038/nrd.2017.178
38. Ritchie, M., Tchistiakova, L. & Scott, N. Implications of receptor-mediated endocytosis and intracellular trafficking dynamics in the development of antibody drug conjugates. *mAbs* (2013). doi:10.4161/mabs.22854
39. Bhattacharyya, S., Bhattacharya, R., Curley, S., McNiven, M. A. & Mukherjee, P. Nanoconjugation modulates the trafficking and mechanism of antibody induced receptor endocytosis. *Proc. Natl. Acad. Sci.* (2010). doi:10.1073/pnas.1006507107
40. Einhauer, A. & Jungbauer, A. The FLAGTM peptide, a versatile fusion tag for the purification of recombinant proteins. *Journal of Biochemical and Biophysical Methods* (2001). doi:10.1016/S0165-022X(01)00213-5
41. Zhao, X., Li, G. & Liang, S. Several affinity tags commonly used in chromatographic purification. *Journal of Analytical Methods in Chemistry* (2013). doi:10.1155/2013/581093

42. Jarmander, J., Gustavsson, M., Do, T. H., Samuelson, P. & Larsson, G. A dual tag system for facilitated detection of surface expressed proteins in *Escherichia coli*. *Microb. Cell Fact.* (2012). doi:10.1186/1475-2859-11-118
43. Veggiani, G. *et al.* Programmable polyproteins built using twin peptide superglues. *Proc. Natl. Acad. Sci. U. S. A.* **113**, 1202–7 (2016).
44. Bedbrook, C. N. *et al.* Genetically Encoded Spy Peptide Fusion System to Detect Plasma Membrane-Localized Proteins In Vivo. *Chem. Biol.* **22**, 1108–1121 (2015).
45. Klarenbeek, J., Goedhart, J., Van Batenburg, A., Groenewald, D. & Jalink, K. Fourth-generation Epac-based FRET sensors for cAMP feature exceptional brightness, photostability and dynamic range: Characterization of dedicated sensors for FLIM, for ratiometry and with high affinity. *PLoS One* **10**, 1–11 (2015).
46. Bindels, D. S. *et al.* MScarlet: A bright monomeric red fluorescent protein for cellular imaging. *Nat. Methods* **14**, (2016).
47. Ghose, S., Trinquet, E., Laget, M., Bazin, H. & Mathis, G. Rare earth cryptates for the investigation of molecular interactions in vitro and in living cells. *J. Alloys Compd.* **451**, 35–37 (2008).
48. Höferl, M., Krist, S. & Buchbauer, G. Adaptation of DELFIA™ cortisol kit for determination of salivary cortisol concentration. *Arch. Pharm. (Weinheim)*. (2005). doi:10.1002/ardp.200500116
49. Meyer, J. & Karst, U. Enzyme-linked immunosorbent assays based on peroxidase labels and enzyme-amplified lanthanide luminescence detection. *Analyst* (2001). doi:10.1039/b008293g
50. Zwier, J. M. *et al.* A fluorescent ligand-binding alternative using tag-lite technology. *J. Biomol. Screen.* **15**, 1248–1259 (2010).
51. Mathis, G. HTRF® technology. *Journal of Biomolecular Screening* (1999). doi:10.1177/108705719900400605
52. Sculimbrene, B. R. & Imperiali, B. Lanthanide-binding tags as luminescent probes for studying protein interactions. *J. Am. Chem. Soc.* **128**, 7346–7352 (2006).
53. Wu, Q. *et al.* A cell-penetrating protein designed for bimodal fluorescence and magnetic resonance imaging. *Chem. Sci.* **6**, 6607–6613 (2015).

CHAPTER 2. IMAGING PH DYNAMICS SIMULTANEOUSLY IN TWO CELLULAR COMPARTMENTS USING A RATIOMETRIC PH-SENSITIVE MUTANT OF MCHERRY

Reprinted with permission from *ACS Omega*. Rajendran, M., Claywell, B., Haynes, E.P., Scales, U., Henning, C.K., and Tantama, M. (2018). Imaging pH Dynamics Simultaneously in Two Cellular Compartments Using a Ratiometric pH-Sensitive Mutant of mCherry, *ACS Omega*, 8: 9476-9486. Copyright 2018 American Chemical Society.

2.1 Introduction

In eukaryotic cells, pH compartmentalization is critical for cellular processes such as mitochondrial energy production, protein degradation in lysosomes, and post-translational protein modification in the endoplasmic reticulum^{1,2}. In the brain, for example, organelle pH gradients are essential for proper neurophysiology. The acidification of synaptic vesicles provides the proton motive force for neurotransmitter loading, and the alkalization of the mitochondrial matrix provides the proton motive force for ATP synthesis, both of which are required for the energetically-expensive process of neurotransmission^{3,4}. Because neurotransmission is fundamentally a pH-dependent process, pH is also a useful indicator of activity. For example, transient pH fluctuations in the cytosol of neurons occur due to proton and ion fluxes, and mitochondrial pH fluctuates in response to energy consumption during action potential generation⁵⁻⁷.

Aberrant changes in pH are also commonly seen in diseases. For example, significant pH changes are seen during neurological disorders such as stroke and ischemia, where pH dynamics during hypoxia play an important role in cell survival^{1,8}. In cancer, altered pH homeostasis can occur⁹, and the Warburg effect and metabolic reprogramming can cause intracellular alkalization and extracellular acidification, both of which may play important roles in cell survival¹⁰⁻¹². Furthermore, regulation of organelle pH has been linked to oncogenic signaling^{13,14}, but we still need new pH sensors in order to accurately study organelle pH changes in the context of the entire cell.

In biological imaging studies, spatially-resolved pH dynamics are commonly visualized using pH-sensitive dyes, such as BCECF or SNARF¹⁵, and genetically-encoded green and yellow fluorescent protein-based pH sensors, such as pHluorin and SypHer^{16,17}. Genetically-encoded

sensors are advantageous because they can be targeted to subcellular locations. However, to study the role of proton exchange and buffering between different compartments in pH regulation, we need a toolbox of both green and red fluorescent pH sensors for multiplex imaging. Currently, many of the red fluorescent protein (RFP) sensors, such as pHTomato¹⁸, pHuji¹⁹ and mNectarine²⁰, report pH changes on the basis of fluorescence intensity alone. These sensors have high dynamic range and are very useful for the detection of events such as synaptic vesicle release¹⁸. However, ratiometric sensors are better-suited for quantifying pH changes because they are insensitive to variations in sensor concentration and photobleaching, which facilitates the comparison of pH dynamics between independent experiments. The ratiometric red fluorescent protein pH sensor pHRed²¹ has been used to monitor pH fluctuations in mitochondria²² and to measure peroxisomal pH²³. However, pHRed has a pK_a of 6.9, which limits its sensitivity in alkaline compartments because it exhibits smaller changes in its signal at pH greater than 8. The availability of spectral variants and pH sensors with a range of pK_a values would facilitate the study of pH changes in various cellular compartments.

In this study, we demonstrate that the I158E/Q160A mutant of mCherry, originally reported by Piatkevich *et al.*²⁴, is an effective ratiometric red fluorescent protein pH sensor. We characterize the pH-dependent fluorescence properties of the mCherry mutant protein in solution, and we also characterize its pH sensing performance in live cells. To demonstrate its use in biological studies, we show that it reports pH dynamics caused by changes in neuronal activity and metabolism. Furthermore, we demonstrate that it is spectrally compatible with the green fluorescent pH sensor ratiometric-pHluorin, facilitating the visualization of pH changes in mitochondria and the cytosol simultaneously within the same live cell.

2.2 Methods

2.2.1 Materials

Unless otherwise stated, chemicals were purchased from Sigma Aldrich; molecular biology enzymes were purchased from New England Biolabs (NEB); cell culture media and supplements were purchased from Invitrogen. Neuro2A and HEK-293 were purchased from ATCC, C57BL/6 and FVB mice were purchased from Charles River. Mitotracker DeepTM Red FM was a kind gift from Dr. Qing Deng at Purdue University.

2.2.2 Molecular Biology

pRSETb-mCherry(wt) and GW1-mCherry(wt) were mutated using the NEB Q5 site directed mutagenesis kit to generate the mCherry(I158E/Q160A) mutant. Mitochondria targeted mCherryEA was cloned by fusing a tandem 4xCoxVIII signal sequence²⁵ to the N-terminus. GW1-ratiometric-pHluorin and GW1-SypHer were generated by subcloning ratiometric-pHluorin from VV064: 1xCox8-ratiometric-pHluorin and SypHer from SypHer-mt into GW1 vector using NEB HiFi reactions. VV064: 1xCox8 -ratiometric-pHluorin in the FCK vector was a gift from Adam Cohen (Addgene plasmid # 58502) and SypHer-mt was a gift from Nicolas Demaurex (Addgene plasmid # 48251).

2.2.3 Protein Expression and Purification

pRSETb-mCherryEA was transformed into BL21(DE3) cells and grown in 500 mL autoinduction media (ForMedium™) at 37 °C overnight and transferred to 4 °C for 3 days. Protein was purified using HiTrap Nickel columns (GE healthcare) according to manufacturer instructions. Purified protein was dialyzed into storage solution (5mM MOPS, 150mM NaCl and 5% Glycerol, pH 7.4) and stored at -80 °C.

2.2.4 Steady-State Fluorescence Spectroscopy

pH titration was performed in solutions containing 10mM of each of Bis-Tris, MOPS, and Tris plus 100mM NaCl adjusted to pH values ranging from 5.5-9. Protein samples were diluted to 1-2 μM and fluorescence was measured in a microplate reader (BioTek Synergy H5). The excitation spectrum was measured using monochromator set to scan from 350nm-600nm with emission set at 630nm. The fluorescence was normalized by calculating the ratio of excitation peaks at 585nm by 450 nm. To test for environmental interference the mutants were titrated in buffered solutions containing either 100 mM NaCl, KCl or K-gluconate and the addition of 1 mM MgCl₂, 1 mM CaCl₂, 1 mM H₂O₂ and 3 mM DTT. For temperature dependence, the fluorescence measurement was taken with the reader set to 23, 25, 31 and 37 °C.

2.2.5 Cell Culture and Transfections

Neuro2A (ATCC CCL-131) and HEK-293 (ATCC CRL-1573) cells were cultured at 37 °C in 5% CO₂ humidified air incubator in DMEM media containing 10% cosmic calf serum (Hyclone). Cells were transfected using Effectene (Qiagen) per manufacturer's instructions and imaged after 2 days.

2.2.6 Neuron and Astrocyte Cultures

All animal procedures were performed in strict accordance with recommendations provided in the National Institutes of Health Guide for the Care and Use of Laboratory Animals, according to protocols approved by the Purdue Animal Care and Use Committee and the Purdue University Laboratory Animal Program to minimize pain and suffering. Cortical and hippocampal neurons were isolated from P0 mice and maintained in Neurobasal media supplemented with 5-25mM glucose, 0.2mM pyruvate, 0.5mM Glutamax, B-27, penicillin, and streptomycin (Pen/Strep). Neurons were transfected after 7-9 days using calcium phosphate method²⁶. Cortical astrocytes were isolated from P0-P4 mice and maintained in DMEM/F12 media supplemented with 10% FBS and Pen/Strep. Astrocytes were transfected using Lipofectamine3000 (Invitrogen) as per manufacturer's instructions.

2.2.7 Coefficient (ϵ) and Quantum Yield (QY)

The concentration of protein containing mature chromophore was quantified by measuring the absorbance of the protein in 1M NaOH at 450 nm (ϵ : 44000 M⁻¹.cm⁻¹) as previously described¹⁸. 28% of purified mCherryEA corresponded to mature chromophore. The concentration from alkaline denaturation method was used for ϵ and QY measurements. For ϵ measurement, absorbance and fluorescence spectra of the protein at dilutions of 5-20 μ M were measured. The ϵ was calculated according to Beer-Lambert equation. For QY measurement, slopes from absorbance vs fluorescence at different pH were measured with wild-type mCherry as the standard for excitation at 530 nm (QY = 0.22). QY at 440 nm was calculated relative to 530 nm QY.

2.2.8 Sensor Characterization in Live Cells

NH₄Cl: pH response of the sensors in live cells were tested by adding 10 mM NH₄Cl to the imaging solution (mM: 15 HEPES, 1.25 NaH₂PO₄, 10 glucose, 120 NaCl, 3 KCl, 2 CaCl₂, 1 MgCl₂, and 3 NaHCO₃, pH 7.3). *Cytosol pH calibration*: Neuro2A cells transfected with mCherryEA or

ratiometric-pHluorin were seeded in multi-well plate and exposed to different pH ranging from 5.5 to 9 in a high potassium solution (mM: 15 HEPES, 1.25 KH_2PO_4 , 10 glucose, 123 KCl, 2 CaCl_2 , 1 MgCl_2 , pH 7.3) in the presence of 2-5 μM nigericin^{21,27,28}. *Mitochondria pH calibration:* Neuro2A cells transfected with mito-mCherryEA or mito-pHluorin seeded in multi-well plate were exposed to pH 5.5 to 9 in a high potassium solution (mM: 15 HEPES, 10 glucose, 123 KCl, 20 NaCl, 2 CaCl_2 , 1 MgCl_2) in the presence of 5 $\mu\text{g}/\text{mL}$ nigericin and 5 μM monensin. For individual cell calibration, Neuro2A cells were treated with 10 mM NH_4Cl . After washing the cells with imaging solution, a three-point calibration was performed with high potassium solutions buffered at pH 6.0, 7.5 and 8.0.

2.2.9 Live-Cell Imaging

Cells were imaged using an Olympus IX83 fluorescence microscope with a 20x/0.75 NA and 60x/1.35 oil objective illuminated by a Lumencor SpectraX light engine and equipped with an Andor Zyla 4.2 sCMOS camera. Lumencor power levels were typically set at 5-10% for each ratio channel for cytosolic sensor and 15-30% for mitochondrial sensor. mCherryEA and pHRed were excited using 575/25 nm and 438/29 nm band-pass filters and emission was collected through a 632/60 nm band-pass filter. Ratiometric-pHluorin was excited using 475/34 nm and 395/25 nm band-pass filters and emission was collected through a 525/50 nm band-pass filter. SypHer was excited using 475/34 nm and 438/29 nm band-pass filters and emission was collected through a 525/50 nm band-pass filter. The exposure time set between 50-200 ms for all experiments, and fluorescence signals were at least 3-fold above background in all fluorescence channels. For mCherryEA and pHRed comparison, cells expressing each sensor were imaged on the same days under the exact same illumination and imaging conditions (exposure times, LED power, etc.). Neurons were perfused at 1mL/min with artificial cerebrospinal fluid (ACSF, mM: 15 HEPES, 120 NaCl, 3 KCl, 2 CaCl_2 , 1 MgCl_2 , 3 NaHCO_3 , 1.25 NaH_2PO_4 , 5 glucose, 0.2 pyruvate, 0.5 glutamax, pH 7.4). To confirm targeting of GW1-4xcox8-mCherryEA, 10 nM Mitotracker Deep Red (Invitrogen) was added to Neuro2A cells expressing mito-mCherryEA and treated as per manufacturer's instruction. High magnification images were captured using the 60x/1.35 oil objective. Mitotracker Deep Red was excited using 631/28 nm band-pass filter and emission was collected through a ET706/95 nm band-pass filter.

2.2.10 Data Analysis

Images were acquired with IQ (Andor) and analyzed with ImageJ. The mean and background intensities were measured for the images. The ratio was calculated by dividing the background subtracted means of images excited at the higher wavelength by the lower wavelength. For pixel-by-pixel measurement, fluorescence images were background subtracted and a threshold was set to reject background pixels. Ratio images were obtained by dividing the images captured by exciting at the higher and the lower excitation wavelengths.

2.3 Results

2.3.1 Characterization of mCherryEA as a ratiometric pH sensor

We first demonstrated that the mCherry(I158E/Q160A) mutant, which we refer to as “mCherryEA”, is a ratiometric pH sensor. The I158E and Q160A mutations were originally engineered to support excited state proton transfer (ESPT) in mCherry in order to generate a long Stokes shift variant (Figure 3A)²⁴. This mutant has not been used as a long Stokes shift RFP because at neutral pH it exhibits two excitation peaks corresponding to the protonated and deprotonated chromophore, with a single emission peak (Figure 3B). However, we hypothesized that existence of the two peaks would instead make the mutant an effective ratiometric pH sensor because it is proposed that the protonation state of Glu158 is sensitive to the pH of the surrounding solution²⁴, resulting in pH dependent protonation of the chromophore.

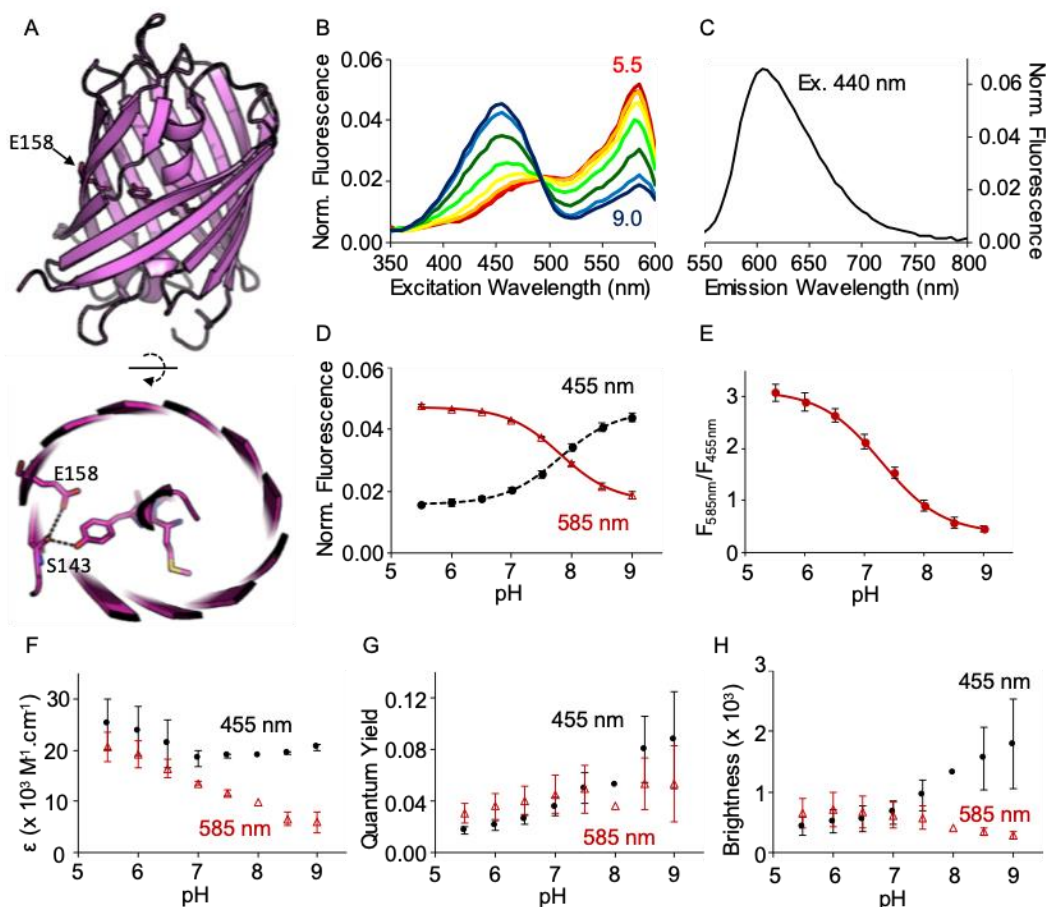


Figure 3 Characterization of purified mCherryEA in solution.

A) Structure of wildtype mCherry (PDB 2H5Q) showing the location of the E158 mutation relative to the chromophore. B) The pH-dependent fluorescence excitation and C) emission spectra ($\lambda_{\text{ex}}=440 \text{ nm}$) ($n=6$). Fluorescence was normalized to total integrated fluorescence. D) The pH titration curves for the fluorescence intensity with 455 nm (black, dashed) and 585 nm (red, solid) excitation with emission at 630 nm. E) The pH titration curve for the $F_{585\text{nm}}/F_{455\text{nm}}$ Ratio ($n=7$). The pH titration curves for the F) extinction coefficient, G) quantum yield, and H) brightness ($\epsilon \cdot \text{QY}$) ($n=2$). Data were fit to a Boltzmann equation, $\text{Ratio} = \text{Minimum} + (\text{Maximum} - \text{Minimum}) / (1 + \exp((\text{pH} - \text{pK}_a) / \text{slope}))$. Errors are stdev.

To determine whether the mCherryEA mutant exhibits a pH-dependent ratiometric change in the excitation spectra peaks, we characterized the pH response of purified mCherryEA protein in solution. The mutant showed pH dependent changes in its excitation spectra with a ratiometric change in excitation peaks at 455nm and 585nm, without a significant spectral shift in the emission peak at 610 nm (Figure 3B,C). We did not observe residual green emission from immature chromophore, and thus mCherryEA is compatible with blue, cyan, green, and yellow fluorescent proteins that exhibit spectrally-distinct emission peaks. As predicted, the proton transfer network²⁴ results in an “inverse” pH dependence with an increase from pH 5.5 to pH 9, causing a 2.80 ± 0.14 -fold increase in the 455nm peak (protonated form) and 2.54 ± 0.20 -fold decrease in 585 nm peak (deprotonated form) with a pK_a of 7.8 (Figure 3D). Fold change was measured by dividing the highest fluorescence ratio by the lowest fluorescence ratio. The intensity Ratio ($F_{585\text{nm}}/F_{455\text{nm}}$) showed a 6.90 ± 0.83 -fold ($n=7$, mean \pm std) increase with decrease in pH from 9 to 5.5, and the pK_a was 7.29 ± 0.03 for the ratio response (Figure 3E). The pH response was insensitive to variation of salts (NaCl, KCl, MgCl₂, K-Gluconate), oxidative stress (H₂O₂ & DTT) and temperature (25-37 °C) (Figure 4).

To compare the brightness of the mCherryEA mutant relative to wildtype mCherry, we measured the extinction coefficient (ϵ) and quantum yield (QY) of each protein in solution. At pH 7.5, the mutant ($\epsilon=11650 \text{ M}^{-1}\text{cm}^{-1}$, QY=0.05) was dimmer compared to wildtype mCherry ($\epsilon=72000\text{M}^{-1}\text{cm}^{-1}$, QY=0.22)²⁹. Both the excitation peaks showed an increase in QY with increasing pH (Figure 3F). However, the $\epsilon_{530\text{nm}}$ decreased with increasing pH and $\epsilon_{440\text{nm}}$ remains relatively unchanged (Figure 3G). The brightness ($\epsilon \cdot \text{QY}$) for the 455nm peak showed a larger change compared to the 585 nm peak and it drives the dynamic range of the ratio (Figure 3H). These results show that the mCherryEA mutant can serve as a ratiometric pH sensor, and therefore it could be an important addition to the toolset of quantitative pH sensors. However, due to the relatively low brightness of the purified protein, we next characterized the sensor expressed in live cells and found it to be well suited for live-cell ratiometric imaging

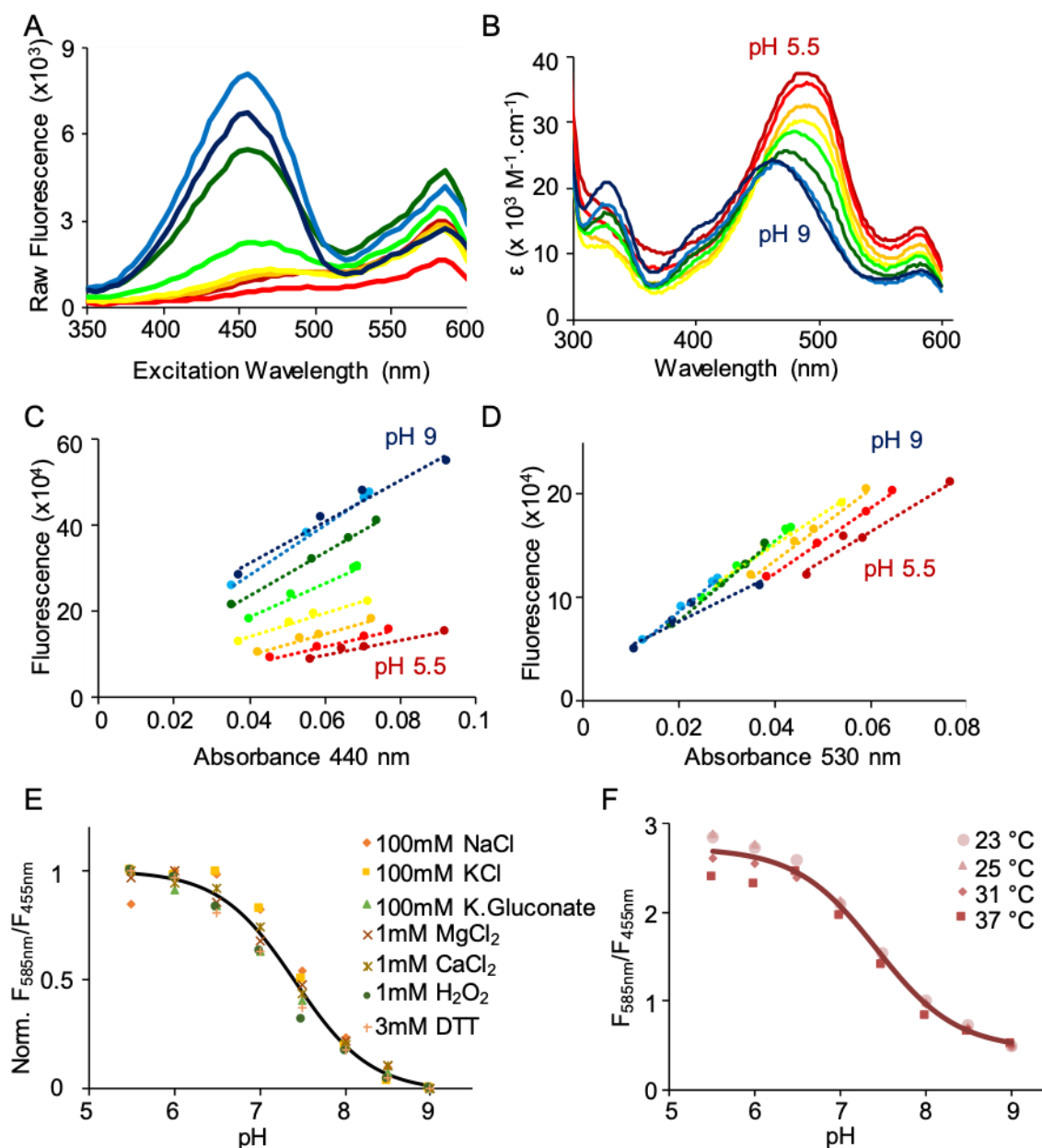


Figure 4 Further characterization of purified mCherryEA in solution

A) pH dependent raw fluorescence excitation spectra and B) pH dependent extinction coefficient spectra for mCherryEA. C) Integrated fluorescence vs absorbance at 440 nm and D) 530 nm peaks. E) pH response of the sensor was not affected in presence of various salts and oxidizing agents and F) temperature. Graphs E and F averages were fit to equation, $\text{Ratio} = \text{Bottom} + (\text{Top} - \text{Bottom}) / (1 + \exp((\text{pH} - \text{pKa})/\text{slope}))$.

2.3.2 Live-Cell Ratiometric Imaging

To test mCherryEA as a pH sensor in cellular imaging, we expressed the protein in mammalian cells. The brightness of mCherryEA was comparable to pHRed in several mammalian cell lines using exactly the same illumination and imaging conditions (Figure 5, Figure 6), and we did not observe any cell toxicity during extended imaging sessions that lasted over 2 hours. Differences in sensor characteristics in live cells compared to purified protein measurements have been observed for other fluorescent proteins and sensors, though the exact reasons are unknown.^{27,30} Thus, despite the low ϵ and QY measured for purified protein in solution, in live cells mCherryEA exhibits sufficient brightness to provide a high fluorescence signal over background.

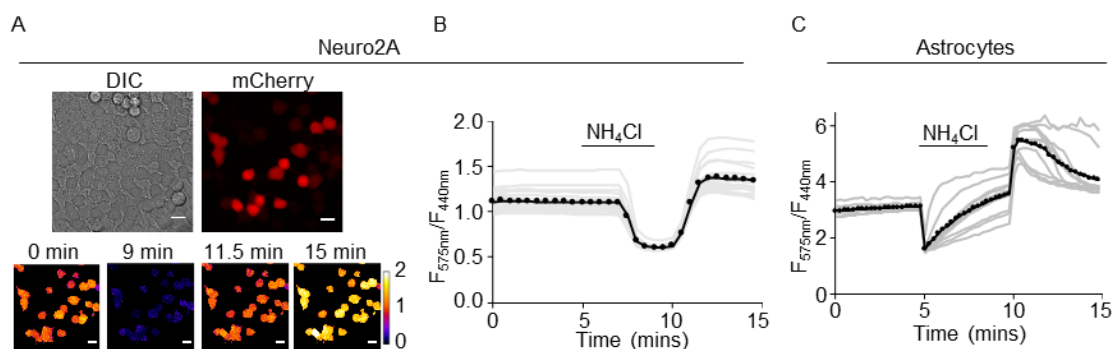


Figure 5 mCherryEA reports live-cell pH changes in different cell types

A) Top: DIC and fluorescence images showing the expression of mCherryEA in the cytosol of Neuro2A cells. Bottom: Representative pseudo-colored image sequence showing changes in pixel-by-pixel fluorescence ratio over time in response to a transient NH₄Cl pulse. B) The pH response upon exposure to 10 mM NH₄Cl measured as the F_{575}/F_{440} ratio over time (n=20). C) The pH response in primary astrocytes expressing mCherryEA upon exposure to 10 mM NH₄Cl (n=11).

We next tested mCherryEA's pH response by exposing the cells to ammonium chloride (NH₄Cl). It is well-established that exposure to NH₄Cl causes a transient alkalinization and re-acidification upon wash-out³¹. The responsiveness of the mutant was demonstrated in Neuro2A cells expressing mCherryEA in the cytosol (Figure 5A). The cells were exposed to 10 mM NH₄Cl for 5 minutes and then washed with imaging solution. The pH response was determined by measuring the Ratio (F_{575nm}/F_{440nm}) for single cells over time (Figure 5A). As expected, the addition of NH₄Cl caused alkalinization of the cytosol followed by re-acidification upon removal

of NH_4Cl (Figure 5B). We found that mCherryEA exhibited a 2.3 ± 0.2 fold change in ratio signal ($n=20$, mean \pm std) in response to the NH_4Cl transient, which was comparable to the 4.2 ± 0.7 fold change observed for pHRed ($n=29$, mean \pm std) (Figure 5B, Figure 6). We saw similar responses in cultured primary astrocytes (Figure 5C, Figure 7) and in HEK293 cells (Figure 7). Note that the lag in pH response to NH_4Cl is caused by the slow perfusion delay and variability in mixing in the live-cell imaging chamber, which also contributes to overall differences in the response. Interestingly, we observed that primary astrocytes regulate cytosolic pH more strongly than Neuro2A cells. That is, the astrocytes exhibited a rebound neutralization during the NH_4Cl exposure, which was not observed in Neuro2A cells (Figure 5B, C). It is not clear if this is an active or passive homeostatic mechanism, but future experiments could address the energy dependence of the response by pairing mCherryEA with one of the currently available green fluorescent ATP sensors^{32–34}.

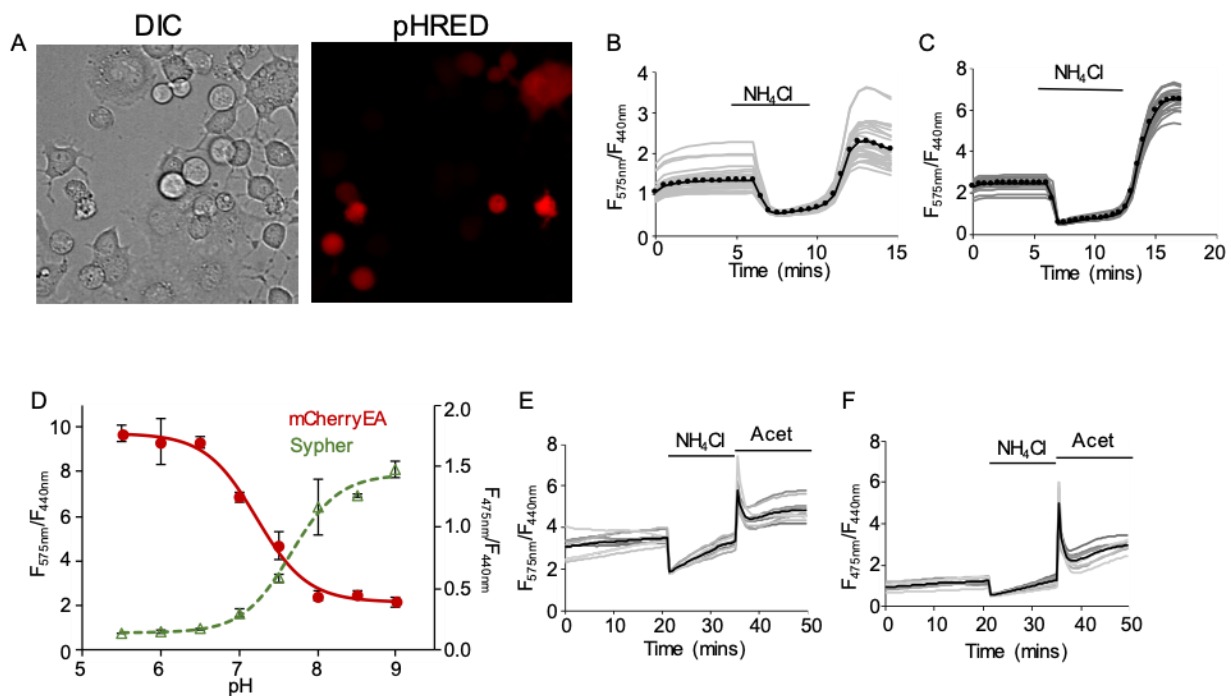


Figure 6 Characterization of mCherryEA in live cells

A) DIC and fluorescence image showing pHRed expression in Neuro2A cells B) pH response to 10 mM NH_4Cl in Neuro2A cells and C) HEK-293 cells expressing cyto-pHRed. D) pH titration in Neuro2A cells expressing mCherryEA (red line) and Sypher (green dashed line) using K^+/H^+ nigericin clamp ($n = 3$ wells with 4-10 cells each). E) The pH response of mCherryEA in Neuro2A cells upon exposure to 10 mM NH_4Cl and 10 mM acetic acid (Acet) measured as $F_{575\text{nm}}/F_{440\text{nm}}$ ratio over time (no. of cells=10). F) The pH response of Sypher in Neuro2A upon exposure to 10

mM NH₄Cl and 10 mM acetic acid (Acet) measured as F_{475nm}/F_{440nm} ratio over time (no. of cells = 10). Bars indicate std

We did observe that long-term expression of both wildtype mCherry and mutant mCherryEA resulted in the formation of red fluorescent puncta in cultured astrocytes after several days (Figure 7). This may be due to protein accumulation in lysosomes, which has been observed for other red fluorescent proteins³⁵⁻³⁷. To avoid complications caused by puncta formation, all subsequent experiments were carried out two days after transfection when neurons and Neuro2A cells did not show any puncta and therefore did not interfere with its use or analysis.

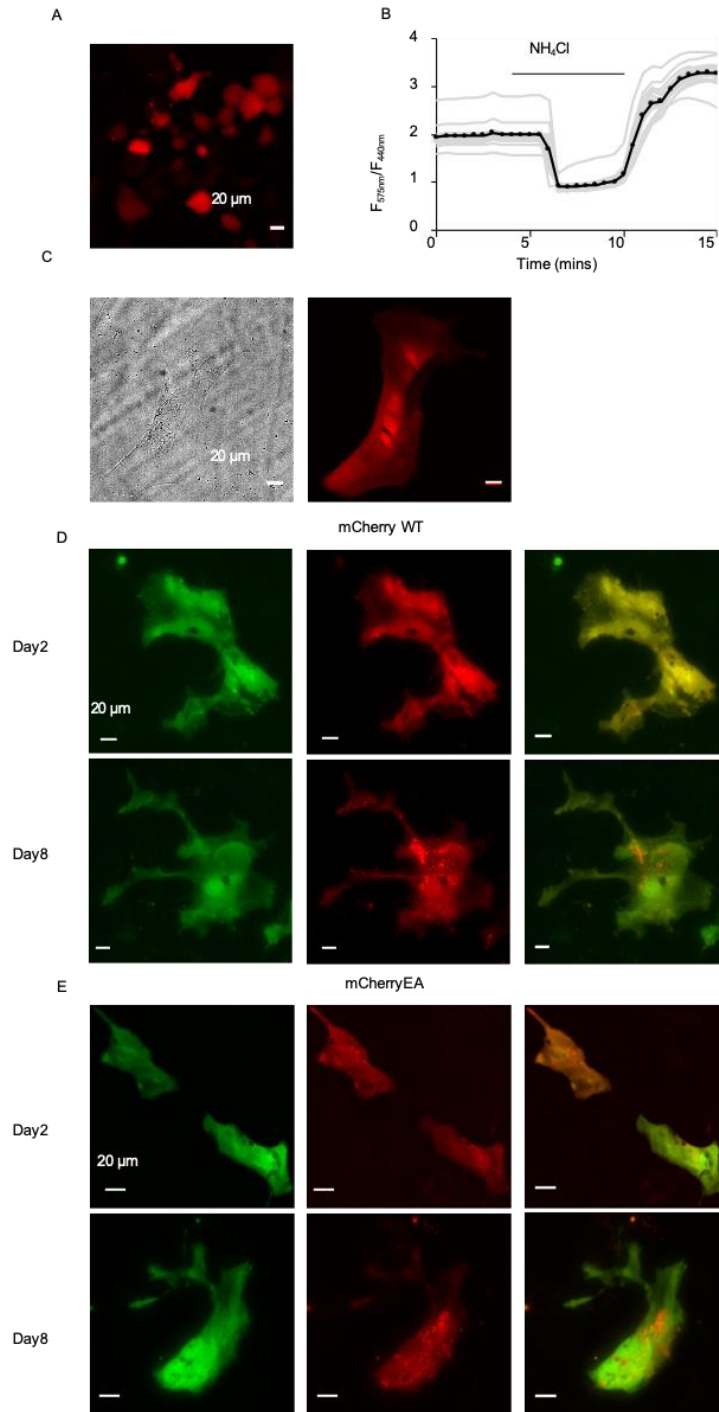


Figure 7 mCherryEA expression in HEK-293 cells and primary astrocytes
 A) HEK-293 expressing mCherryEA and B) pH response upon exposure to NH_4Cl measured as F_{575}/F_{440} ratio over time ($n = 20$). C) Primary astrocytes DIC and fluorescence image showing expression of mCherryEA. Astrocytes co-expressing roGFP2 and wildtype mCherry (D) or mCherryEA (E) on day2 (top) and day8 (bottom) after transfection showing red puncta formation over time.

2.3.3 Live-Cell pH Calibration

To calibrate the pH response, we performed an *in situ* pH titration in Neuro2A cells expressing cytoplasmic mCherryEA using the ionophore nigericin. Nigericin is a K^+/H^+ ionophore, which equilibrates the intracellular pH and extracellular pH when high potassium imaging solution is used³⁸. The cells were exposed to nigericin solutions to clamp cytosolic pH from pH 5.5 to 9, and steady-state values were measured over a period of 15 to 30 minutes (Figure 9). mCherryEA in cells has a pK_a of 7.31 ± 0.01 ($n=3$, mean \pm std) (Figure 8A), consistent with the pK_a measured with the purified protein in solution (Figure 3E). We also carried out an end-of-experiment nigericin pH calibration after exposing cells to an ammonium chloride transient pulse, demonstrating that it is possible to normalize ratio signals into pH values (Figure 8B, Figure 10).

The pK_a of mCherryEA also makes it well-suited for studying pH changes in the mitochondria matrix, which can fluctuate between neutral and alkaline conditions (pH 7-8)¹⁷³⁹. We first demonstrated efficient targeting of mito-mCherryEA in Neuro2A cells using the mitochondrial stain, MitoTracker Deep Red, and high magnification images confirm colocalization of mito-mCherryEA and MitoTracker (Pearson correlation coefficient 0.93 ± 0.06 , $n=12$ cells) (Figure 8C, Figure 11). The *in situ* pH titration of Neuro2A cells expressing mito-mCherryEA was carried out using nigericin plus monensin to clamp mitochondrial pH from pH 5.5 to 9¹⁷, and we measured a pK_a of 7.18 ± 0.09 ($n=3$, mean \pm std) similar to both purified protein and *in situ* cytosolic values (Figure 8D). Again, we carried out an end-of-experiment pH calibration using nigericin plus monensin following an ammonium chloride treatment to demonstrate that ratio signals can be normalized to mitochondrial pH values (Figure 8E). Interestingly, we observed that mitochondrial pH resided near neutral pH, as has been observed for HeLa cells in other studies¹⁷.

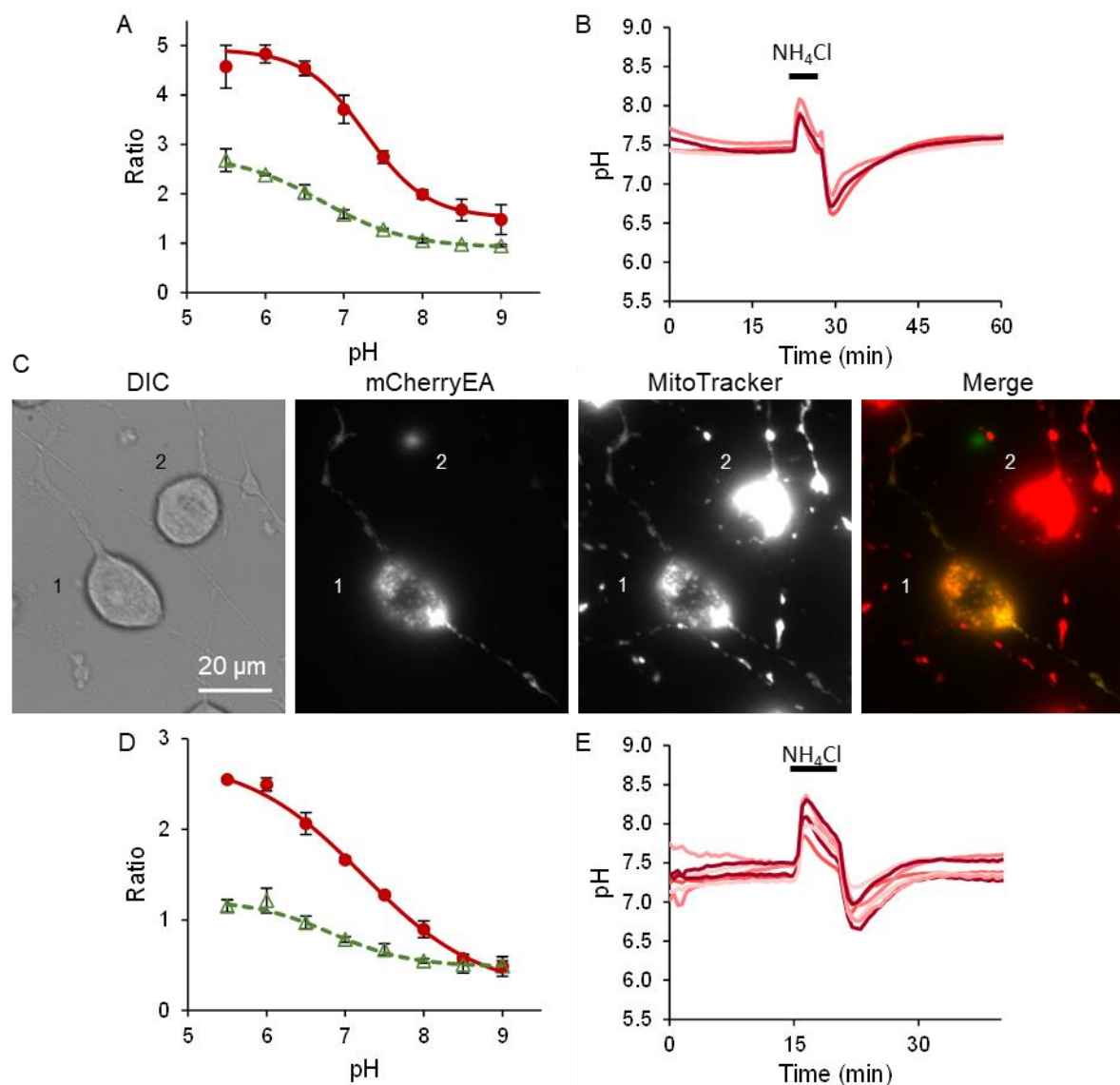


Figure 8 *In situ* pH calibration of mCherryEA in the cytosol and mitochondria live cells
 A) pH titration of Neuro2A cells expressing cytosolic mCherryEA (red line, n = 6, 10 cells each) or ratiometric-pHluorin (green dashed line, n = 3, 10 cells each) using nigericin. B) pH change upon exposure to a transient 10 mM NH₄Cl pulse in Neuro2A cells expressing cytosolic mCherryEA that were calibrated using nigericin at the end of the experiment (n=4). C) Example DIC and fluorescence images of a Neuro2A cell showing colocalization of mito-mCherryEA and MitoTracker Deep Red. Cell 1 expressed mito-mCherryEA but Cell 2 was not transfected. Cell 1 shows colocalization (yellow) of mito-mCherryEA (green) and MitoTracker (red). D) pH titration of Neuro2A cells expressing mito-mCherryEA (red line) and mito-ratiometric-pHluorin (green dashed line) using nigericin plus monensin (n=3, 4-15 cells each). E) pH change upon exposure to a transient 10 mM NH₄Cl pulse in Neuro2A cells expressing mito-mCherryEA that were calibrated using nigericin plus monensin at the end of the experiment (n=7). Bars indicate std.

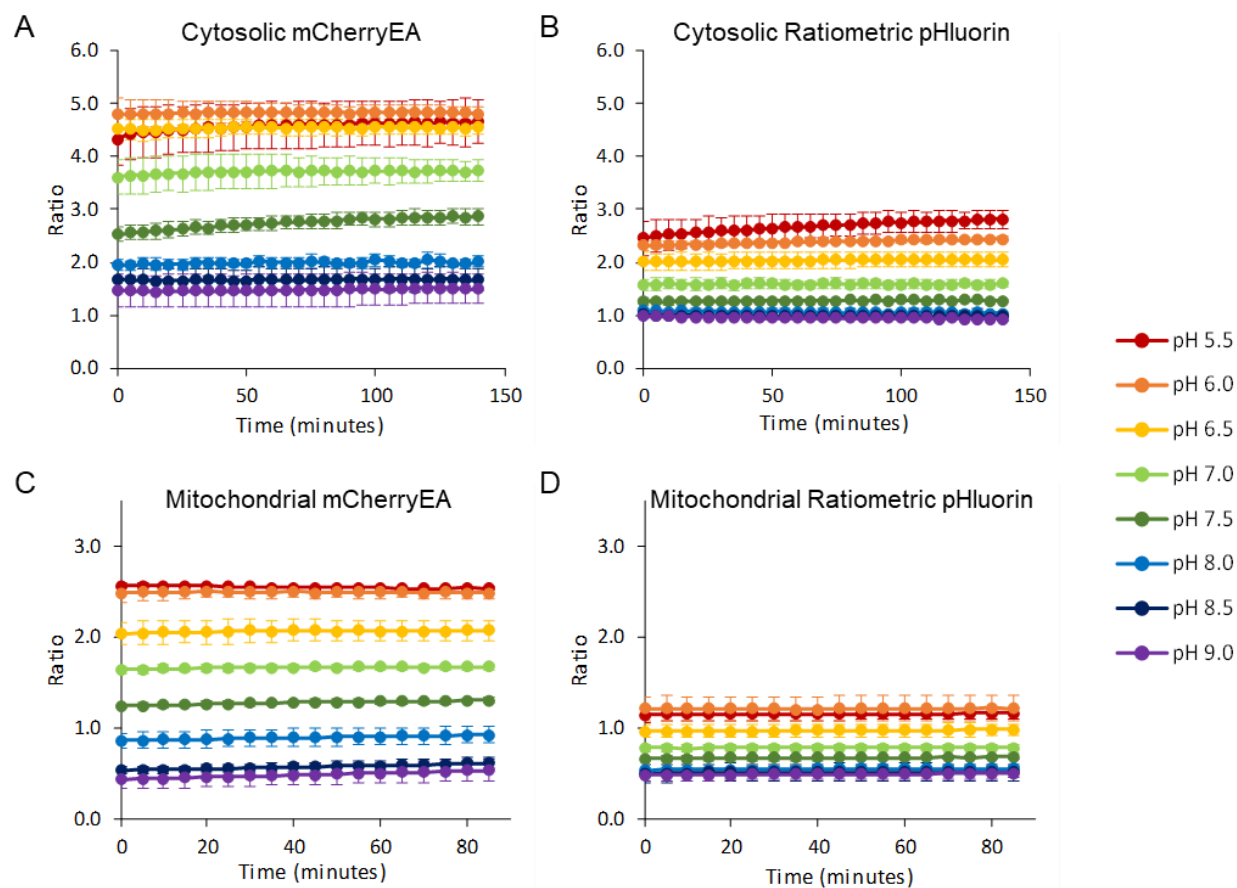


Figure 9 pH titration time course in Neuro2A cells
 pH dependent change fluorescence ratio in Neuro2A cells expressing cyto-mCherryEA (A) and cyto-ratiometric-pHluorin (B) exposed to pH 5.5 to 9 in different wells using K^+/H^+ nigericin clamp. pH dependent change fluorescence ratio in Neuro2A cells expressing mito-mCherryEA (C) and mito-ratiometric-pHluorin (D) exposed to pH 5.5 to 9 in different wells using K^+/H^+ nigericin/monensin clamp. Bar indicate std

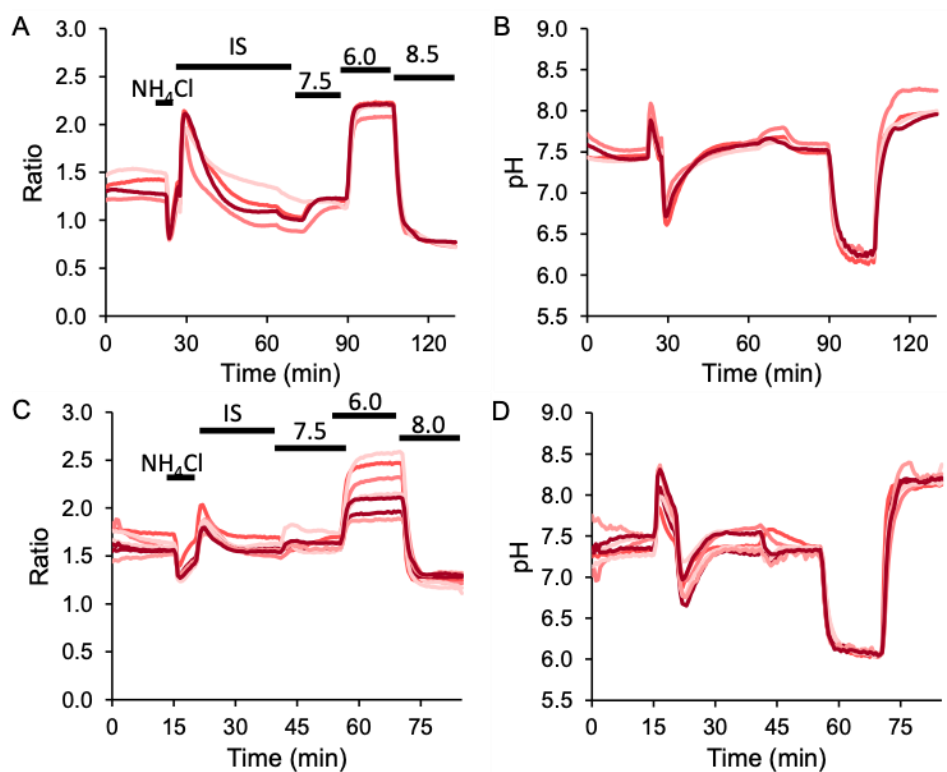


Figure 10 pH calibration in Neuro2A cells

A) Fluorescence ratio and B) corresponding pH change in Neuro2A cells expressing cyto-mCherryEA, which was exposed to 10 mM NH_4Cl , washed with imaging solution (IS) and calibrated using K^+/H^+ nigericin clamp at pH 6.0, 7.5, and 8.5. C) Fluorescence ratio and D) corresponding pH change in Neuro2A cells expressing mito-mCherryEA, which was exposed to 10 mM NH_4Cl , washed with imaging solution (IS) and calibrated using K^+/H^+ nigericin/monensin clamp at pH 6.0, 7.5, and 8.0. E) pH response in Neuro2A cells expressing cyto-mCherryEA to extracellular pH before and after the addition of nigericin (no. of cells =12). Bars indicate std.

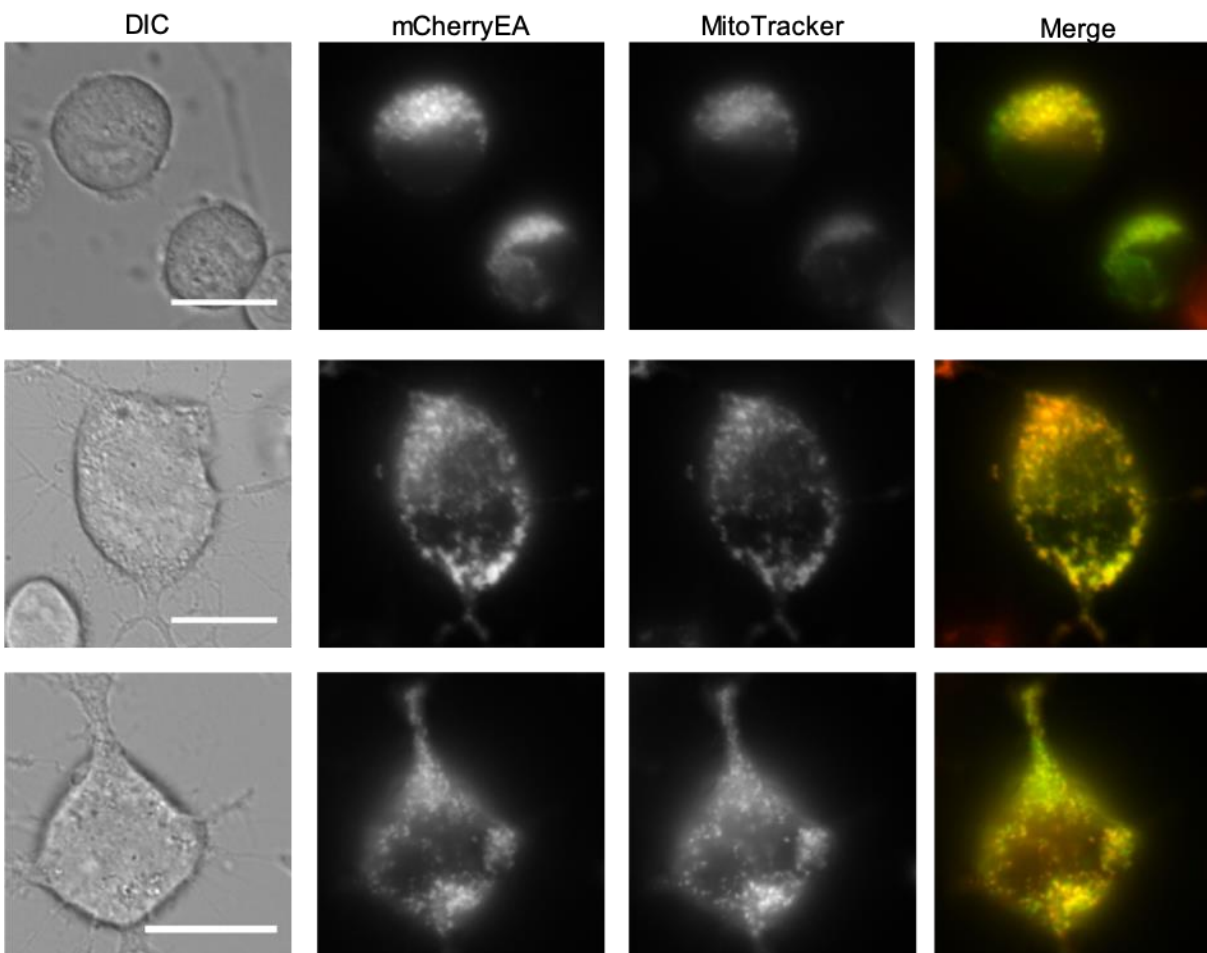


Figure 11 Additional example images demonstrating colocalization of mito-mCherryEA and MitoTracker Deep Red to confirm proper mitochondrial targeting of mito-mCherryEA

The merged images use pseudo-coloring to qualitatively demonstrate colocalization (yellow) of mito-mCherryEA (green) and Mitotracker (red). Scale bar is 20 μm . Mito-mCherryEA and Mitotracker fluorescence was highly correlated for a total of 12 cells that were analyzed with unbiased automatic thresholds to discriminate background and fluorescent pixels. The average Pearson correlation coefficient for above threshold pixels was 0.93 ± 0.06 , which was significantly greater than the correlation coefficient of 0.23 ± 0.31 for below threshold pixels ($n=12$, 2-tail t-test $p=0.000013$).

For comparison to mCherryEA, ratiometric-pHluorin¹⁶ is a green fluorescent pH sensor that is also based on a mutated single fluorescent protein. In the cytoplasm, mCherryEA exhibited a maximum fold change of $\text{Ratio}_{\text{max}}/\text{Ratio}_{\text{min}} = 3.84 \pm 0.91$ (mean \pm std, n=6), which is similar to ratiometric-pHluorin expressed in the cytosol of cells ($\text{Ratio}_{\text{max}}/\text{Ratio}_{\text{min}} = 2.83 \pm 0.20$, $\text{pK}_a = 6.38 \pm 0.77$, n=3) (Figure 8A). The maximum fold change was similar for mCherryEA in mitochondria ($\text{Ratio}_{\text{max}}/\text{Ratio}_{\text{min}} = 4.42 \pm 1.08$, mean \pm std). However, mito-ratiometric-pHluorin showed dampened dynamic range ($\text{Ratio}_{\text{max}}/\text{Ratio}_{\text{min}} = 1.36 \pm 0.16$, $\text{pK}_a = 6.83 \pm 0.10$, mean \pm std, n =3) (Figure 8D).

Thus, we have demonstrated that mCherryEA can be used for calibrated pH measurements in the cytosol and mitochondria of live cells. Ideally, *in situ* pH calibrations are carried out on a cell-by-cell basis at the end of each experiment in order to transform the ratio signal into an absolute pH value¹⁷. However, in practice ionophores and permeabilization reagents such as nigericin and monensin can cause cell death in sensitive cell types such as primary neurons or after experimental paradigms that already cause significant cell stress, and the low yield of successful calibrations can be prohibitive. Despite this complication, relative pH changes within a compartment can be measured more easily and have proven sufficient for studying many physiological processes, including metabolism and neuronal activity⁴⁰⁻⁴². Therefore, we next demonstrated that mCherryEA can be used together ratiometric-pHluorin to measure relative changes in compartment-specific pH, taking advantage of the fact that the spectral crosstalk between mCherryEA and ratiometric-pHluorin is minimal ($\leq 3\%$). Although the ratio signals that we measure cannot be used to directly compare absolute differences in pH between compartments, they can be used to observe correlations between relative pH changes. We conducted two proof-of-concept experiments. First, we demonstrated that both cytosolic and mitochondrial pH exhibit activity-dependent acidification in neurons. To do this we expressed mCherryEA in cytosol and ratiometric-pHluorin in mitochondria. Second, we demonstrated that relative changes in cytosolic and mitochondrial pH correlate with metabolic inhibition. To do this, we also demonstrate that mCherryEA and ratiometric-pHluorin can be used in either compartment.

2.3.4 Neuronal activity-dependent pH dynamics

Neuronal activity involves membrane depolarization, and membrane depolarization results in the acidification of neurons^{8,43}. Membrane depolarization can be caused by neurotransmitters such as glutamate or a rise in external potassium chloride, and both proton fluxes through channels and metabolic generation of acid equivalents can contribute to the pH dynamics^{44,45}. To test the utility of mCherryEA in visualizing this activity-dependent acidification, we expressed mCherryEA in the cytosol of cultured mouse hippocampal neurons (Figure 12A). Upon transient stimulation with 10 μ M glutamate, we were able to visualize acidification in the cytosol as expected (Figure 12B, C first arrow, Figure 13). This was followed by wash-in of 100 μ M ATP before a second pulse of glutamate in the presence of ATP (Figure 12B,C second arrow). ATP was then washed out prior to a third glutamate application (Figure 12B,C third arrow). The activity-dependent acidification of the cytosol could be observed with repeated glutamate stimulation, and it was not modified by the application of neuromodulators, such as extracellular ATP acting on neuronal purinergic receptors⁴⁶. To validate that mCherryEA was responsive to both acidic and alkaline changes in pH, we exposed neurons to a transient pulse of NH_4Cl . Cells exhibited a biphasic response, demonstrating that it is functionally responsive in neurons, similar to other cell types (Figure 5). Because energy metabolism contributes significantly to activity-dependent acidification, we also investigated pH dynamics more closely in both the cytosol and mitochondria.

Neuron excitation is a highly energy consuming process, requiring increased glycolysis and mitochondrial respiration for ATP production. Thus, the increased energy demand drives pH changes in both the cytosol and the mitochondrial matrix, and we used a dual pH sensor imaging approach to test how strongly the compartment-specific pH dynamics are coupled to activity. By co-expressing cytosolic mCherryEA and mitochondria-targeted ratiometric-pHluorin⁴⁷ in the same neurons (Figure 12, Figure 14), we were able to observe synchronous activity-dependent pH changes with similar dynamics in cytosol and mitochondria. Notably, the spectral crosstalk between the mCherryEA red fluorescence and ratiometric-pHluorin green fluorescence channels is minimal ($\leq 3\%$) and does not account for the synchronous changes in cytosolic and mitochondria pH. Thus, the ratio signals report that activity-dependent acidification occurred in each compartment. Although we were unable to carry out pH calibrations due to the toxicity of nigericin and monensin to the cultured neurons, the responsivity of both sensors was validated at the end of the experiment by exposing the cells to NH_4Cl . The activity-dependent pH responses observed in

both the cytosol and mitochondria could indicate coupling of neuronal activity to mitochondrial ATP synthesis or uncoupling of pH compartmentation due to increased Ca^{2+} flux. For example, Azarias *et al.* saw glutamate-induced acidification in mitochondria of astrocytes, which they report was due to loss of cytosol-mitochondrial pH gradient. They also saw pH dependent loss of metabolism in mitochondria⁴⁸. Further calibration and studies with metabolic sensors would help us better understand the effect of increased neuronal activity on pH and neuron metabolism. Overall, in this proof-of-concept study, we validated that mCherryEA can be used to measure pH dynamics in cultured neurons. We were also able to observe activity-dependent pH changes in different compartments by expressing mCherryEA in the cytosol and ratiometric-pHluorin in the mitochondria of the same cell.

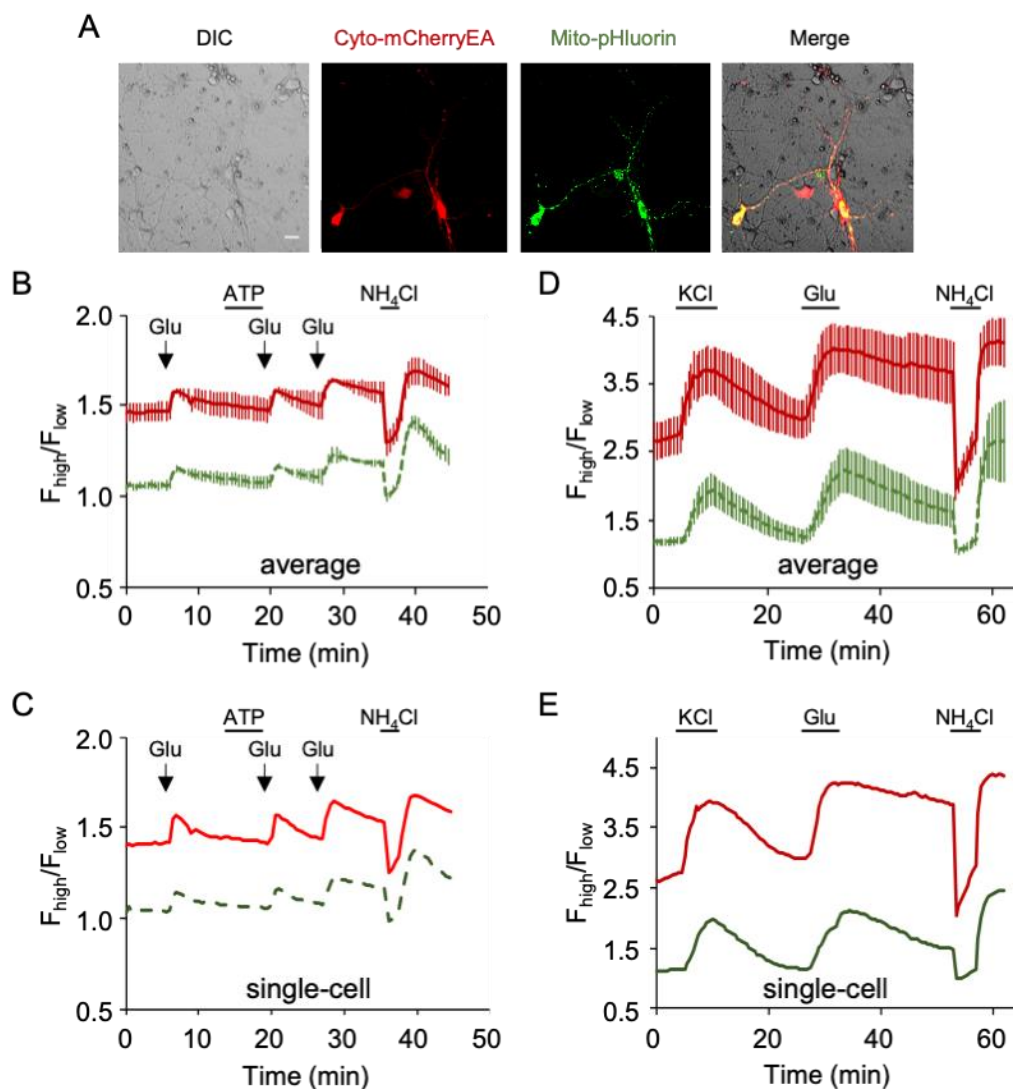


Figure 12 Activity-dependent pH changes in neurons

A) Representative images showing cortical neurons: DIC, cytosolic mCherryEA (red, $\lambda_{\text{ex}}=575$ nm, $\lambda_{\text{em}}=632$ nm), mitochondrial ratiometric-pHluorin (green, $\lambda_{\text{ex}}=475$ nm; $\lambda_{\text{em}}=525$ nm), and merged overlay. B) Average pH change over time in the cytosol (red) and mitochondria (green, dashed) upon addition of 10 μ M glutamate (arrows) in the presence and absence of 100 μ M ATP ($n=3$). C) Example of a single-cell response. D-E) Hippocampal neurons co-expressing cytosolic mCherryEA and mitochondrial ratiometric-pHluorin. D) Average pH change over time in the cytosol (red) and mitochondria (green, dashed) upon exposure to 15 mM KCl and 10 μ M glutamate for 5 min ($n=11$). E) Example of a single-cell response. Cells were treated with 10 mM NH_4Cl at the end of the experiment to validate the sensor response. Bars indicate std.

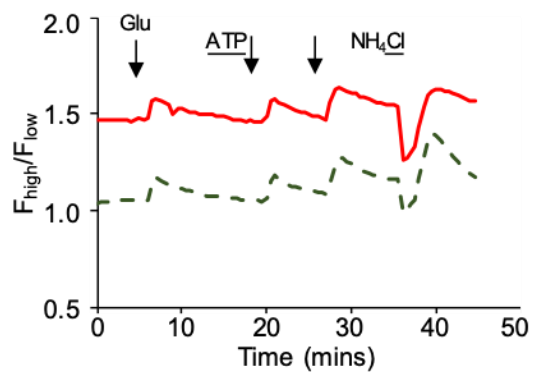
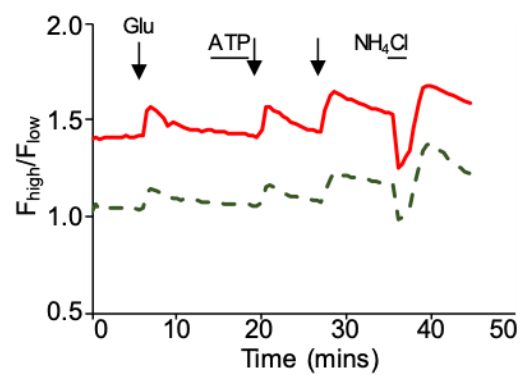
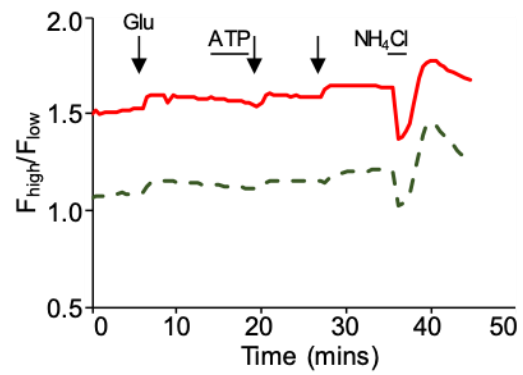


Figure 13 Example of single-cell responses for Figure 8B
pH change was measured over time in cytosol (red) and mitochondria (green, dashed).

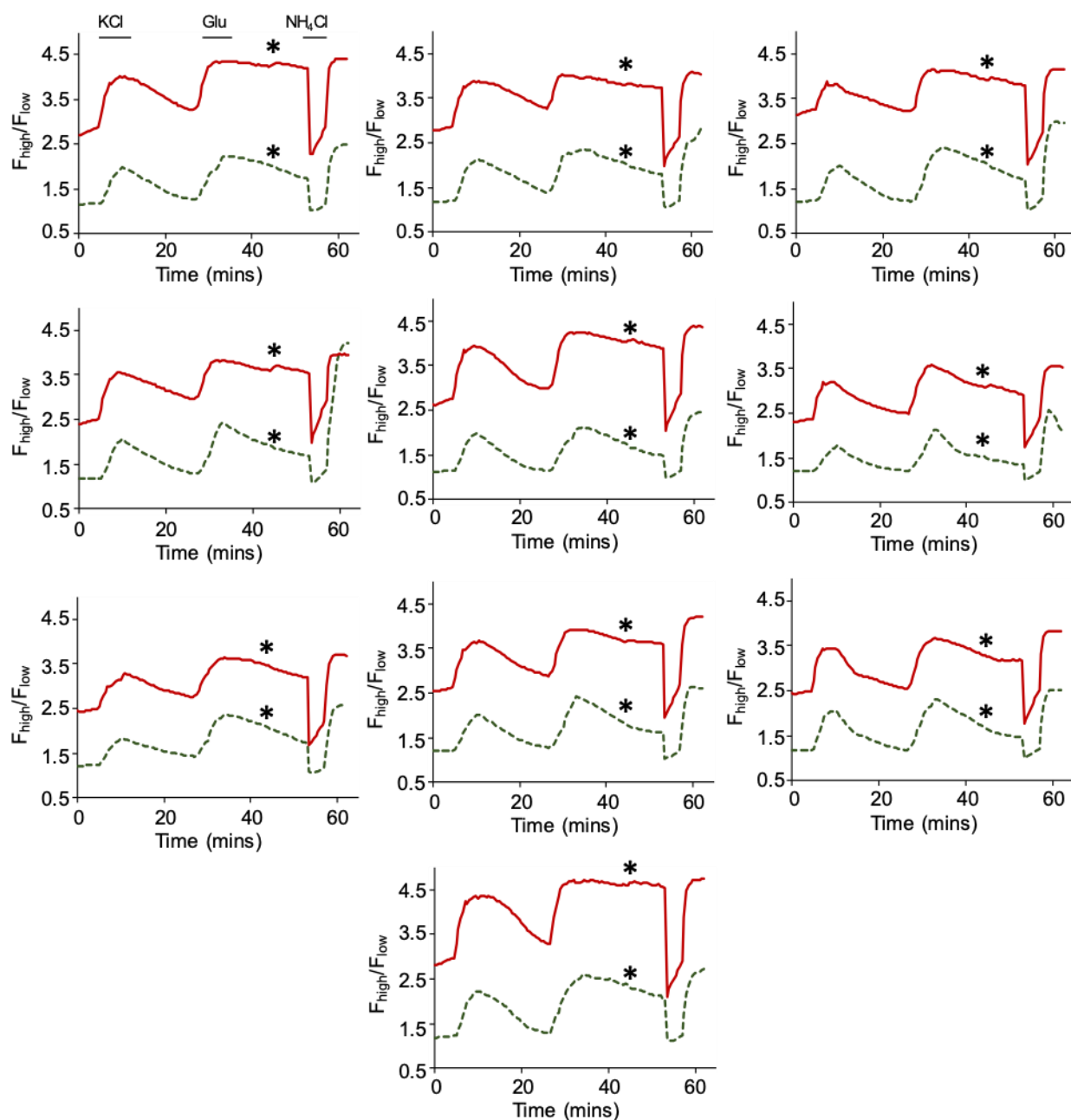


Figure 14 Individual single-cell traces for hippocampal neurons co-expressing mCherryEA in cytosol and ratiometric-pHluorin in mitochondria that were averaged in Figure 8D pH change was measured over time in cytosol (red) and mitochondria (green, dashed) upon exposure to 15 mM KCl and 10 μ M glutamate for 5-6 mins.

We next tested whether simultaneous imaging of mCherryEA and ratiometric-pHluorin could reveal compartment-specific differences in metabolism-dependent pH dynamics. Since the pK_a of mCherryEA also makes it well-suited for studying pH changes in the neutral to alkaline range in mitochondria, and we set out to test the utility of mCherryEA in measuring mitochondrial pH dynamics. We confirmed the efficient localization of mCherryEA and ratiometric-pHluorin using confocal imaging to demonstrate that mCherryEA could be efficiently targeted to the mitochondrial matrix when co-transfected with cytosolic ratiometric-pHluorin (Figure 15). The mCherryEA sensor showed excellent mitochondrial targeting when co-expressed, and therefore we next studied the metabolism dependent pH changes in a neuroblastoma cell line using well-established inhibitors for glycolytic and oxidative phosphorylation pathways^{49,50}.

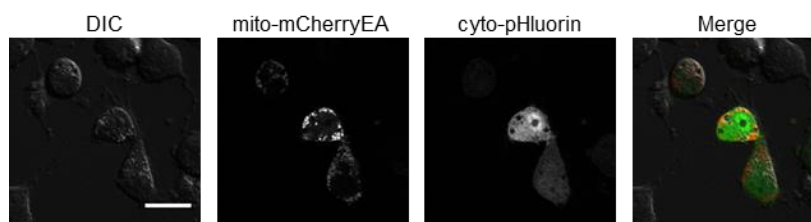


Figure 15 Confocal microscopy

Dual-compartment imaging with mito-mCherryEA and cyto-ratiometric-pHluorin. Scale bar is 20 μm .

2.3.5 Metabolism-dependent pH dynamics

Metabolism and pH are strongly coupled, with perturbations in the metabolic pathway known to cause pH changes^{1,50}. In cancer cells, increased glycolytic activity is known to cause acidification of tumor extracellular environment and alkalinization of the cytosol^{10,12,51}. Recent studies have also implicated a link between organelle pH and oncogenic signaling.^{13,14} For example, Kondapalli *et al.* report increased luminal pH due to mutations in Na^+/H^+ exchanger (NHE9) in patient glioblastomas¹³. However, studies on compartment-specific pH changes in neuroblastoma due to metabolic changes are lacking.

To investigate this with our dual sensor imaging strategy, we studied pH changes in the Neuro2A mouse neuroblastoma cell line co-expressing ratiometric-pHluorin and mitochondria-targeted mCherryEA (Figure 16A-C, Figure 17). Cells were grown in the presence of glucose or in the absence of glucose, using galactose-supplemented media⁵². Cells were then imaged during

sequential treatment with metabolic inhibitors to reveal pH changes linked to glycolysis versus mitochondrial respiration. To inhibit glycolysis, the cells were first exposed to iodoacetic acid (IAA). IAA inhibits the glycolytic enzyme glyceraldehyde-3-phosphate dehydrogenase (GADPH) and is frequently used to inhibit glycolysis in a variety of cell types, including Neuro2A cells, as determined by measurement of ATP, NADH, and other metabolic parameters^{32,53-57}. To next inhibit mitochondrial electron transport and oxidative phosphorylation, cells were exposed to a combination of the mitochondrial membrane ionophore, carbonyl cyanide-p-trifluoromethoxyphenylhydrazone (FCCP), and the ATP synthase inhibitor, oligomycin^{28,58,59}.

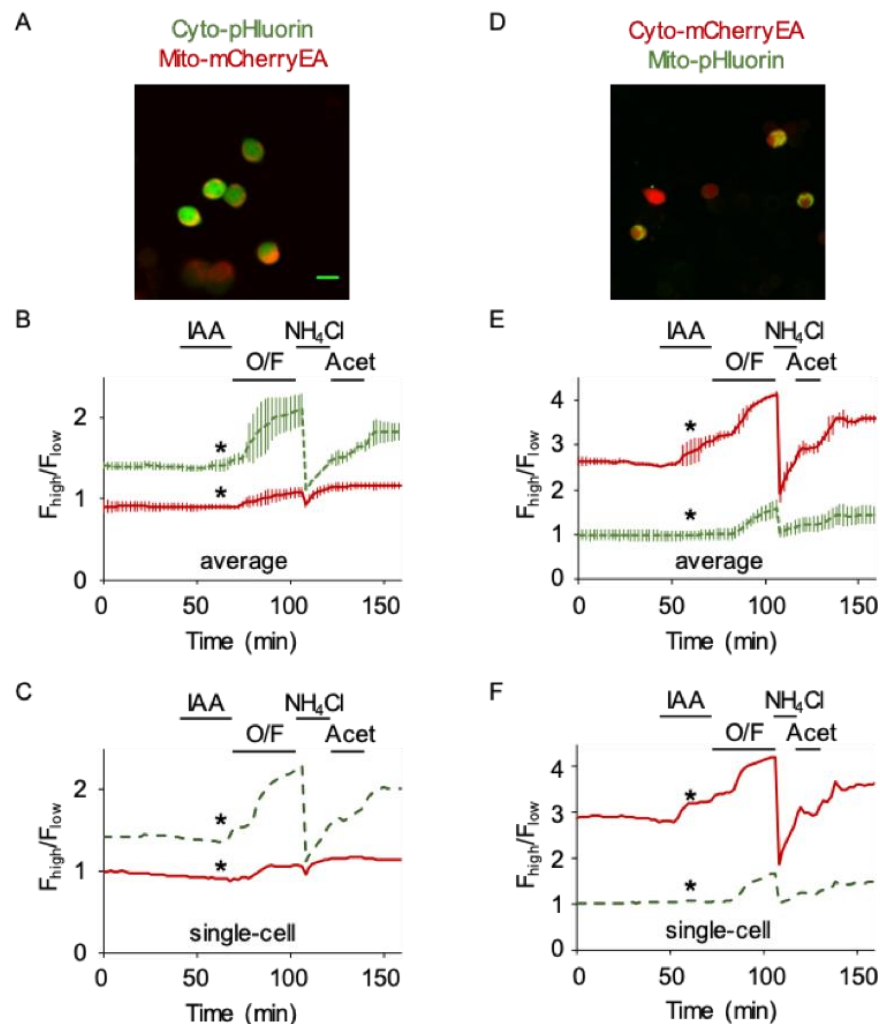


Figure 16 Metabolic inhibition causes differential acidification in the cytosol versus mitochondria
 A) Representative overlay image showing Neuro2A cells expressing cytosolic ratiometric-pHluorin and mitochondria mCherryEA. B) Average pH change over time in the cytosol (green, dashed) and mitochondria (red). Treatment with the glycolytic inhibitor 1 mM iodoacetic acid (IAA) caused minor acidification in the cytosol with significant difference in ratio before and after addition of IAA in individual cells. Though, no acidification was detected in mitochondria (asterisks) for the population, two of the three cells showed significant decrease. Treatment with the mitochondrial inhibitors 5 μ M oligomycin and 1 μ M FCCP (O/F) caused acidification in both compartments, and in particular, the cytosol exhibited a large acidification. (D-F) The metabolism-dependent pH dynamics were independent of the sensor. D) Representative overlay image showing Neuro2A cells expressing cytosolic mCherryEA and mitochondrial ratiometric-pHluorin. (E-F) Similar pH dynamics were observed when the localization of mCherryEA and ratiometric-pHluorin were switched. The sensors were validated at the end of the experiment by adding 30 mM NH₄Cl and 10 mM acetic acid (n=3, 30 cells total). Error bars are stdev. Scale bar is 10 μ m. mCherryEA (red, λ_{ex} =575 nm, λ_{em} =632 nm). ratiometric-pHluorin (green, λ_{ex} = 475 nm, λ_{em} =525 nm)

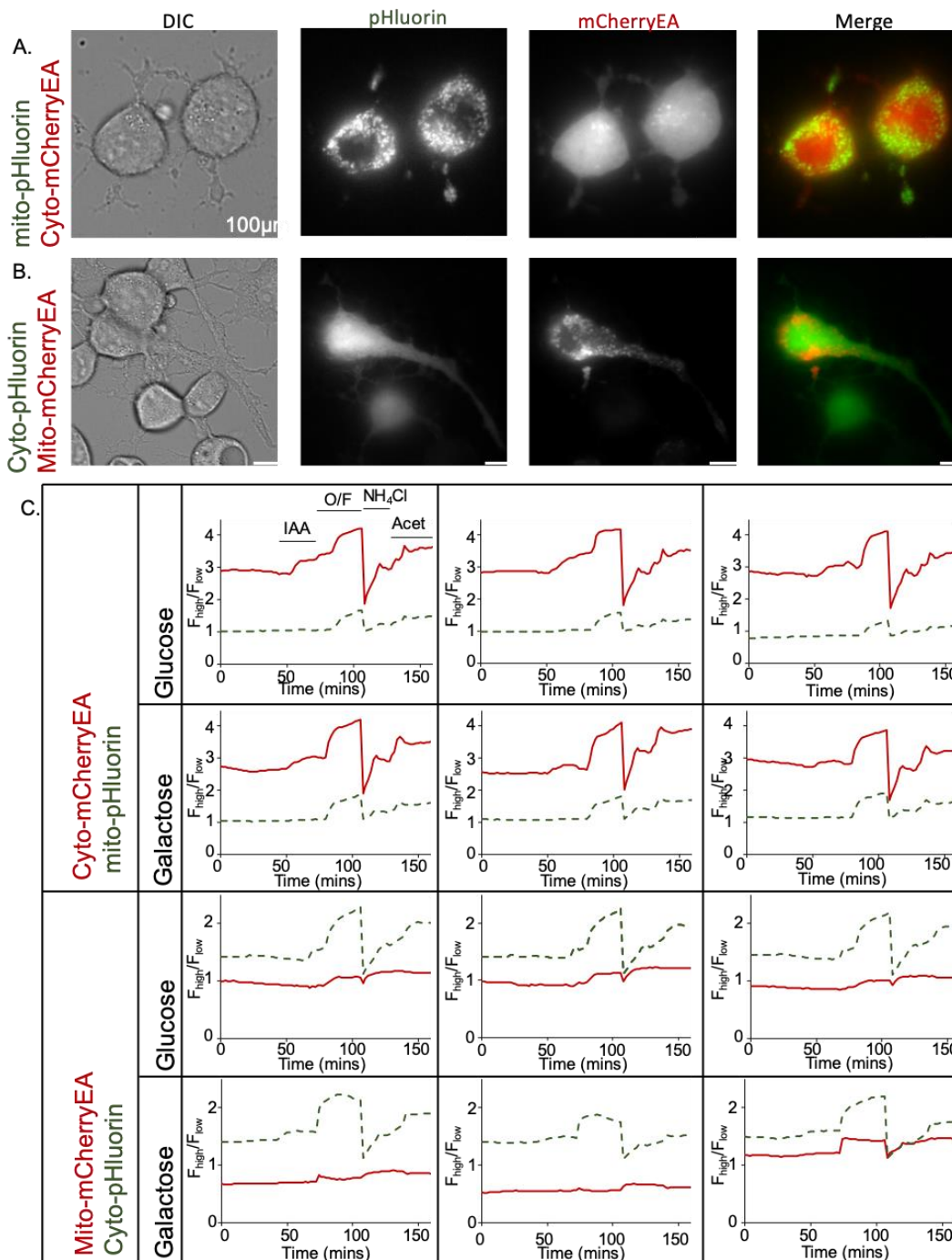


Figure 17 Representative images showing 60X oil magnification of Neuro2A cells expressing A) cytosolic mCherryEA (red, λ_{ex} : 575 nm; λ_{em} : 632 nm) and mitochondria targeted ratiometric-pHLuorin (green, λ_{ex} : 475 nm; λ_{em} : 525 nm). B) Neuro2A cells expressing cytosolic ratiometric-pHLuorin and mitochondria targeted mCherryEA. C) Representative graphs showing changes in individual cells for each condition. IAA: Iodoacetic acid, O/F: Oligomycin/FCCP; NH_4Cl : Ammonium chloride; Acet: Acetic acid. Scale bar is 10 μm .

As expected, metabolic inhibition with 1 mM IAA caused a small decrease in pH in the cytosol, which is consistent with glycolytic inhibition. Although the pH change before (ratio = 1.39 ± 0.04 , mean \pm std, $n=3$) and after (ratio = 1.48 ± 0.05) IAA addition is not significant for the population average ($p=0.28$, $n=3$), the pH change is significant ($p<0.05$) in the cytosol of individual cells, highlighting the power of single-cell analysis to reveal differences obscured by ensemble means. The pH change in the mitochondria before (ratio = 0.90 ± 0.04) and after (ratio = 0.90 ± 0.02) IAA addition was not significant ($p=0.80$) for the population average ($n=3$), but two cells show significant pH decreases ($p \leq 0.015$) (Figure 16B, C). Further calibration would be required to compare the difference in responses between the compartments, but we were clearly able to observe relative pH changes in each compartment. Subsequent treatment with 1 μ M FCCP and 5 μ M oligomycin (O/F) blocked oxidative phosphorylation and caused further acidification in the cytosol (before O/F ratio = 1.48 ± 0.05 ; after O/F ratio = 2.08 ± 0.17 , $p = 0.06$, $n=3$) and also in mitochondria (before O/F ratio = 0.90 ± 0.02 ; after O/F ratio = 1.07 ± 0.05 , $p = 0.02$, $n=3$). Individual cells showed a significant decrease in pH in both the compartments ($p < 0.001$). Although blocking the ATP synthase with oligomycin alone would increase mitochondrial pH, the presence of FCCP causes coupling between mitochondrial and cytosolic pH resulting in acidification of the mitochondria. Interestingly, the metabolism-dependent pH dynamics may be dependent on glycogen stores, fatty acid supply, or gluconeogenic amino acid supply because IAA also caused acidification when glucose is replaced with galactose⁵². The IAA-dependent acidification during galactose replacement indicates that extracellular glucose supply is not strictly required for the effect (Figure 17). However, future metabolic studies will be needed to explore this further.

Importantly, the compartment-specific differences in pH dynamics are consistent with the compartmentation of metabolic processes, and we validated that our observations are not an artifact of the sensors themselves. To do this, we switched the localization of the two sensors, now expressing mCherryEA in the cytosol and ratiometric-pHluorin in the mitochondria. We again observed that FCCP and oligomycin treatment caused the greatest change in pH the cytosol and of the mitochondria compared to IAA treatment, confirming that the compartment-specific pH dynamics are independent of the specific sensor (Figure 16D-F). We cannot interpret the difference between cytosol and mitochondria dynamics because of the dampened dynamic range in mitochondria, but in the future, additional pH calibration of the sensor in mitochondria and other

organelles will enable compartment-specific differences in pH dynamics to be quantified with respect to the physiological process under study.

These studies show the mCherryEA sensor can be used simultaneously with ratiometric-pHluorin to monitor coupled pH changes in two compartments. In addition, the mCherryEA mutant, a ratiometric red pH sensor with a pK_a of 7.3, is well suited for quantitative imaging in neutral to alkaline organelles such as cytosol (pH 7.2), endoplasmic reticulum (pH 7.2), mitochondria (pH 8) and peroxisome (pH 7)¹.

2.4 Discussion and Conclusion

We demonstrated here that mCherryEA is a ratiometric red fluorescent pH sensor that adds to the current toolbox of genetically-encoded indicators available for multicolor live-cell imaging. An excitation ratiometric sensor exhibits two peaks in its fluorescence excitation spectrum, and for fluorescent protein-based sensors the peaks are characteristic of the ionization states of the chromophore. The I158E/Q160A mutant of mCherry was originally engineered by Piatkevich *et al.* to shift the ionization state of the chromophore from the deprotonated to protonated form to generate a Long Stokes Shift (LSS) mutant²⁴. Structural analysis indicated that an aspartate or glutamate at residue 160 could facilitate Excited State Proton Transfer (ESPT), and therefore the I160E mutation was made to create a proton-relay network between S158, E160, and the hydroxyl group of the chromophore²⁴. ESPT mutants have been similarly engineered for LSS mutants of mCherry and other RFPs^{24,60}. Piatkevich *et al.* also showed that the E160 interacts with solvent protons²⁴, and we showed here that this interaction makes it a suitable solvent pH sensor. In a similar manner, pHluorin was engineered using the S202H mutation in wildtype GFP. Although wildtype GFP exhibits excitation peaks characteristic of the protonated and deprotonated states, it does not exhibit a ratiometric shift in ionization in response to pH changes. Like the engineered glutamate in mCherryEA, the residue S202, which is involved in the proton-relay network, was mutated to histidine (pK_a= 6.0) in pHluorin to increase its sensitivity to solvent pH. Thus, our work characterizing mCherryEA highlights the utility of engineering ESPT mutants of RFPs to generate new pH sensors.

Interestingly, in our characterization of mCherryEA, we found that despite the low quantum yield and extinction coefficient measured from the purified protein, the brightness of mCherryEA

expressed in live cells was comparable to pHRed under same imaging conditions. Similar photophysical and photochemical differences between solution studies versus live-cell studies have been observed for other fluorescent protein biosensors, but the exact causes are not well understood^{27,30}. We then compared the pH sensing characteristics of mCherryEA to two other single fluorescent protein-based pH sensors. We found that mCherryEA has a more alkaline pK_a of 7.3 compared to both ratiometric-pHluorin and pHRed, making mCherryEA useful for monitoring pH changes in neutral to alkaline compartments. We also found that the dynamic range for mCherryEA (4-fold change) is comparable to ratiometric-pHluorin and several commonly used FRET sensors such as AKAR, EKAR, and JNKAR, which show 1.2-2 fold change in cells⁶¹⁻⁶³. In the future, further mutagenesis could help improve the dynamic range of mCherryEA to be comparable to the multidomain green fluorescent pH sensor SypHer (10 fold change)^{17,27} (Figure 6) and other FRET-based sensors such as the calcium sensor Twitch (4-10 fold change)⁶⁴.

A major contribution of mCherryEA is to enable multicolor live-cell imaging because it is red fluorescent and should be compatible with green fluorescent sensors. As a proof-of-concept, we simultaneously imaged mCherryEA and ratiometric-pHluorin in different compartments in live neurons and neuroblastoma cells. We demonstrated that the negligible spectral crosstalk between mCherryEA and ratiometric-pHluorin makes it possible to measure pH changes in the cytosol and mitochondria of the same cell. We observed relative changes in compartment-specific pH that correlated with neuronal activity and metabolic inhibition. However, because the sensors show decreased dynamic range in mitochondria, we could not directly compare the differences in pH between compartments. In order to compare pH changes between organelles, it is necessary to carry out an *in situ* pH calibration at the end of each experiment on a cell-by-cell basis, as demonstrated by Poburko *et al* for example¹⁷. We demonstrate that *in situ* calibrations can be done with cytosolic or mitochondrial-targeted mCherryEA using nigericin and monensin. However, we also found that nigericin and monensin can cause extensive cell death after long metabolic manipulations or with primary neuron cultures, precluding our ability to carry out *in situ* calibrations in some scenarios. In the absence of calibrated measurements, mCherryEA can still be used to observe relative changes in pH within a compartment.

In conclusion, we demonstrated that the mCherryEA mutant is a red fluorescent, ratiometric pH sensor with pK_a of 7.3, which is more alkaline than other red fluorescent pH sensors such as pHRed. It can be used to measure compartment-specific pH changes simultaneously with green

fluorescent pH sensors such as ratiometric-pHluorin in several different cell types, and in principle it is spectrally compatible with sensors of other analytes that utilize blue, cyan, green, or yellow fluorescent proteins.

2.5 References

1. Casey, J. R., Grinstein, S. & Orlowski, J. Sensors and regulators of intracellular pH. *Nat. Rev. Mol. Cell Biol.* **11**, 50–61 (2010).
2. Wu, M. M. *et al.* Mechanisms of pH Regulation in the Regulated Secretory Pathway. *J. Biol. Chem.* **276**, 33027–33035 (2001).
3. Sinning, A. & Hübner, C. A. Minireview: PH and synaptic transmission. *FEBS Lett.* **587**, 1923–1928 (2013).
4. Nicholls, D. G. & Budd, S. L. Mitochondria and Neuronal Survival. *Physiol. Rev.* **80**, 315–360 (2000).
5. Chesler, M. & Kaila, K. Modulation of pH by neuronal activity. *Trends Neurosci.* **15**, 396–402 (1992).
6. Rossano, A. J., Chouhan, A. K. & Macleod, G. T. Genetically encoded pH-indicators reveal activity-dependent cytosolic acidification of Drosophila motor nerve termini in vivo. *J. Physiol.* **591**, 1691–1706 (2013).
7. KannR, O. Mitochondria and Neuronal Activity. *Am. J. Physiol. - Cell Physiol.* **292**, (2010).
8. Deitmer, J. W. & Rose, C. R. pH regulation and proton signalling by glial cells. *Prog. Neurobiol.* **48**, 73–103 (1996).
9. Webb, B. A., Chimenti, M., Jacobson, M. P. & Barber, D. L. Dysregulated pH: a perfect storm for cancer progression. *Nat. Rev. Cancer* **11**, 671–677 (2011).
10. Helmlinger, G., Sckell, A., Dellian, M., Forbes, N. S. & Jain, R. K. Acid production in glycolysis-impaired tumors provides new insights into tumor metabolism. *Clin. Cancer Res.* **8**, 1284–91 (2002).
11. Estrella, V. *et al.* Acidity generated by the tumor microenvironment drives local invasion. *Cancer Res.* **73**, 1524–35 (2013).
12. Schornack, P. A. & Gillies, R. J. Contributions of cell metabolism and H⁺ diffusion to the acidic pH of tumors. *Neoplasia* **5**, 135–45
13. Kondapalli, K. C. *et al.* A leak pathway for luminal protons in endosomes drives oncogenic signalling in glioblastoma. *Nat. Commun.* **6**, 6289 (2015).

14. Di Domenico, F. *et al.* Expression of human papilloma virus type 16 E5 protein in amelanotic melanoma cells regulates endo-cellular pH and restores tyrosinase activity. *J. Exp. Clin. Cancer Res.* **28**, 4 (2009).
15. Han, J. & Burgess, K. Fluorescent indicators for intracellular pH. *Chem. Rev.* **110**, 2709–2728 (2009).
16. Miesenböck, G., De Angelis, D. a & Rothman, J. E. Visualizing secretion and synaptic transmission with pH-sensitive green fluorescent proteins. *Nature* **394**, 192–5 (1998).
17. Poburko, D., Santo-Domingo, J. & Demaurex, N. Dynamic regulation of the mitochondrial proton gradient during cytosolic calcium elevations. *J. Biol. Chem.* **286**, 11672–11684 (2011).
18. Li, Y. & Tsien, R. W. pHTomato, a red, genetically encoded indicator that enables multiplex interrogation of synaptic activity. *Nat. Neurosci.* **15**, 1047–53 (2012).
19. Shen, Y., Rosendale, M., Campbell, R. E. & Perrais, D. pHuji, a pH-sensitive red fluorescent protein for imaging of exo- and endocytosis. *J. Cell Biol.* **207**, (2014).
20. Johnson, D. E. *et al.* Red fluorescent protein pH biosensor to detect concentrative nucleoside transport. *J. Biol. Chem.* **284**, 20499–20511 (2009).
21. Tantama, M., Hung, Y. P. & Yellen, G. Imaging intracellular pH in live cells with a genetically encoded red fluorescent protein sensor. *J. Am. Chem. Soc.* **133**, 10034–10037 (2011).
22. Rosselin, M., Santo-Domingo, J., Bermont, F., Giacomello, M. & Demaurex, N. L-OPA1 regulates mitoflash biogenesis independently from membrane fusion. *EMBO Rep.* **18**, 451–463 (2017).
23. Godinho, L. F. & Schrader, M. Determination of Peroxisomal pH in Living Mammalian Cells Using pHRed. in *Peroxisomes: Methods and Protocols, Methods in Molecular Biology* (ed. Schrader, M.) **1595**, 181–189 (Springer New York, 2017).
24. Piatkevich, K. D., Malashkevich, V. N., Almo, S. C. & Verkhusha, V. V. Engineering ESPT Pathways Based on Structural Analysis of LSSmKate Red Fluorescent Proteins with Large Stokes Shift. *J. Am. Chem. Soc.* **132**, 10762–10770 (2010).
25. Filippin, L. *et al.* Improved strategies for the delivery of GFP-based Ca²⁺ sensors into the mitochondrial matrix. *Cell Calcium* **37**, 129–136 (2005).
26. Xia, Z., Dudek, H., Miranti, C. K. & Greenberg, M. E. Calcium Influx via the NMDA Receptor Induces Immediate Early Gene Transcription by a MAP Kinase/ERK-Dependent Mechanism. *J. Neurosci.* **16**, 5425–5436 (1996).
27. Matlashov, M. E. *et al.* Fluorescent ratiometric pH indicator SypHer2: Applications in neuroscience and regenerative biology. *Biochim. Biophys. Acta - Gen. Subj.* **1850**, (2015).

28. Abad, M. F. C., Di Benedetto, G., Magalhães, P. J., Filippin, L. & Pozzan, T. Mitochondrial pH Monitored by a New Engineered Green Fluorescent Protein Mutant. *J. Biol. Chem.* **279**, 11521–11529 (2004).
29. Shaner, N. C. *et al.* Improved monomeric red, orange and yellow fluorescent proteins derived from *Discosoma* sp. red fluorescent protein. *Nat. Biotechnol.* **22**, 1567–1572 (2004).
30. Balleza, E., Kim, J. M. & Cluzel, P. Systematic characterization of maturation time of fluorescent proteins in living cells. *Nat. Methods* **15**, 47–51 (2018).
31. Musa-Aziz, R., Jiang, L., Chen, L. M., Behar, K. L. & Boron, W. F. Concentration-dependent effects on intracellular and surface pH of exposing xenopus oocytes to solutions containing NH₃/NH₄⁺. *J. Membr. Biol.* **228**, 15–31 (2009).
32. Tantama, M., Martinez-Francois, J. R., Mongeon, R. & Yellen, G. Imaging energy status in live cells with a fluorescent biosensor of the intracellular ATP-to-ADP ratio. *Nat Commun* **4**, 2550 (2013).
33. Yaginuma, H. *et al.* Diversity in ATP concentrations in a single bacterial cell population revealed by quantitative single-cell imaging. *Sci. Rep.* **4**, (2014).
34. Imamura, H. *et al.* Visualization of ATP levels inside single living cells with fluorescence resonance energy transfer-based genetically encoded indicators. *Proc. Natl. Acad. Sci.* **106**, 15651–15656 (2009).
35. Costantini, L. M., Fossati, M., Francolini, M. & Snapp, E. L. Assessing the Tendency of Fluorescent Proteins to Oligomerize Under Physiologic Conditions. *Traffic* **13**, 643–649 (2012).
36. Katayama, H., Yamamoto, A., Mizushima, N., Yoshimori, T. & Miyawaki, A. GFP-like proteins stably accumulate in lysosomes. *Cell Struct. Funct.* **33**, 1–12 (2008).
37. Shemiakina, I. I. *et al.* A monomeric red fluorescent protein with low cytotoxicity. *Nat. Commun.* **3**, 1204 (2012).
38. Thomas, J. A., Buchsbaum, R. N., Zimniak, A. & Racker, E. Intracellular pH Measurements in Ehrlich Ascites Tumor Cells Utilizing Spectroscopic Probes Generated in Situ. *Biochemistry* **18**, 2210–2218 (1979).
39. Benčina, M. Illumination of the spatial order of intracellular pH by genetically encoded pH-sensitive sensors. *Sensors (Switzerland)* **13**, 16736–16758 (2013).
40. Breckwoldt, M. O. *et al.* Mitochondrial redox and pH signaling occurs in axonal and synaptic organelle clusters. *Sci. Rep.* **6**, 23251 (2016).
41. Lazarenko, R. M., DelBove, C. E., Strothman, C. E. & Zhang, Q. Ammonium chloride alters neuronal excitability and synaptic vesicle release. *Sci. Rep.* **7**, 5061 (2017).

42. Rathje, M. *et al.* AMPA receptor pHluorin-GluA2 reports NMDA receptor-induced intracellular acidification in hippocampal neurons. *Proc. Natl. Acad. Sci.* **110**, 14426–14431 (2013).
43. Magnotta, V. A. *et al.* Detecting activity-evoked pH changes in human brain. *Proc. Natl. Acad. Sci.* **109**, 8270–8273 (2012).
44. Esquivel, G., Schruers, K., Maddock, R., Colasanti, A. & Griez, E. Acids in the brain: a factor in panic? *J. Psychopharmacol.* **24**, 639–647 (2010).
45. Chesler, M., Brien, J. O., Zappala, A., Cicirata, F. & Barrio, L. C. Regulation and Modulation of pH in the Brain. *Brain* 1183–1221 (2008). doi:10.1152/physrev.00010.2003
46. Khakh, B. S. & North, R. A. Neuromodulation by Extracellular ATP and P2X Receptors in the CNS. *Neuron* **76**, 51–69 (2012).
47. Venkatachalam, V. & Cohen, A. E. Imaging GFP-Based Reporters in Neurons with Multiwavelength Optogenetic Control. *Biophys. J.* **107**, 1554–1563 (2014).
48. Azarias, G. *et al.* Glutamate Transport Decreases Mitochondrial pH and Modulates Oxidative Metabolism in Astrocytes. *J. Neurosci.* **31**, 3550–3559 (2011).
49. Perry, S., Norman, J., Barbieri, J., Brown, E. & Gelbard, H. Mitochondrial membrane potential probes and the proton gradient: a practical usage guide. *Biotechniques* **50**, 98–115 (2011).
50. Eisner, D. a., Nichols, C. G., O'Neill, S. C., Valdeolmillos, M. The effect of metabolic inhibition on intracellular calcium and pH in isolated rat ventricular cells. *J. Phys* **411**, 393–418 (1989).
51. Liberti, M. V. *et al.* The Warburg Effect: How Does it Benefit Cancer Cells? *Trends Biochem. Sci.* **41**, 211–218 (2016).
52. Gohil, V. M. *et al.* Nutrient-sensitized screening for drugs that shift energy metabolism from mitochondrial respiration to glycolysis. *Nat. Biotechnol.* **28**, 249–255 (2010).
53. Sabri, M. I. & Ochs, S. Inhibition of Glyceraldehyde-3-Phosphate Dehydrogenase in Mammalian Nerve by Iodoacetic Acid. *J. Neurochem.* **18**, 1509–1514 (1971).
54. Schmidt, M. M. & Dringen, R. Differential effects of iodoacetamide and iodoacetate on glycolysis and glutathione metabolism of cultured astrocytes. *Front. Neuroenergetics* **1**, 1 (2009).
55. Lutas, A., Birnbaumer, L. & Yellen, G. Metabolism Regulates the Spontaneous Firing of Substantia Nigra Pars Reticulata Neurons via K ATP and Nonselective Cation Channels. *J. Neurosci.* **34**, 16336–16347 (2014).

56. Hung, Y. P., Albeck, J. G., Tantama, M. & Yellen, G. Imaging cytosolic NADH-NAD(+) redox state with a genetically encoded fluorescent biosensor. *Cell Metab.* **14**, 545–54 (2011).
57. Kauppinen, R. A. & Nicholls, D. G. Synaptosomal bioenergetics: The role of glycolysis, pyruvate oxidation and responses to hypoglycaemia. *Eur. J. Biochem.* **158**, 159–165 (1986).
58. Tan, B., Xiao, H., Li, F., Zeng, L. & Yin, Y. The profiles of mitochondrial respiration and glycolysis using extracellular flux analysis in porcine enterocyte IPEC-J2. *Anim. Nutr.* **1**, 239–243 (2015).
59. Duchen, M. R. Contributions of mitochondria to animal physiology: from homeostatic sensor to calcium signalling and cell death. *J. Physiol.* **516**, 1–17 (1999).
60. Shen, Y., Chen, Y., Wu, J., Shaner, N. C. & Campbell, R. E. Engineering of mCherry variants with long Stokes shift, red-shifted fluorescence, and low cytotoxicity. *PLoS One* **12**, 1–14 (2017).
61. Allen, M. D. & Zhang, J. Subcellular dynamics of protein kinase A activity visualized by FRET-based reporters. *Biochem. Biophys. Res. Commun.* **348**, 716–721 (2006).
62. Komatsu, N. *et al.* Development of an optimized backbone of FRET biosensors for kinases and GTPases. *Mol. Biol. Cell* **22**, 4647–56 (2011).
63. Fritz, R. D. *et al.* A Versatile Toolkit to Produce Sensitive FRET Biosensors to Visualize Signaling in Time and Space. *Sci. Signal.* **6**, rs12–rs12 (2013).
64. Thestrup, T. *et al.* Optimized ratiometric calcium sensors for functional in vivo imaging of neurons and T lymphocytes. *Nat. Methods* **11**, (2014).

CHAPTER 3. QUANTIFYING ACUTE FUEL AND RESPIRATION DEPENDENT PH HOMEOSTASIS IN LIVE CELLS USING THE MCHERRY MUTANT AS A FLUORESCENCE LIFETIME SENSOR

Reprinted with permission from *Analytical Chemistry*. Haynes, E.P., Rajendran, M., Henning, C.K., Mishra, A., Lyon, A., and Tantama, M. (2019). Quantifying acute fuel and respiration dependent pH homeostasis in live cells using the mCherryTYG mutant as a fluorescence lifetime sensor, *Analytical Chemistry*. Copyright 2019 American Chemical Society.

3.1 Introduction

The measurement of fluorescence lifetime is one of the most important approaches to obtaining quantitative information from endogenous or exogenous reporters in biological specimens^{1,2}. However, fluorescence lifetime-based pH sensors have not been widely developed compared to fluorescence intensity or ratiometric probes. New approaches to live-specimen measurement are important because pH is a fundamental physiological parameter that is relevant to molecular biology³, microbiology⁴⁻⁷, cancer biology⁸, neuroscience⁹, and immunology¹⁰ with applications in drug delivery¹¹ and bioproduction^{7,12}. For example, in microbiology the proper measurement of pH remains key to answering open questions about homeostasis, environmental adaptation, and antibiotic resistance mechanisms in pathogenic bacteria such as *Escherichia coli*^{4,13-16}. Measurements of cellular pH have provided insights into the underlying microbial physiology. For example, how decarboxylases, sigma factor, and other stress response systems enable *E. coli* to survive the acidic and basic environments of the mammalian gut^{4,13-16}. These studies in turn provide foundations for the growing understanding that metabolic factors, such as respiratory capacity and proton motive force, contribute to the action of different types of antimicrobials^{17,18}. In many of these studies, extracellular pH is monitored with electrodes or other physiochemical methods, with a growing use of fluorescent sensors to measure intracellular pH in living cells.

Fluorescent pH sensors have long been important in deciphering the physiology of prokaryotes and eukaryotes¹⁹⁻²¹. Small pH-sensitive organic dyes such as BCECF and SNARF²² have been widely used, but dye loading, leakage, and non-specific binding to proteins and membranes can limit their application. In contrast, pH sensors based on fluorescent proteins (FPs) have grown in popularity because they are genetically-encoded and can be used in a range of cell

types and species with targeting ability to organelles and subcellular locations. However, current FP-based pH sensors still need improvement. For example, commonly-used sensors, such as pHluorin and SypHer, utilize green and yellow FP variants^{23,24}. Unfortunately, their color overlaps with the color of most other fluorescent sensors, precluding multiplexed experiments with more than one probe²¹. Therefore, it is important to develop new red fluorescent protein (RFP) pH sensors, but only a few have been developed thus far²⁵⁻²⁹. Furthermore, the current FP pH sensors rely on single-channel intensity or two-channel ratio readouts. Single-channel intensity sensors such are excellent for detecting events such as vesicle release in which large pH changes occur³⁰, but they are not ideal for quantifying pH due to high signal variability with expression level. Ratiometric sensors overcome this problem by normalizing for expression level via the ratio of two distinct spectral peaks. However, the ratio can depend on excitation power and filter bandwidths, and they occupy a greater spectral space that can also limit multiplex measurements.

In contrast, fluorescence lifetime is an intrinsic property that offers a single-channel measurement that is independent of sensor concentration. Notably, lifetime measurements have proven highly robust and reproducible across different labs using different instrumentation, which facilitates direct quantitative comparisons of results between studies³¹. One challenge, however, is that the application of fluorescence lifetime sensing in biology turned its focus toward fluorescence lifetime imaging microscopy (FLIM) early on^{32,33}. FLIM offers great spatial resolution and molecular specificity for a number of analytes^{34,35} including protons^{28,36-38}, but in practice it is not yet a widely accessible technique because of the requirement for expensive commercial or custom-built systems. However, in many studies, high spatial resolution is not required to obtain critical understanding of live-cell physiology, and population measurements are entirely sufficient. Important alternative techniques are being developed, such as fluorescence lifetime flow cytometry and microfluidic methods^{39,40}. Alternatively, steady-state spectroscopy of live-cell suspensions has proven highly effective for studying the physiology of in bacteria⁴¹⁻⁴³, yeast^{44,45}, and mammalian cells^{46,47}, but the time-resolved modality has not been exploited until now.

In this study, we demonstrate mCherryTYG can quantitatively report pH in live cells with its fluorescence lifetime. Although wildtype mCherry is pH insensitive, it is the most widely used RFP and has low cytotoxicity, thus providing an appropriate scaffold for an RFP pH sensor⁴⁸. The M66T mutant, mCherryTYG, is pH sensitive²⁷ but it has not yet been used as a quantitative sensor. We find that it matures efficiently, corroborated by a high-resolution crystal structure that we

obtained showing clear electron density for its chromophore. With solution and live cell studies, we demonstrate that this sensor exhibits an incredibly large dynamic range with a 2 ns lifetime change from pH 5 to 9. In a further demonstration of its applications, we use mCherryTYG to show that bacterial pH regulation is acutely dependent on fuel and aerobic respiration, using live cell suspension cultures with single-color and dual-color multiplexed measurements for the first time.

3.2 Methods

3.2.1 Materials

Unless otherwise noted, chemicals were purchased from Sigma Aldrich, enzymes were purchased from New England Biolabs (NEB), and cell culture media and supplements were purchased from ThermoFischer (Invitrogen).

3.2.2 Molecular Biology

The wildtype mCherry gene was mutated to mCherryTYG using the NEB Q5 Mutagenesis kit (forward primer: ACCTACGGTTCCAAGGCCTACGTGAAG; reverse primer: GAACTGAGGGGACAGGATG) within the pRSETB bacterial expression vector or the GW1 mammalian expression vector. The mCherryTYG-mTurquoise2 fusion was constructed by linearizing the GW1-mCherryTYG plasmid with BsrGI, amplifying the mTurquoise2 gene by PCR (forward primer: AGTAAGAATTCGAAGCTTGTGATCATAATCAGCCATAACCACATT; reverse primer: AGCTCGTCCATGCCGC) to add compatible overlaps, and the NEB HiFi kit was used to insert mTurquoise2 on the C-terminal end of mCherryTYG via a Gibson reaction. mTurquoise2-N1 was a gift from Michael Davidson & Dorus Gadella (Addgene plasmid # 54843).

3.2.3 Protein Expression and Purification

The pRSETB-mCherryTYG plasmid was transformed into BL21(DE3) E. coli cells and grown in Autoinduction Media (Formedium) at 37 °C in baffled flasks with continuous shaking overnight for 12-16 hours followed by 2-3 days of continuous shaking at ambient temperatures. Cells were pelleted at 6,000xg and stored at -80 °C until purification. His-tagged protein was purified by nickel-affinity chromatography using a HiTrap IMAC column (Amersham) according to manufacturer instructions. Purified protein was dialyzed against storage buffer (5 mM MOPS, 300

mM NaCl, 10% glycerol, pH 7.3), concentrated to 500 μ L using a 10,000 MWCO Amicon Centrifugal Filter (Millipore), and stored at -20 °C for immediate use or -80 °C for extended storage. Protein produced for crystallization was further polished by size-exclusion chromatography using tandem Superdex S200 columns (GE Healthcare) pre-equilibrated with 50 mM HEPES pH 7.9 (Shu et al 2006). Fractions containing mCherryTYG were pooled and concentrated to 20 mg/mL for crystallization.

3.2.4 Steady-State Fluorescence Spectroscopy

pH titrations were performed by diluting protein to 0.2 - 1 μ M in assay buffer containing 50 mM Tris, 50 mM Bis-Tris, 50 mM MOPS adjusted to pH 5.5 - 9.0 with NaOH or HCl at half unit steps. Fluorescence was measured on a microplate reader (Biotek synergy H5). Emission spectra were measured using a monochromator with fixed excitation at 540/9 nm and emission scanned from 560 - 700 nm with a 9 nm emission bandpass. Excitation spectra were measured using a monochromator with fixed emission at 600/9 nm and excitation scanned from 480 - 580 nm with a 9 nm excitation bandpass. To test for environmental interference, protein samples were prepared in assay buffer containing either 100mM NaCl, 100 mM KCl, 1 mM MgCl₂, 1mM CaCl₂, 10 μ M H₂O₂ or 30 μ M DTT. The concentration of protein containing mature chromophore was quantified by measuring absorbance of protein after alkaline denaturation in 1M NaOH at 450 nm ($\epsilon = 44000$ M⁻¹·cm⁻¹) as previously described. Absorbance and fluorescence spectra of 5 - 20 μ M protein solutions at different pH were measured. Extinction coefficients were calculated according to the Beer-Lambert equation. Quantum yields were calculated from the slopes from integrated fluorescence (530 nm excitation) vs. absorbance relationships relative to the wildtype mCherry standard.

3.2.5 Crystallization

Crystals were obtained by hanging drop vapor diffusion experiments at 25 °C. Optimal crystallization conditions contained an equal volume of mCherryTYG at 10 mg/mL and well solution containing 50 mM Tris at pH 8.5, 100 mM sodium acetate, and 30% PEG 4000. Crystals were harvested on nylon loops and flash frozen in liquid N₂. X-ray diffraction data was collected at 100 K with an Eiger detector at the Advanced Photon Source LS-CAT 21-ID-D. HKL2000 was used for data integration and scaling. Phaser⁴⁹ was used to solve the structure by molecular

replacement using the mCherry structure (PDB 2H5Q)⁵⁰ as a search model. Manual model building was performed in COOT⁵¹ and altered with refinement in PHENIX⁵². The correctness of the final structure was determined using MolProbity⁵². Structure figures were generated using PyMol.

3.2.6 Time-Resolved Spectroscopy with Purified Protein

The mCherryTYG protein samples were diluted to 0.2 - 1 μ M in assay buffer. Fluorescence decays were measured by time-correlated single-photon counting (TCSPC) on a FS5-TCSPC+ (Edinburgh Instruments) with a Fianium WhiteLaseMicro supercontinuum laser (20 MHz repetition rate). All mCherryTYG lifetimes were measured with 546/10nm excitation and 580/10 nm emission. Typically, a neutral density filter was used to adjust count rates to 100,000 to 200,000 counts per second to avoid photon pileup artifacts, and typically at least 1,000,000 total photons were counted for peak counts of 1,000 - 5,000 photons to obtain well-defined decays. The instrument response function (IRF) was measured using LUDOX suspensions, and IRFs were collected to match total counting time and background counts of the fluorescent samples. Lifetime decay time constants were calculated by reconvolution fitting using the Fluoracle software (Edinburgh Instruments), and the lifetime value was calculated as the weighted average of the decay time constants. The pK_a values were determined by fitting pH data to a Boltzmann function.

3.2.7 Time-Resolved Spectroscopy with Live Cell Suspensions

Leaky expression of the fluorescent protein sensors was sufficient for live-cell experiments in DH5 α *E. coli*. Bacteria were washed and diluted to an OD of 0.3 - 0.5 in 1.5 mL of continuously stirred M63 minimal medium (0.4 g/L KH₂PO₄, 2 g/L (NH₄)₂SO₄, 7.45 g/L KCl) buffered to the desired pH with 50 mM MES for pH 5.5 to 6.5, MOPS for pH 7.0 to 7.5, and Tris for pH 8.0 to 9.0. For live-cell pH calibration curves, IRFs were measured and reconvolution fitting was carried out to determine the lifetimes. For time course experiments, the empirical tail mean lifetime was measured to facilitate automated analysis. Empirical tail mean lifetimes were calculated as the photon count-weighted average lifetime for the 15 ns window after the peak. The pH calibration curve for the empirical mean lifetime (Figure 23) is comparable to the lifetimes obtained by IRF reconvolution fitting. Live-cell suspension treatments were added directly to stirring suspensions at final concentrations of 10 mM glucose, 10 mM KCN, 0.8% glycerol, and 40 mM benzoate and 40 mM methylamine. For simultaneous measurements of intracellular ATP and pH, cells

expressing mCherryTYG and ATeam1.03YEMK were mixed. The ATeam1.03YEMK CFP donor lifetime was measured using 435/10 nm excitation with 485/10 nm emission. For simultaneous measurements of intracellular and extracellular pH, cells expressing mCherryTYG were diluted in M63 media containing 50 - 100 nM purified EGFP protein. The EGFP lifetime was measured using 475/10 nm excitation and 510/10 nm emission.

3.2.8 Mammalian Cell Culture, Transfection, and Live-Cell Imaging

HEK-293 cells were cultured at 37 °C in 5% CO₂ humidified air incubator in DMEM media containing 10% Cosmic calf serum (Hyclone). Cells were transfected using calcium phosphate and imaged after 2 days. Cells were imaged in high potassium imaging solution (mM: 1.25 NaH₂PO₄, 125 KCl, 2 CaCl₂, 1 MgCl₂, 10 glucose) containing 2.5 μM nigericin and buffered to pH 5.5 to 9.0. The mCherryTYG fluorescence images were collected using 550/15 nm excitation, 570 nm longpass dichroic, and 585/20 nm emission filters. The mTurquoise2 fluorescence images were collected using 438/29 nm excitation, multiband dichroic, and 470/20 nm emission filters.

3.3 Results

3.3.1 Structural analysis of mCherryTYG

We solved the X-ray crystal structure of mCherryTYG to a resolution of 1.09 Å, which allowed us to unambiguously determine the maturation state of its chromophore (Figure 18). The mCherryTYG mutant contains the M66T mutation found in mOrange that causes an additional cyclization of its chromophore (Figure 19)^{50,53}. In mOrange the threonine mutation positions the side chain hydroxyl for a nucleophilic attack on the backbone amide, creating an oxazole ring. The oxazole ring partially disrupts the fully extended chromophore conjugation system found in DsRed-type RFPs, which results in the shift to orange color. Here, the M66T mutation has the same effect on chromophore maturation, generating an oxazole ring but in the context of the overall mCherry scaffold (Figure 18). This chromophore mutation did not significantly alter the overall structure of the protein as compared to the previously determined wildtype mCherry structure (0.098 Å root mean square deviation for the C α atoms of residues 4-225)⁵⁰. However, it still induces a shift in the pK_a of the chromophore (Table 4), and protonation of the chromophore at near neutral pH causes a characteristic shift to a lower wavelength peak in the pH-dependent absorption spectrum (Figure 20)⁵⁴. Taken together, these results are consistent with the idea that the pK_a shift of the

chromophore phenolic proton is caused primarily by decreased π -electron density in the conjugated chromophore system. In addition to the chromophore itself, structural differences were observed at residues Glu215, discussed below, and Lys70 (Figure 19).

Comparison of our structure for mCherryTYG (pH 8.5) with those of wildtype mCherry (PDB 2H5Q, pH 8.5) and mOrange (PDB 2H5O, pH 8.2) reveal two distinct conformations for the glutamate 215 side chain, contributing to changes in the local electrostatic environment of the chromophore. In wildtype mCherry, the Glu215 side chain is within hydrogen bonding distance 2.7 Å from the imidazolinone ring nitrogen of the chromophore; however, in mOrange, this side chain is rotated 1 Å away from the chromophore nitrogen and instead hydrogen bonds with the interior network of waters. The electron density of mCherryTYG reveals ~50% occupancy of Glu215 in two conformations, one of which is consistent with wildtype mOrange and the other with mCherry (Figure 18). In the wildtype mCherry conformation Glu215 is protonated, acting as the hydrogen bond donor to the chromophore nitrogen; whereas in the mOrange conformation, Glu215 is deprotonated and acts as the acceptor in its hydrogen bond to water. Importantly, deprotonation of Glu215 is hypothesized to cause the hypsochromic shift in the absorbance and fluorescence spectra of wildtype mCherry at high pH⁵⁰. The spectral shift observed for mCherryTYG is larger than the spectral shift observed for wildtype mCherry^{27,50}. This larger shift is likely caused by the partial occupancy of Glu215 in the anionic state that results in a stronger local electric field around the chromophore, shown to be a major factor in tuning the color of fluorescent proteins⁵⁵. It is also evident that Glu215 in mCherryTYG is titratable in the physiological pH range (Figure 20). Thus, in mCherryTYG the M66T chromophore mutation causes an increase in the structural dynamics of Glu215, which plays an important role in governing the pH-dependent electrostatic environment of the chromophore and is reflected in its steady-state spectral properties. As described below, this behavior did not negatively impact on our ability to use mCherryTYG as a pH sensor, as has been observed for other pH sensors like pHTomato²⁶.

Thus, our X-ray crystal structure of mCherryTYG provides a structural rationale for its steady-state fluorescence properties. Shu *et al.* also noted evidence of incomplete chromophore maturation with the M66T mutation in mOrange, evidenced by green fluorescence⁵⁰. Importantly, we did not observe green fluorescence of mCherryTYG when it was purified for protein studies

nor when expressed in bacteria or mammalian cells, showing that mCherryTYG matures efficiently (Figure 21).

Table 2 Data collection and refinement statistics

Data Collection	
X-ray source	LS-CAT 21-ID-D
Wavelength (Å)	1.088 Å
D _{min} (Å)	20.0– 1.09
Space group	<i>P</i> 12 ₁ 1
Cell dimensions	
a, b, c (Å)	48.8, 42.8, 61.1
α, β, γ (°)	90, 112.2, 90
Total reflections	473,526
Unique reflections	69,505
R _{sym} (%)	0.095 (0.072)
Completeness (%)	93.6 (100.0)
(<i>I</i> /σ)	10.4 (23.1)
Redundancy	6.8 (7.0)
(<i>CC</i> _{1/2})	0.996 (0.993)
Refinement	
Refinement resolution (Å)	20.0 – 1.09
Total reflections used	76,260
RMSD bond lengths (Å)	0.005
RMSD bond angles (°)	1.04
Estimated coordinate error (Å)	0.09
Ramachandran plot	
Favored (%)	98.6
Outliers (%)	0.0
R _{work} /R _{free} (%)	16.7/17.7
Protein atoms	2,168
Ligand atoms	22
Solvent molecules	313
Average B-factor (Å ²)	15.9
Protein	14.3
Ligand	16.6
Solvent	25.3
Wilson B factor (Å ²)	11.7
PDB entry	6M3Z

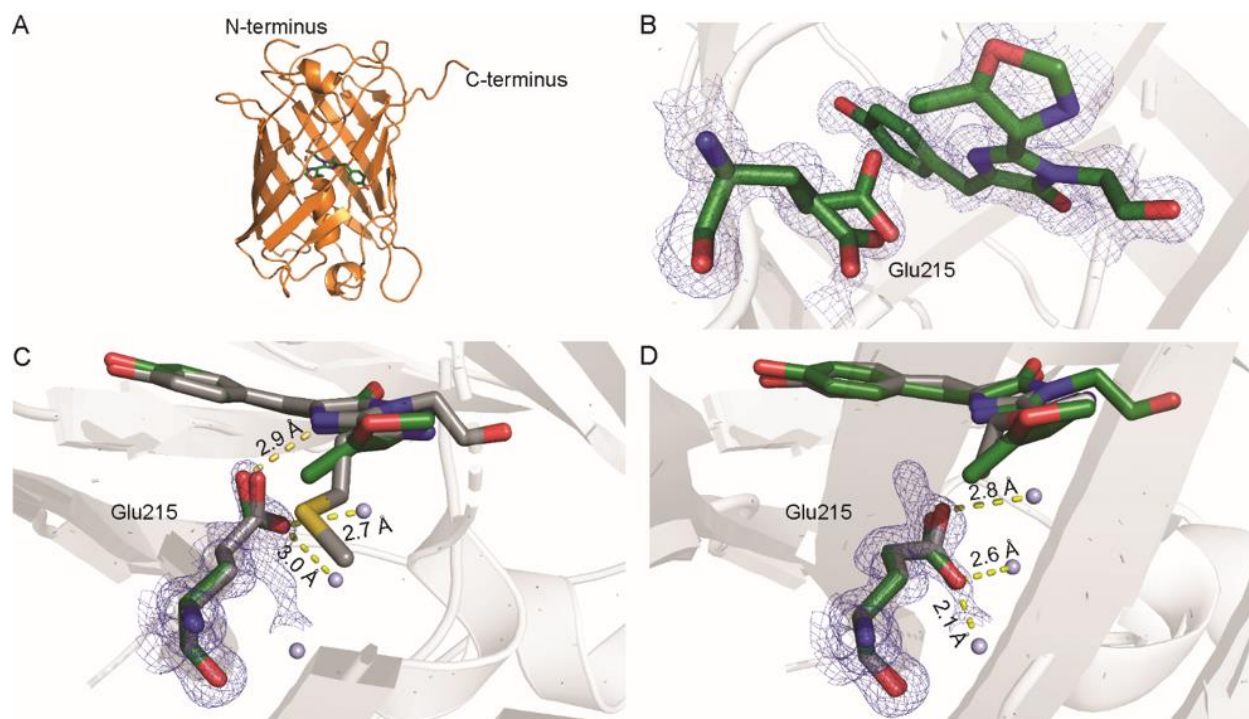


Figure 18 The X-ray crystal structure of mCherryTYG (PDB 6M3Z) with data collection and refinement statistics reported in Table S-2. The (A) overall structure of mCherryTYG crystallized at pH 8.5 is shown with (B) a close-up view of the chromophore environment. The $2|F_o|-|F_c|$ map contoured at 3σ for the chromophore is shown as the blue cage. Electron density for the two major conformations of Glu215 is shown. (C) One conformation resembles that of Glu215 found in wildtype mCherry (PDB 2H5Q, grey overlay), and (D) the second conformation resembles mOrange (PDB 2H5O, grey overlay). Distances between atoms are labeled, and grey spheres are water molecules.

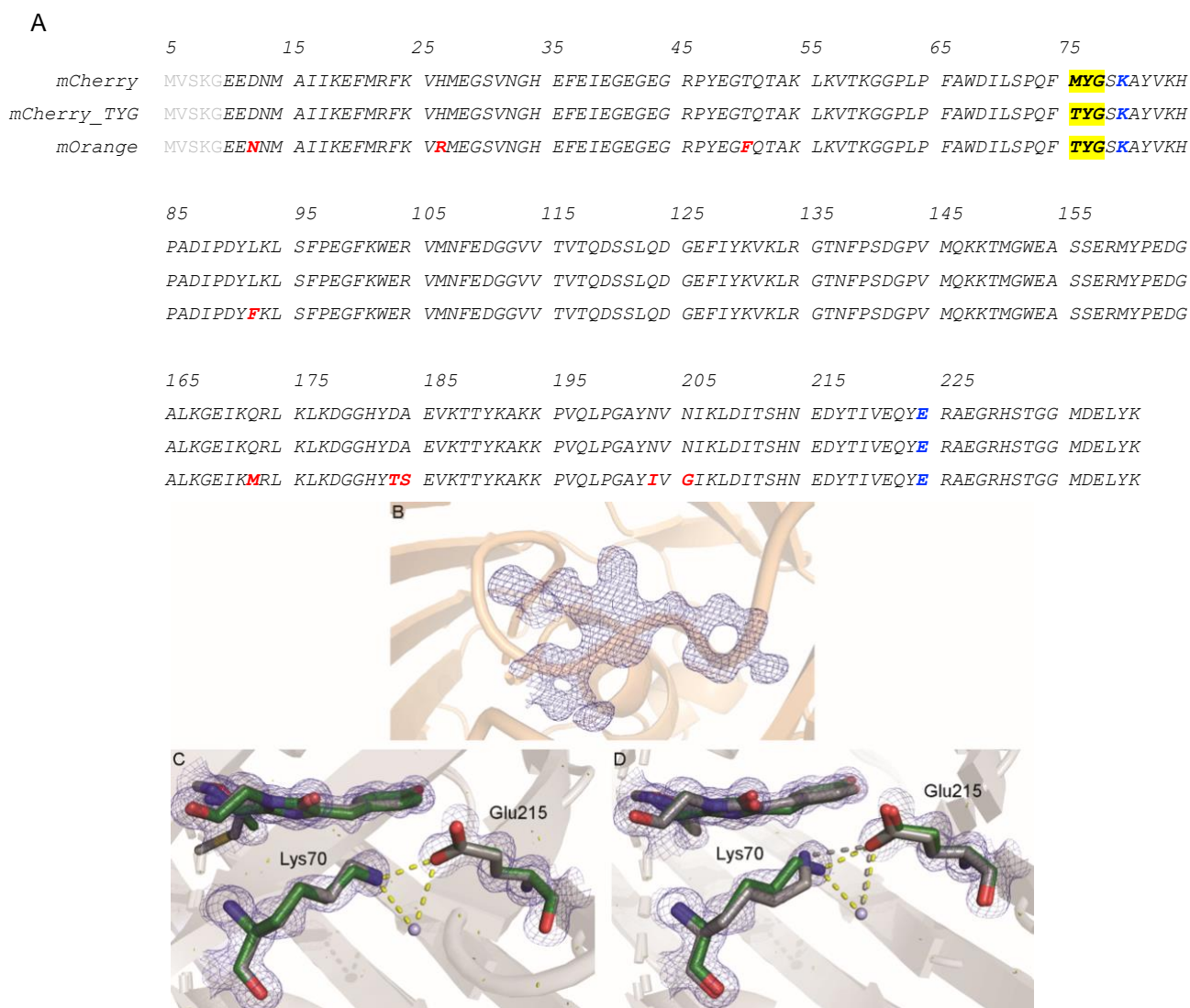


Figure 19 Structural comparison between mCherryTYG, wildtype mCherry, and wildtype mOrange

(A) Protein sequence alignment for the different fluorescent proteins. Chromophore forming residues are highlighted in yellow. mOrange residues that differ from the mCherry scaffold are in bold red font. Conserved residues Glu215 and Lys70 are in bold blue font. (B) Omit map showing the electron density for the mCherryTYG chromophore. (C-D) In addition to Glu215, we also observed structural differences at Lys70. Lys70 is also thought to contribute to the local electric field around the chromophore, and in mCherryTYG residue Lys70 shows small deviations from its positions in wildtype mCherry and mOrange. In mOrange, the charged side chain of Lys70 hydrogen bonds to the same water coordination network interacting with Glu215. However, in mCherryTYG the electron density suggests the conformation of Lys70 more resembles the conformation in wildtype mCherry, and it does not interact with the water coordination sphere observed in mOrange. In mCherryTYG, Lys70 resembles the conformation found in wildtype mCherry (C) whereas mOrange exhibits a different rotamer for Lys70 (D). The mCherryTYG residues are colored green with overlays of (C) wildtype mCherry or (D) mOrange residues in grey.

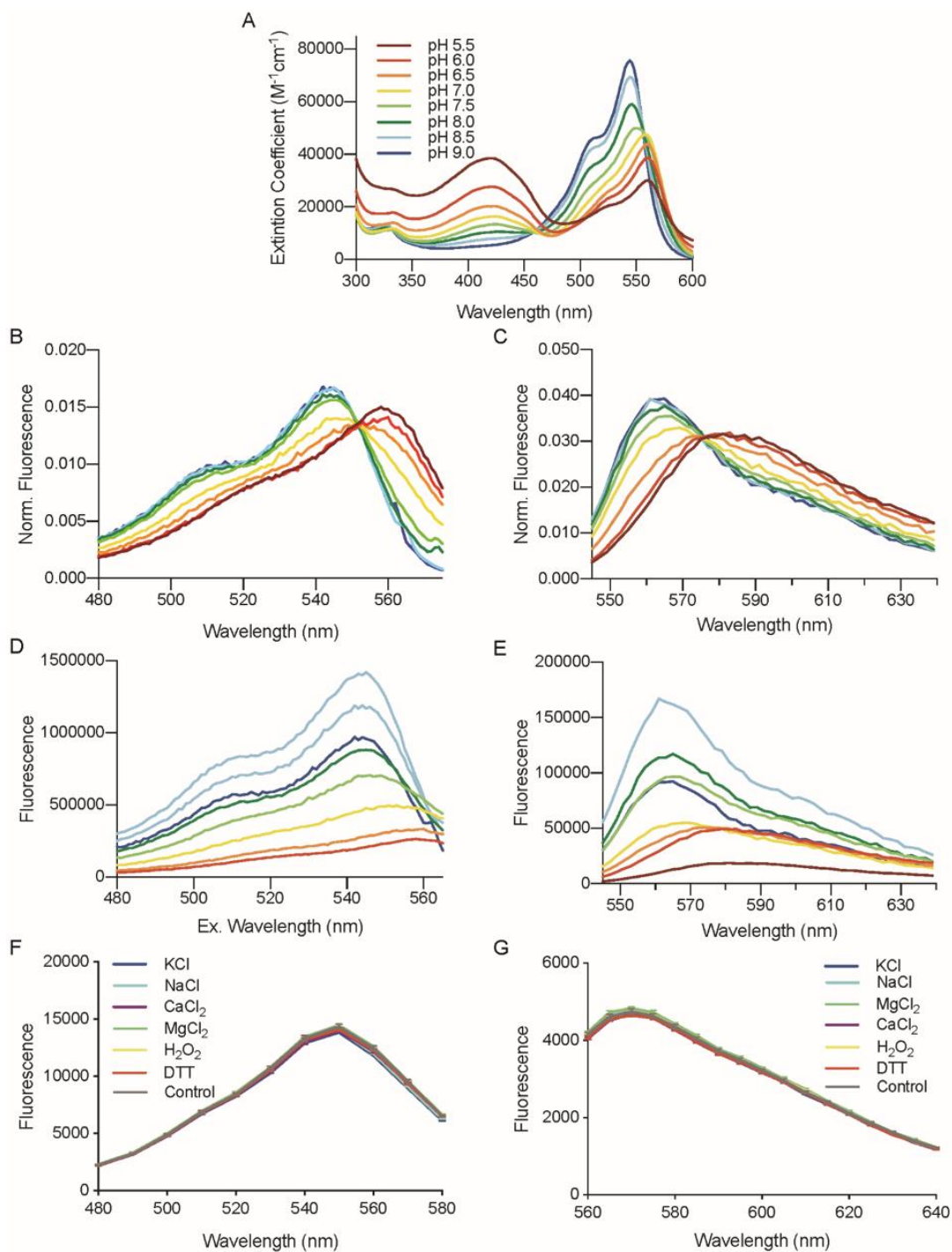


Figure 20 Steady-state fluorescence spectroscopy characterization of mCherryTYG

The pH-dependent spectra were measured, including the (A) absorbance spectra, (B) raw fluorescence excitation spectra, (C) raw fluorescence emission spectra, (D) fluorescence excitation spectra normalized to total fluorescence, and (E) fluorescence emission spectra normalized to total fluorescence. The (F) fluorescence excitation and (G) emission spectra of mCherryTYG demonstrate that it is not sensitive to differences in physiological salts nor differences in redox environment.

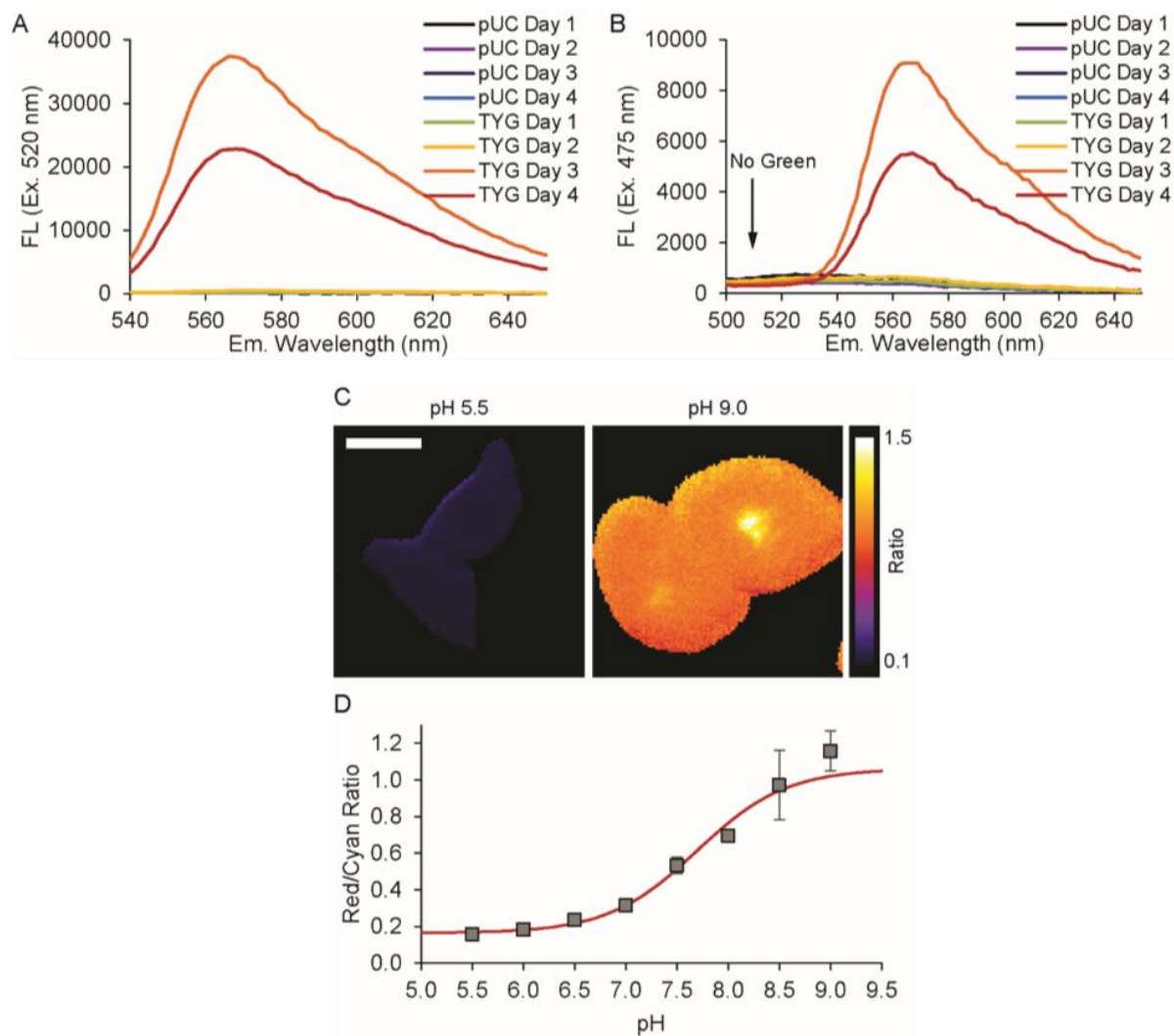


Figure 21 mCherryTYG exhibits efficient maturation to the red fluorescent form (A-B) Expression of mCherryTYG was monitored in live BL21(DE3) *E. coli*. (A) Emission spectra with 520 nm excitation were measured as direct excitation of the red chromophore as a reference. (B) To test if immature green fluorescent chromophore was present at any time point, emission spectra with 475 nm excitation were measured. Bleedthrough excitation of the fully mature red fluorescence chromophore was detected near 570 nm emission (note the 4-fold lower y-axis scale), but no green fluorescence near 510 nm emission was detected in mCherryTYG transformed cells relative to background measured in pUC transformed control cells. Similar results showing no detection of immature green fluorescent chromophore were obtained with DH5a *E. coli* (n=3 for each cell type and plasmid). (C-D) mCherryTYG mature efficiently and is well-behaved when expressed in mammalian cells. HEK293 cells expressing mCherryTYG did not show any evidence of immature green fluorescence. To demonstrate that mCherryTYG maintained pH sensing, we constructed the mCherryTYG-mTurquoise2 fusion as a ratiometric pH sensor. HEK293 cells expressing mCherryTYG-mTurquoise2 were incubated in high potassium imaging solution with the equilibrative H⁺/K⁺ nigericin and buffered at pH 5.5 to 9.0. The ratio of mCherryTYG red fluorescence intensity to mTurquoise2 cyan fluorescence intensity exhibits a pH dependent change with pK_a of 7.7 (mean ± std).

3.4 mCherryTYG is a fluorescence lifetime pH sensor

We next demonstrated that mCherryTYG is an effective pH sensor whether in purified protein or live cells. Steady-state spectroscopy of the protein in solution shows a pH dependence of both the extinction coefficient (ϵ) and fluorescence quantum yield (ϕ) of mCherryTYG (Figure 22). Due to acid quenching from pH 9.0 to pH 5.5, the extinction coefficient decreases from $\epsilon = 55,000 \text{ M}^{-1}\text{cm}^{-1}$ to $\epsilon = 20,000 \text{ M}^{-1}\text{cm}^{-1}$ and the fluorescence quantum yield decreases from $\phi = 0.31$ to $\phi = 0.05$, causing a greater than 16-fold change in brightness. Importantly, although dimming occurs in acidic conditions, even at pH 5.5 data acquisition was not encumbered, allowing for capture of a large biologically relevant pH range. With its large change in quantum yield, we hypothesized that mCherryTYG would exhibit a large change in fluorescence lifetime.

As hypothesized, time-resolved spectroscopy revealed that mCherryTYG shows an exceptionally large pH-dependent fluorescence lifetime change in protein solution studies. The mCherryTYG fluorescence decays were well fit with two exponential components, a fast decay component $t_{\text{fast}} \sim 0.5 \text{ ns}$ and a slow decay component $t_{\text{slow}} \sim 3 \text{ ns}$ (Table 2). Importantly, the weighted average of the fitted components, which we simply refer to as the “lifetime”, changes from 1.3 ns to 3.0 ns from pH 5.5 to pH 9.0, exhibiting a dynamic range with an unprecedented maximal 1.7 ns change and a pK_a of 6.8 (Figure 22). This dynamic range is 4-fold larger than the 0.4 ns lifetime change exhibited by the RFP pH sensor pHRed²⁸. Notably, the apparent pK_a of 6.8 determined from lifetime measurements differs from the pK_a of 7.4 determined from steady-state brightness measurements (Table 4), which is expected because of the contribution of photon counting as described by Mongeon *et al*⁵⁶. Interestingly, there is a reciprocal change in the amplitudes of the fast and slow components as the pH fluctuates. The slow decay component increases in its relative amplitude as pH increases, with an apparent pK_a of 6.8 in agreement with the pK_a determined from the lifetime response (Figure 23). This trend correlates with acid quenching in which the equilibrium favors a protonated low quantum yield state. Given the promising results of our protein studies, we next determined if mCherryTYG would be effective for lifetime measurements when expressed in live cells.

To this end, we first established that the measurement of mCherryTYG’s lifetime is not affected by total fluorescence intensity, determined by expression levels, or is it distorted by scatter, which is determined by culture density. It is known that strongly scattering media such as thick biological tissues can affect the observed fluorescence lifetime^{57,58}. However, typical bacterial

suspensions should not cause a significant increase in the photon scattering path length relative to the magnitude of the fluorescence lifetime. Therefore, we expect the lifetime to be invariant over a range of liquid culture densities during the log growth phase. To demonstrate this, live cells expressing mCherryTYG were suspended in minimal M63 media at pH 7.5 at optical densities of 0.1 to 0.7, and total fluorescence intensity and fluorescence lifetime were measured under the same respective instrumental settings. Next, we validated that mCherryTYG exhibits its pH-dependent lifetime when expressed in live cells. It is well known that the local environment can alter fluorescent sensor properties due to interactions between proteins, membranes, or other cellular components^{59,60}. However, fluorescent proteins offer a distinct advantage because the protein β -barrel surrounding the interior chromophore protects it from interactions with neighboring biomolecules. To test that pH sensing capability is preserved in live cells, we expressed mCherryTYG in the cytosol of *E. coli* and then measured the pH response in live cell suspensions. As previously established, we used benzoate and methylamine to equalize intracellular and extracellular pH in these experiments^{41,42,61}. Significantly, we found that the mCherryTYG lifetime exhibits a pK_a of 6.8 regardless of its environment, whether as purified protein in dilute solution or expressed in the crowded intracellular environment of a live cell. Interestingly, in live cells there is an increase in dynamic range with a maximum 2 ns change compared to the 1.7 ns change of the purified protein. There is also a small decrease in the absolute lifetime values, with lifetimes ranging from 0.6 ns at pH 5.5 to 2.6 ns at pH 9.0 in live cells. It is possible that non-specific interactions between mCherryTYG and the cell could cause the shift in lifetime values, however mCherry is relatively inert⁴⁸. Furthermore, mCherryTYG is quite pH selective, and it is not affected by differences in monovalent salts, divalent salts, or redox (Figure 20). Alternatively, the overall decrease in lifetime is consistent with the higher index of refraction of cellular environments, which have been measured to cause lifetime shifts of up to ~0.5 ns compared to dilute protein solutions^{62,63}. Notably, in live cells the mCherryTYG fluorescence is only partially quenched at pH 5.5, and fluorescence is still easily detectable for lifetime measurements. Thus, mCherryTYG is a well-behaved pH sensor that retains its pK_a in live cells with an exceedingly large fluorescence lifetime dynamic range.

Interestingly, we noticed that the media composition could greatly affect the basal lifetime of mCherryTYG when expressed in live cells. We suspected that mCherryTYG was reporting differences in metabolic activity, specifically respiration, that contribute to intracellular pH

homeostasis of the aerobic cultures. Thus, the live-cell pH calibration curves were obtained under metabolic inhibition in the absence of exogenous energy sources and in the presence of cyanide to block respiration^{64,65}. This resulted in highly reproducible pH response curves. Importantly, these observations suggested that we could use our sensor measurement approach to quantify pH fluctuations as a readout of metabolic activity in real-time, which we investigated next as a proof-of-concept application.

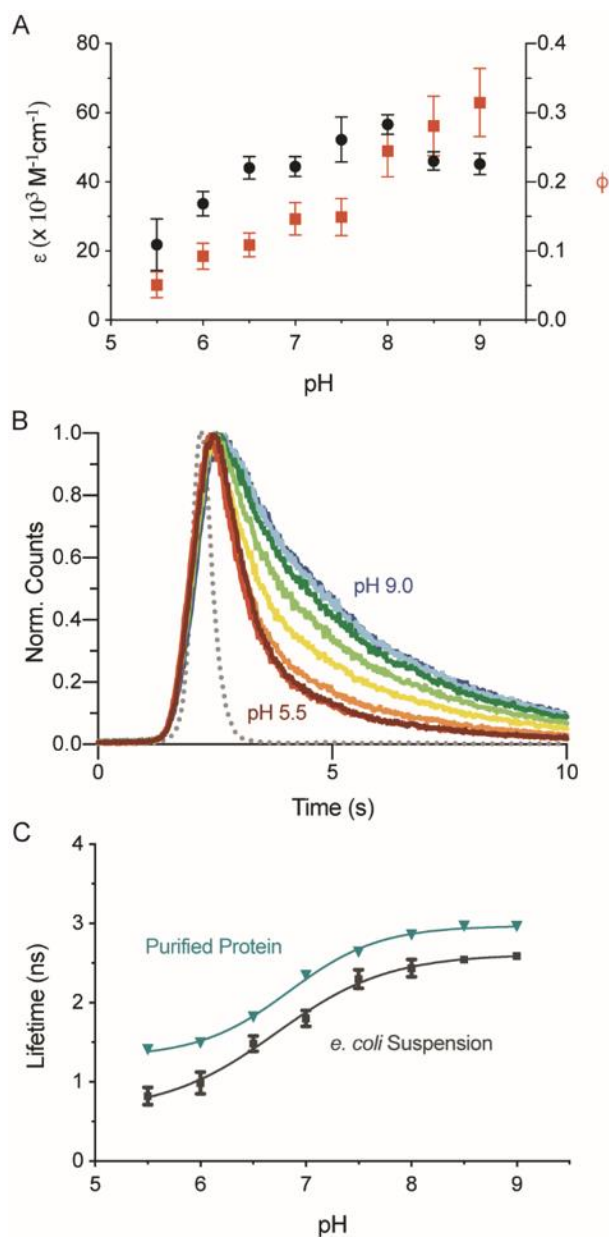


Figure 22 pH-dependent fluorescence lifetime of mCherryTYG
 pH-dependent fluorescence lifetime of mCherryTYG. (A) The extinction coefficient (ϵ) and quantum yield (ϕ) are pH-dependent, but low pH does not completely quench fluorescence (mean \pm std, $n=3$). (B) Representative fluorescence decays from time-resolved measurements of purified protein show that the fluorescence lifetime decreases with decreasing pH (grey dots, IRF). (C) The sensor exhibits a pK_a of 6.8 both in solution and expressed in live *E. coli* (mean \pm std, $n=3$).

Table 3 Fitted fluorescence lifetime decay components for the purified protein pH calibration

pH	τ_{fast} (ns)	Rel.%	τ_{slow} (ns)	Rel.%	τ (ns)	χ^2
5.5	0.56 ± 0.01	57.7 ± 0.8	2.56 ± 0.03	42.3 ± 0.8	1.40 ± 0.01	1.11 ± 0.05
6.0	0.54 ± 0.01	55 ± 1	2.64 ± 0.02	45 ± 1	1.48 ± 0.02	1.17 ± 0.02
6.5	0.55 ± 0.02	44 ± 2	2.81 ± 0.04	56 ± 2	1.81 ± 0.01	1.2 ± 0.1
7.0	0.58 ± 0.01	26.6 ± 0.5	2.98 ± 0.03	73.4 ± 0.5	2.34 ± 0.02	1.11 ± 0.05
7.5	0.68 ± 0.01	17.8 ± 0.1	3.06 ± 0.02	82.2 ± 0.1	2.64 ± 0.02	1.08 ± 0.03
8.0	0.85 ± 0.02	10.6 ± 0.5	3.09 ± 0.03	89.4 ± 0.5	2.86 ± 0.03	1.09 ± 0.05
8.5	1.09 ± 0.09	7.1 ± 0.8	3.11 ± 0.05	92.9 ± 0.8	2.96 ± 0.04	1.11 ± 0.04
9.0	1.26 ± 0.14	8 ± 1	3.10 ± 0.02	92 ± 1	2.96 ± 0.01	1.13 ± 0.04

Table 4 Fitted fluorescence lifetime decay components for the pH-clamped E. coli calibration

pH	τ_{fast} (ns)	Rel.%	τ_{slow} (ns)	Rel.%	τ (ns)	χ^2
5.5	0.29 ± 0.03	67 ± 5	1.87 ± 0.05	33 ± 5	0.8 ± 0.1	1.63 ± 0.06
6.0	0.31 ± 0.04	62 ± 4	2.04 ± 0.04	38 ± 4	1.0 ± 0.1	1.6 ± 0.1
6.5	0.35 ± 0.03	45 ± 3	2.39 ± 0.01	55 ± 3	1.47 ± 0.08	1.36 ± 0.05
7.0	0.38 ± 0.03	35 ± 3	2.53 ± 0.02	65 ± 3	1.79 ± 0.08	1.26 ± 0.09
7.5	0.46 ± 0.09	18 ± 3	2.67 ± 0.03	82 ± 3	2.3 ± 0.1	1.17 ± 0.08
8.0	0.5 ± 0.1	13 ± 2	2.69 ± 0.05	87 ± 2	2.4 ± 0.1	1.14 ± 0.04
8.5	0.6 ± 0.1	9 ± 2	2.73 ± 0.03	91 ± 2	2.54 ± 0.06	1.1 ± 0.1
9.0	0.7 ± 0.2	8 ± 2	2.75 ± 0.03	92 ± 2	2.58 ± 0.04	1.14 ± 0.01

Table 5 Steady-state properties of fluorescent proteins.

RFP	Ex. (nm)	Em. (nm)	ϵ ($M^{-1} \cdot cm^{-1}$)	ϕ	pKa ⁴
mCherry-TYG ^{1,2}	558	582	20,000	0.05	7.4 ¹ ; 7.8 ²
(pH 5.5)	543	562	55,000	0.31	
(pH 9.0)					
mOrange ³	548	562	71,000	0.69	6.5
mCherry ³	587	610	72,000	0.22	4.5

¹ This study; ² Shen *et al.*; ³ Shaner *et al.*⁵³; ⁴ Steady-state pK_a calculated from pH-dependent change in fluorescence intensity brightness.

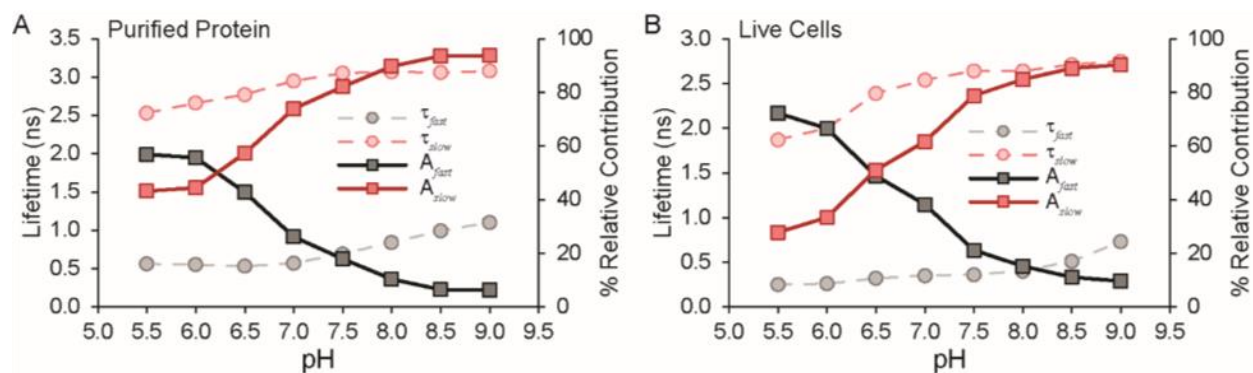


Figure 23 Fluorescence lifetime decay time constants

Plots of the time constants obtained by reconvolution fitting for sample-matched IRFs also reported in Tables S1 and S2 for pH calibration curves obtained from (A) purified mCherryTYG protein or (B) mCherryTYG expressed in live *E. coli* with benzoate and methylamine pH clamping. The pH dose response of the relative amplitude of the slow component exhibits (A) a pK_a of 6.81 ± 0.08 for purified protein and (B) a pK_a of 6.7 ± 0.1 for live cells.

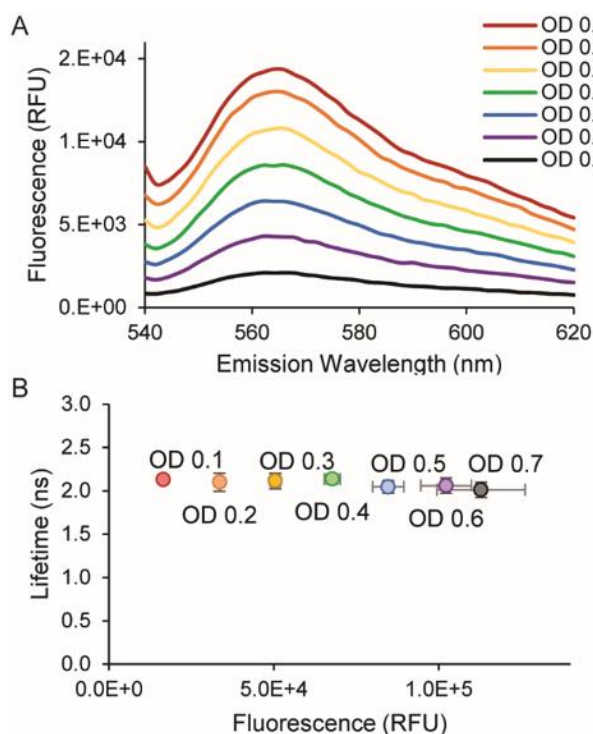


Figure 24 Fluorescence lifetime is independent of scatter and total intensity in live cell suspensions (A) mCherryTYG fluorescence was detectable live-cell suspensions at an OD of 0.1 to 0.7. (B) The lifetime does not depend on the total fluorescence intensity or scatter (mean \pm std, $n = 3$; no differences by ANOVA with Tukey's posthoc, $p > 0.4$ for all comparisons).

3.4.1 Live-Cell Lifetime Spectroscopy

Building on our sensor characterization, we set out to demonstrate that (1) mCherryTYG is effective for measuring physiology, (2) time-resolved spectroscopy on live-cell suspensions provides a quantitative approach to real-time continuous assays, and (3) mCherryTYG enables simultaneous multicolor lifetime measurements.

With regard to our first two objectives, we carried out single-color fluorescence lifetime measurements with mCherryTYG to quantify how respiration acutely contributes to pH regulation, which had not been directly determined in this manner previously. Under aerobic conditions, *E. coli* use a variety of pH homeostasis mechanisms to maintain intracellular pH in range of 7 - 8, even in the face of extreme acid or base stress^{4,13-16}. Evolved acid stress resistance mechanisms include potassium-dependent proton extrusion, amino acid decarboxylation, as well as the upregulation of many genes including respiratory complex proteins^{66,67}. Seminal work using radioactive tracer distribution demonstrated that respiration contributes to the substantial difference between intracellular and extracellular pH under aerobic conditions⁶⁴, and live-cell nuclear magnetic resonance (NMR) studies showed that pH homeostasis effectively resists transient pH changes under acid and base challenge⁶⁸. Under anaerobic conditions, live-cell NMR also established that ATP can be used to power proton efflux in the absence of respiration⁶⁵. Here, we present a novel approach using mCherryTYG live-cell lifetime spectroscopy to demonstrate that respiration also contributes to acute pH regulation under aerobic conditions.

We first continuously measured the lifetime of mCherryTYG in live *E. coli* suspensions subjected to mild acid stress. Live cells were equilibrated in minimal M63 media buffered at pH 6 containing potassium but no amino acids and no exogenous energy sources⁶¹. As expected, at baseline in the absence of fuel the cytosol was slightly acidic at pH = 6.5 - 7.0 (Figure 25, 26). Upon addition of glucose, there was an immediate alkalinization of the cytosol with the intracellular pH approaching pH 8. The subsequent addition of cyanide to block respiration caused a pH reversal and acidification of the cytosol. Control cell suspensions expressing either no fluorescent protein or the pH-insensitive wildtype mCherry did not exhibit lifetime changes (Figure 26). To demonstrate that mCherryTYG was well-calibrated, we added benzoate and methylamine at the end of the experiment to equalize the intracellular and extracellular pH⁶¹. Notably, mCherryTYG reported a pH of 6.5 which was consistent with the alkalinization of the M63 media caused by the addition of the potassium cyanide basic salt, as measured using pH

electrodes for orthogonal validation. Of note, cyanide addition did not cause a pH change in the vehicle control without glucose addition (Figure 25, 26), indicating minimal respiratory proton pumping activity in the absence of a fuel. However, in both the glucose and no fuel control conditions after cyanide treatment, the cytosol remained alkaline with respect to the extracellular media, and benzoate and methylamine caused acidification after loss of the intracellular-extracellular pH gradient. Hence, the live cells also retained respiration-independent homeostatic mechanisms that persist in the absence of fuel. We observed a similar phenotype when *E. coli* were subjected to the same protocol using M63 media at pH 7 (Figure 25, 26). Interestingly, with mild alkaline stress using M63 media at pH 8, the addition of glucose still caused a trend towards an alkalization, though it was not statistically significant across independent cultures (Figure 26). Thus, our measurements demonstrate that *E. coli* are able to resist mild acid stress and maintain a near neutral cytosol on acute timescales even in the absence of an external energy source. Furthermore, we hypothesize that the cyanide-inhibited alkalization upon glucose addition reflects the fuel and respiration-dependent pumping of protons out of the cell to support oxidative phosphorylation and ATP synthesis.

To test that our experimental conditions do in fact result in intracellular ATP level changes, we utilized the ATeam1.03YEMK (abbreviated ATeam) fluorescent sensor which is well-tuned for bacterial ATP levels^{69,70}. The sensor employs Förster-type resonance energy transfer (FRET) between a cyan fluorescent protein (CFP) and yellow fluorescent protein (YFP) donor-acceptor pair in which ATP-binding causes an increase in FRET⁷⁰. The steady-state fluorescence emission spectra of live cell suspensions expressing ATeam were measured in the absence of fuel, after glucose addition, and after cyanide addition (Figure 27). The emission spectra showed significant increases in FRET from the resulting increase in intracellular ATP after glucose addition, which is reversed with the subsequent addition of cyanide. Thus, our time-resolved fluorescence measurements of mCherryTYG and steady-state fluorescence measurements of ATeam are consistent with fuel and respiration-dependent ATP synthesis.

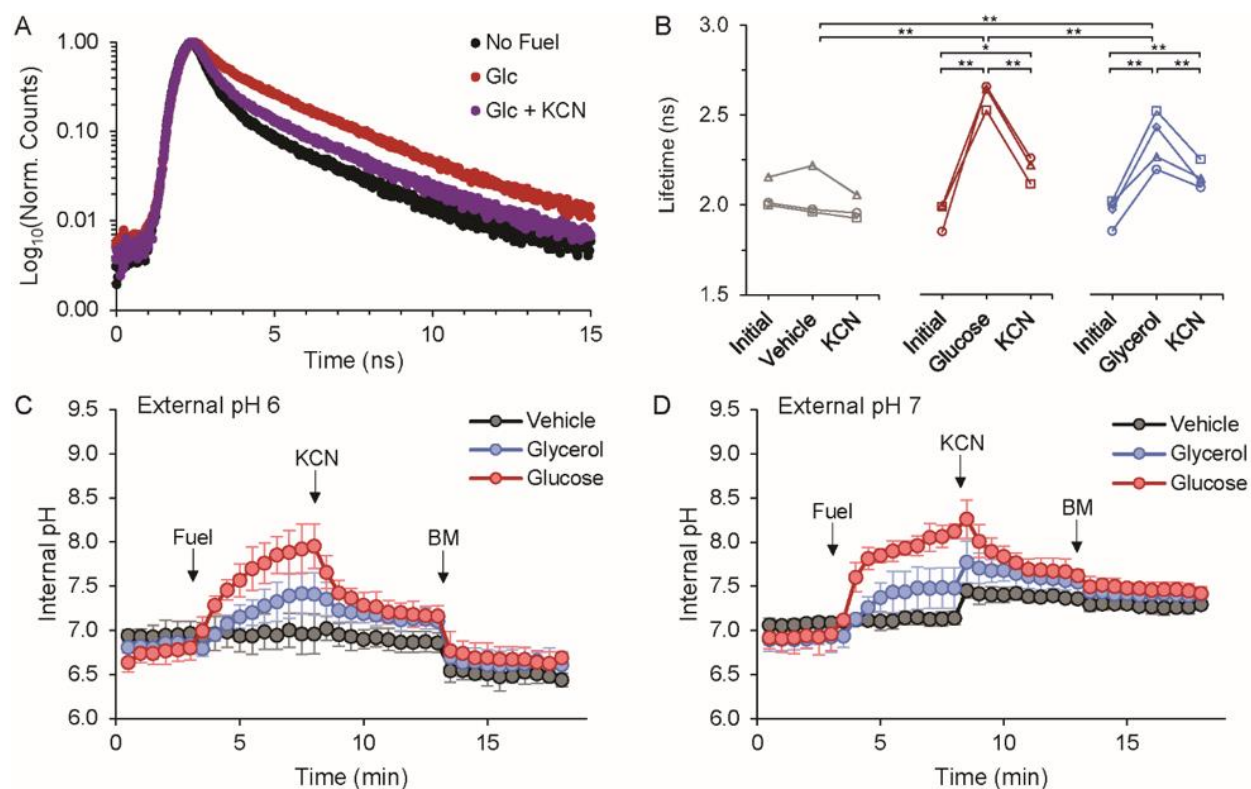


Figure 25 Fuel and respiration-dependent pH homeostasis

Time-resolved measurements of live *E. coli* expressing mCherryTYG in M63 media lacking glucose and amino acids, buffered at (A-C) pH 6 or (D) pH 7. (A) Example fluorescence lifetime decays. (B) Addition of Fuel, glucose (n=3) or glycerol (n=4), causes an increase in cytosolic pH reported by the mCherryTYG lifetime, but no-fuel Vehicle addition (n=3) does not. Cyanide (KCN) blocks respiration and causes acidification after loss of electron transport mediated proton pumping. Lines connect data for independent cultures. (**p<0.05, *p<0.1, two-tail t-test, paired within fuel condition, unpaired between fuels). (C-D) Time-dependent changes in intracellular pH for cells in M63 media at (C) pH 6 and (D) pH 7 (n=3 each). Data are the mean \pm 95% confidence interval (CI) for independent cultures. Benzoate and methylamine (BM) equalize the intracellular and extracellular pH.

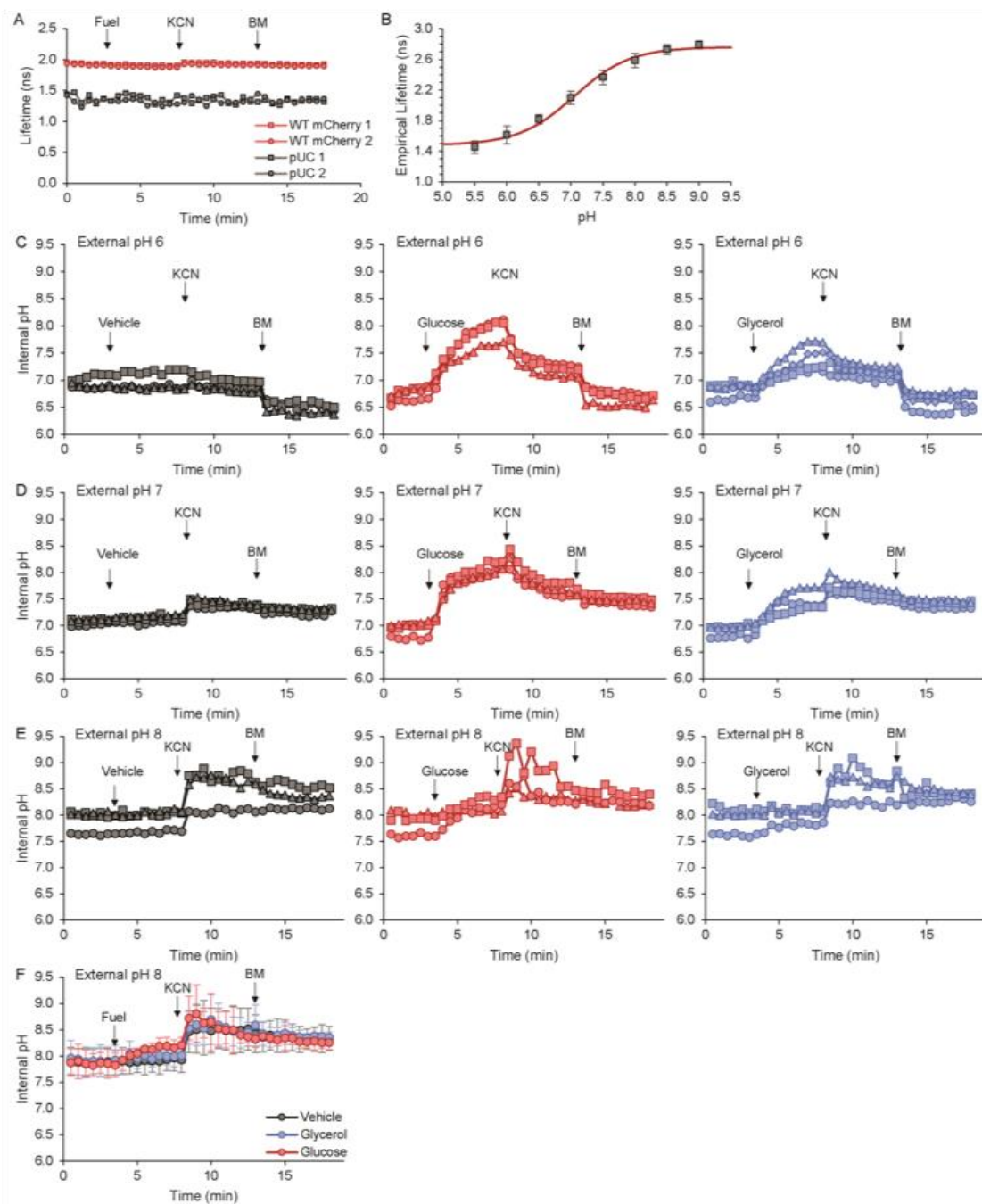


Figure 26 Live-cell time-resolved spectroscopy on *E. coli* suspensions

(A) Controls using pUC cells expressing no fluorescent protein and cells expressing pH-insensitive wildtype mCherry show no change in lifetime with fuel or cyanide addition in M63 media at pH 6. (B) Calibration curve for the empirical tail mean lifetime for continuous live-cell assays. (C-E) Each trace is the pH response for an independent culture of mCherryTYG expressing cells in M63 media at (C) pH 6, (D) pH 7, and (E) pH 8. (F) The average response at pH 8 (mean \pm 95% CI) trended towards alkalization only with the glucose addition.

These results show that mCherryTYG is very effective at reporting pH changes linked to respiratory activity and central energy metabolism, and therefore we next tested whether we could quantify differences in fuel source. Previous studies have demonstrated that glycerol can support bacterial respiration, but it is a less efficient energy source that provides half the equivalents of ATP production compared to glucose⁷¹⁻⁷³. We therefore hypothesized that using glycerol as fuel would result in a diminished respiration-dependent alkalization compared to glucose. Employing the same experimental protocol, we measured the mCherryTYG lifetime in live cells and found that the addition of 0.8% glycerol⁴² caused an alkalization of the cytosol qualitatively similar to the response during glucose addition (Figure 25). However, the approximately equimolar addition of glycerol caused a stoichiometric attenuation in the pH increase compared to glucose addition (Figure 25). Furthermore, steady-state fluorescence emission spectra of cells expressing ATeam show that the increase in ATP is significantly lower for glycerol compared to glucose treatment (Figure 27). Cyanide treatment did cause a decrease in ATP levels, indicating that glycerol supports ATP production via respiratory activity. Notably, control experiments demonstrate that the pH sensitivity of the ATeam sensor⁷⁰ does not account for the observed ratio changes, and ATeam faithfully reports ATP levels under these conditions (Figure 28). Thus, the use of glycerol compared to glucose as an energy source results in a quantitative decrease in ATP production that correlates well with a decrease in respiration-dependent proton efflux.

Using our sensor approach, we have now measured to what extent respiration can contribute to the regulation of intracellular pH on acute time scales under aerobic conditions. Overall, these results demonstrate that continuous real-time measurements of mCherryTYG lifetime in live-cell suspensions can provide new and quantitative insights into the metabolic regulation of pH. In these experiments, we validated the effects on energy metabolism using steady-state fluorescence measurements of the ATeam sensor. However, mCherryTYG is a significant addition to the toolbox of genetically-encoded pH sensors, not only because it provides a lifetime-based readout, but because it is red fluorescent, making it spectrally compatible with other sensors. We demonstrate this advantage next with simultaneous multicolor spectroscopy.

3.5 Multicolor Live-Cell Lifetime Spectroscopy.

To address the third objective of our proof-of-concept studies, we showed that mCherryTYG is spectrally compatible for simultaneous two-color lifetime measurements, facilitating direct

correlative analysis of more than one physiological parameter within the same specimen. Our steady-state spectroscopy results demonstrated that the ATeam detects changes in ATP levels related to the pH fluctuations reported by mCherryTYG. Because ATeam is a FRET-based sensor, the CFP donor lifetime should also change with respect to ATP levels. The ATP-bound, high FRET state should have a decreased CFP donor lifetime, and therefore an increase in ATP will cause a decrease in the ATeam lifetime. Therefore, it should be possible to measure the lifetimes of ATeam and mCherryTYG simultaneously. To test this, we studied *E. coli* cultures with a mixture of cells expressing mCherryTYG and cells expressing ATeam.

As expected, in M63 media at pH 6, the addition of glucose causes an increase in the mCherryTYG lifetime because of cytosolic alkalinization (Figure 29, 31). Importantly, glucose addition also causes a concurrent decrease in the ATeam lifetime, reporting an increase in ATP within the same sample (Figure 29, 31). The subsequent addition of cyanide blocks respiration causing re-acidification of the cytosol, and there is a correlated increase in the ATeam lifetime that reports a decrease in intracellular ATP levels with metabolic inhibition. Hence, lifetime changes of both mCherryTYG and ATeam can be measured simultaneously to directly correlate changes in respiratory proton pumping and ATP synthesis.

We were then curious how different nutrient additives found in bacterial medias might affect metabolism. For example, casamino acids are typically used to provide amino acid supplementation and support nitrogen metabolism in microbial cultures. Interestingly, we found the addition of 0.2% casamino acids¹⁸ in either the absence or presence of glucose caused a similar increase in the mCherryTYG lifetime that is reversed by cyanide treatment (Figure 29, 31), showing that casamino acids can support respiratory proton pumping. However, the ATeam lifetime also increased, indicating an acute consumption of ATP that was further exacerbated by cyanide addition (Figure 29, 31). We hypothesized It is possible that the consumption of ATP results from saturation of amino acid influx pathways via energy-dependent ABC transporters as well as flux through previously depleted anapleurotic and biosynthetic pathways. However, casamino acids are not a chemically-defined mixture, and in the future beyond this proof-of-concept, it will be interesting to tease apart the microbial metabolism responsible for these observations.

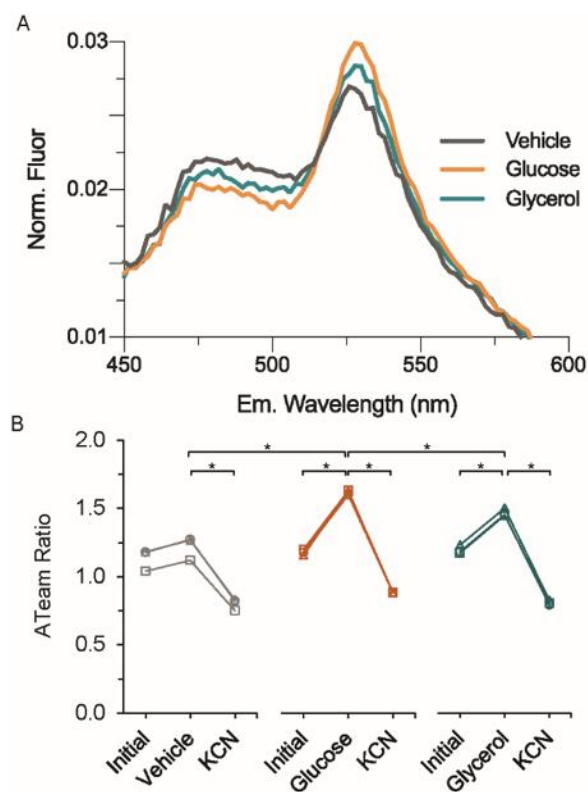


Figure 27 Acute changes in respiration regulates intracellular ATP

(A) Addition of glucose or glycerol increases intracellular ATP levels, reported by increased FRET-to-CFP peak ratios in the steady-state fluorescence emission spectra of live *E. coli* expressing ATeam1.03YEMK. (B) Glucose causes a greater increase in ATP compared to glycerol, and KCN decreases ATP. Lines connect data for independent cultures. (* $p < 0.01$, 2-tailed t-test, $n = 3$).

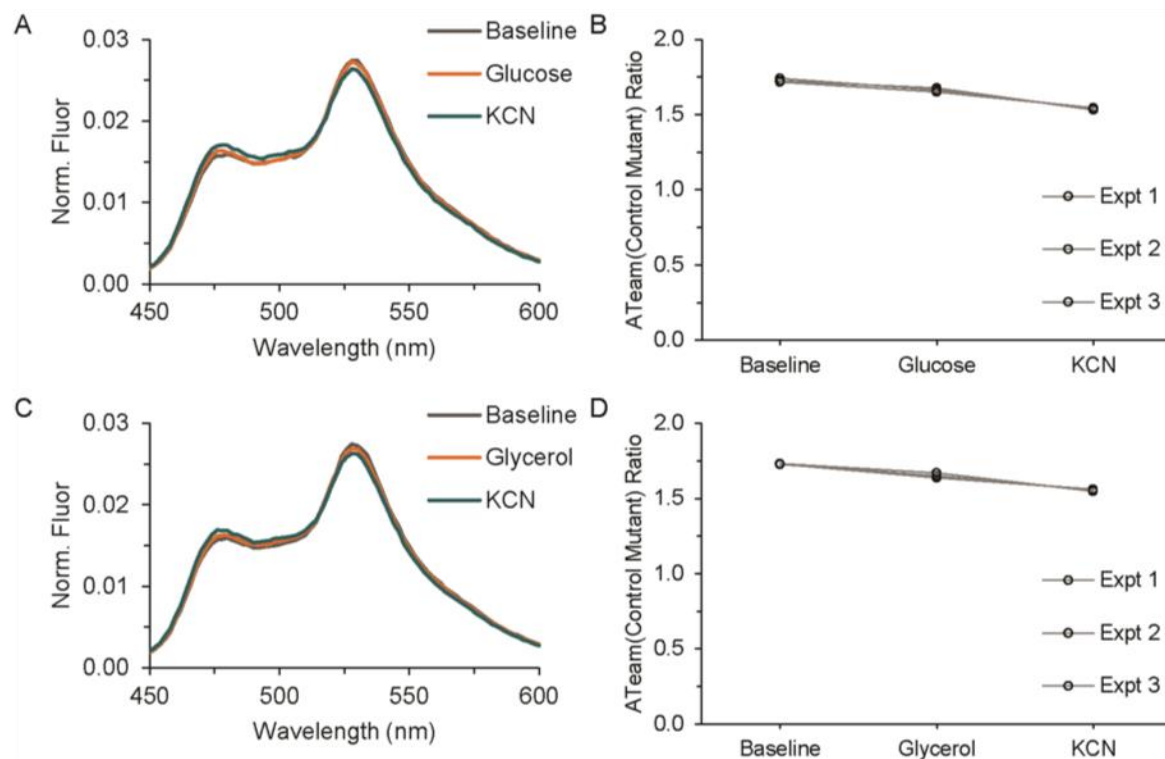


Figure 28 Non-binding ATeamYEMK mutant controls

The ATeam sensor is known to be pH sensitive, but between pH 7.0 to 8.0 the ATeam sensor is far more sensitive to changes in ATP compared to pH (Imamura *et al.* 2009 PNAS). To validate that the ATeam sensor reports true changes in ATP and that the spectral changes are not an artifact of a pH change, we used live cells expressing the ATeam1.03YEMK(R103A) mutant that does not bind ATP. Neither glucose (A-B) nor glycerol (C-D) fuel addition causes a change in the steady-state FRET/CFP emission ratio, and there is only a minor decrease in the ratio after the addition of KCN. The ratios values are: (A-B) baseline, 1.73 ± 0.01 ; glucose, 1.66 ± 0.01 ; KCN, 1.54 ± 0.01 ; (C-D) baseline, 1.73 ± 0.01 ; glycerol, 1.65 ± 0.02 ; KCN, 1.56 ± 0.01 ; mean \pm 95% CI. Thus, control experiments using live cells expressing the non-binding mutant demonstrate that the pH sensitivity of the ATeam sensor does not account for the large ratio changes observed and reported in Figure 5.

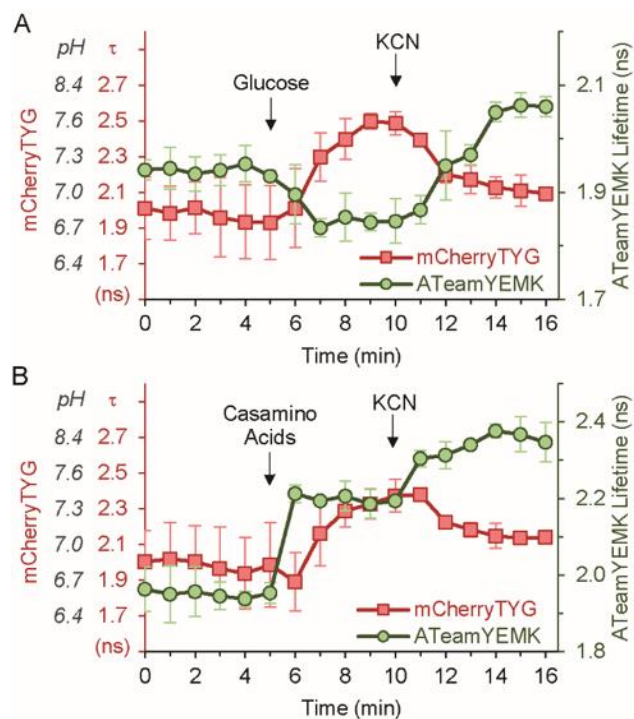


Figure 29 Simultaneous two-color live-cell lifetime measurements directly correlate intracellular pH and ATP levels

Live *E. coli* expressing mCherryTYG (red) and ATeam (green) were mixed in M63 media at pH 6. (A) Glucose addition causes an increase in pH and the mCherryTYG lifetime (τ). It also causes an increase in ATP and thus a decrease in ATeam CFP donor lifetime (green). Block of respiration with cyanide causes a reversal. (B) Casamino acids support respiratory alkalization reported by the increase in the mCherryTYG lifetime, but the increase in ATeam lifetime indicates acute ATP consumption (mean \pm 95% CI, n=3).

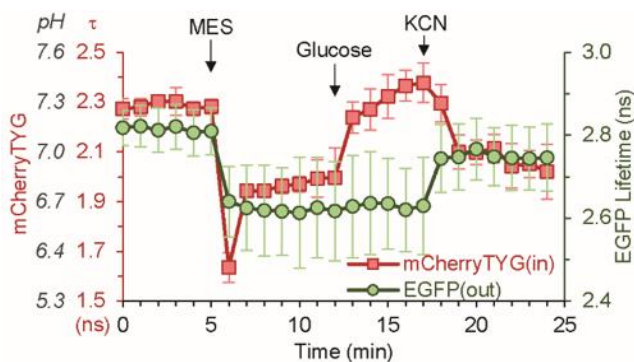


Figure 30 Simultaneous measurement of the extracellular and intracellular pH

Live *E. coli* expressing mCherryTYG (red) were suspended in M63 media at pH 8 containing purified EGFP (green). The media was first acidified to pH 6 with MES, followed by the addition of glucose and KCN (mean \pm 95% CI, n=3).

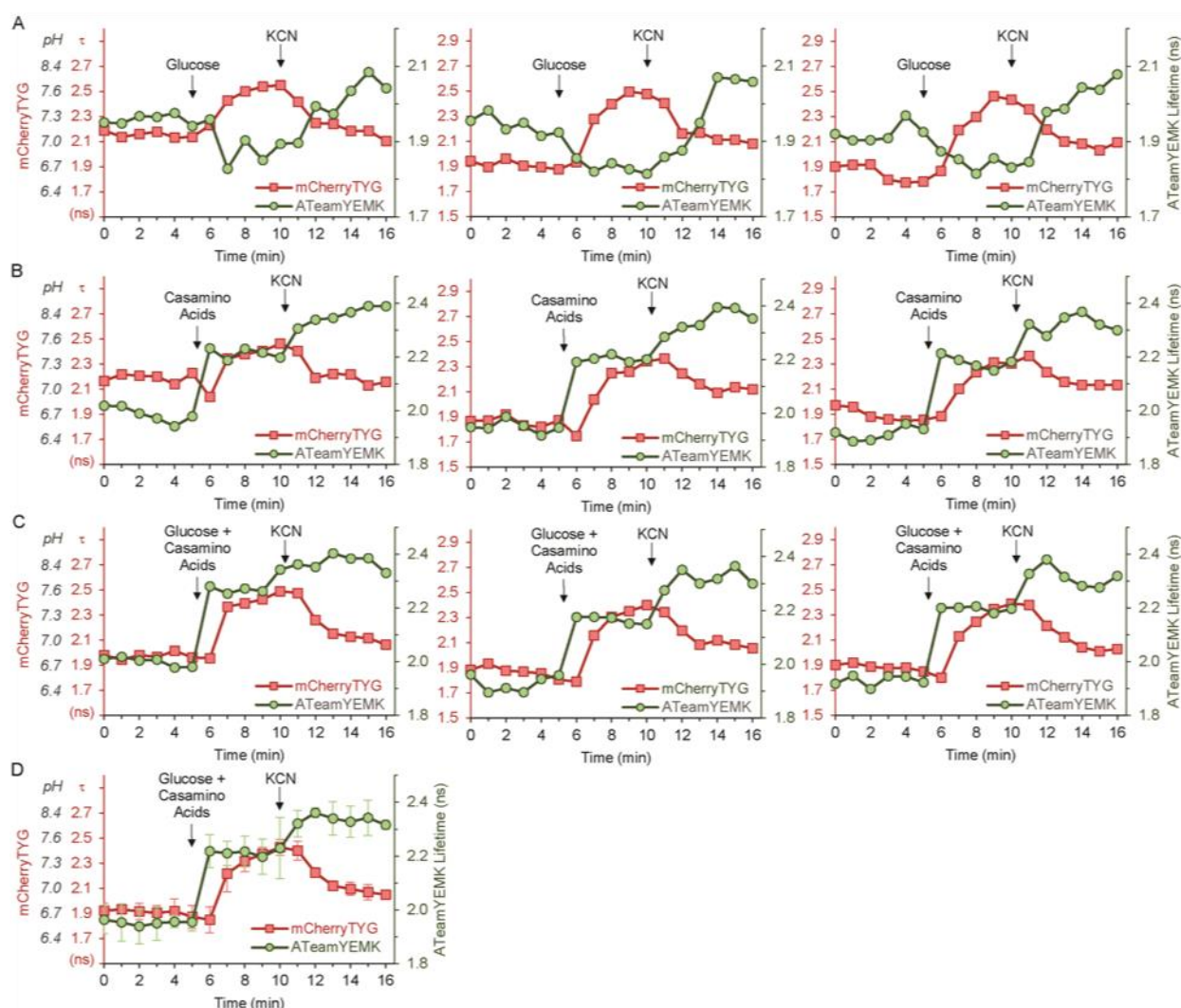


Figure 31 Simultaneous two-color live-cell lifetime measurements directly correlate intracellular pH and ATP levels

Each plot shows the correlated mCherryTYG (red) and ATeamYEMK (green) individual time-course data for independent experiments testing the effects of (A) glucose addition, which is presented as averaged data in Figure 6A, and (B) glycerol addition, which is presented as averaged data in Figure 6B. (C-D) The addition of casamino acids together with glucose supports respiration and causes intracellular alkalinization reported by the increase in the mCherryTYG lifetime. However, casamino acid transport and metabolism consumes ATP and causes a decrease in intracellular ATP levels reported by the increase in ATeam donor lifetime, even in the presence of glucose. Individual time-course data for independent experiments (C) and averaged data (D) are presented.

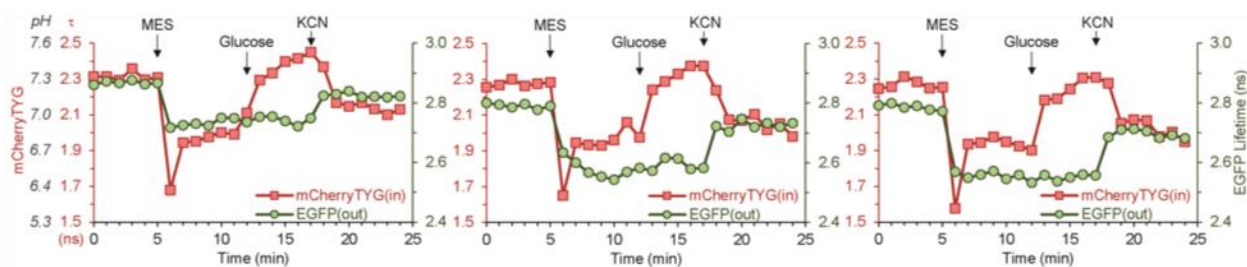


Figure 32 Simultaneous two-color live-cell lifetime measurements directly correlate intracellular pH and extracellular pH

Each plot shows the correlated intracellular mCherryTYG (red) and extracellular EGFP (green) individual time-course data for independent experiments that are presented as averaged data in Figure 7.

Ultimately, respiration supports the generation of a pH gradient that contributes to the proton motive force driving ATP synthesis. Therefore we used mCherryTYG and EGFP to measure different changes in intracellular and extracellular pH simultaneously. EGFP is pH sensitive, and acidification causes a decrease in its lifetime^{37,74,75}. Cells expressing mCherryTYG were equilibrated in M63 media modified to contain 5 mM MOPS, providing weak buffering capacity at pH 8. Purified EGFP was included in the media, with no amino acids or fuel present. Measuring mCherryTYG and EGFP lifetimes simultaneously, we first added 50 mM MES to acidify the extracellular media to pH 6 (Figure 30, 32). Both green and red fluorescence lifetimes decreased, reflecting the acidification of both the media and cytosol, respectively. Interestingly, the mCherryTYG lifetime reported a reproducible acid transient indicative of fast regulation that, taken together with our previous observations, supports the persistence of fuel and respiration-independent homeostatic mechanisms. Such mechanisms could rely on decarboxylase acid resistance systems, given the short starvation likely did not completely deplete residual glutamate and arginine. Upon the addition of glucose, however, the extracellular pH remained constant as reported by EGFP, while the intracellular pH increased as reported by mCherryTYG. Furthermore, the addition of the cyanide basic salt caused an alkalization of the extracellular pH as expected, and also expected was the blockade of respiration causing an acidification of the cytosol. These results clearly demonstrate that mCherryTYG and EGFP lifetimes can be measured in live-cell suspensions to simultaneously quantify intracellular and extracellular pH, providing quantitative insight into respiratory contribution to the generation of the proton gradient.

3.6 Conclusions

Understanding pH regulation is fundamentally important to deconvoluting the complex physiology of species ranging from single-cell prokaryotes to mammals. In this report, we were able to study metabolically-driven pH changes in live *E. coli* using mCherryTYG, which we demonstrate is a highly effective genetically-encoded red fluorescent sensor, that quantitatively reports pH via its fluorescence lifetime. Using this sensor, we make novel measurements of the acute contributions of respiration to intracellular pH homeostasis in support of ATP generation. Our results clearly demonstrate that lifetime spectroscopy of mCherryTYG could be used to quantify the contributions of different homeostatic mechanisms under different nutrient and growth conditions. Furthermore, the mCherryTYG pH sensor stands out uniquely as a red fluorescent lifetime pH sensor. In comparison to the only other RFP lifetime pH sensor characterized in live cells, the 2.0 ns dynamic range of mCherryTYG is a vast improvement over the 0.4 ns dynamic range of pHRed²⁸. In fact, the 2.0 ns dynamic range of mCherryTYG is extraordinarily large for any lifetime sensor, including: EGFP that exhibits a 0.8 ns pH-dependent change^{37,74,75}; intramolecular FRET sensors such as the AKAR protein kinase A^{76,77}, IDOCKS protein kinase C⁷⁸, and epac cAMP⁷⁹ sensors that exhibit 0.2 ns, 0.3 ns, and 1.0 ns changes, respectively; and intermolecular FRET small GTPase activity sensors that exhibit 0.3 ns changes⁸⁰. Additionally, we found that neither the pK_a or dynamic range of mCherryTYG was strongly perturbed by expression in live cells, unlike many other sensors that experience significant changes in analyte sensitivity as well as attenuated dynamic ranges^{81,82}. Thus, in general our methodology fills an important technology gap that provides molecular specificity in the live-cell context without the high barriers of FLIM instrumentation.

3.7 References

1. Berezin, M. Y. & Achilefu, S. Fluorescence Lifetime Measurements and Biological Imaging. *Chem. Rev.* (2010). doi:10.1021/cr900343z
2. Hum, J. M., Siegel, A. P., Pavalko, F. M. & Day, R. N. Monitoring biosensor activity in living cells with fluorescence lifetime imaging microscopy. *Int. J. Mol. Sci.* **13**, 14385–14400 (2012).
3. Gohil, V. M. *et al.* Nutrient-sensitized screening for drugs that shift energy metabolism from mitochondrial respiration to glycolysis. *Nat. Biotechnol.* **28**, 249–255 (2010).

4. Krulwich, T. A., Sachs, G. & Padan, E. Molecular aspects of bacterial pH sensing and homeostasis. *Nat. Rev. Microbiol.* **9**, 330–343 (2011).
5. Farha, M. A., French, S., Stokes, J. M. & Brown, E. D. Bicarbonate Alters Bacterial Susceptibility to Antibiotics by Targeting the Proton Motive Force. *ACS Infect. Dis.* **4**, 382–390 (2018).
6. Zhao, N. *et al.* Target-Based Screen Against a Periplasmic Serine Protease That Regulates Intrabacterial pH Homeostasis in *Mycobacterium tuberculosis*. *ACS Chem. Biol.* **10**, 364–371 (2015).
7. Chan, L. C. Z., Khalili Moghaddam, G., Wang, Z. & Lowe, C. R. Miniaturized pH Holographic Sensors for the Monitoring of *Lactobacillus casei* Shirota Growth in a Microfluidic Chip. *ACS Sensors* **4**, 456–463 (2019).
8. Luo, X. *et al.* Highly Sensitive Hill-Type Small-Molecule pH Probe That Recognizes the Reversed pH Gradient of Cancer Cells. *Anal. Chem.* **90**, 5803–5809 (2018).
9. Paredes, J. M. *et al.* Synchronous Bioimaging of Intracellular pH and Chloride Based on LSS Fluorescent Protein. *ACS Chem. Biol.* **11**, 1652–1660 (2016).
10. Kinchen, J. M. & Ravichandran, K. S. Phagosome maturation: going through the acid test. *Nat. Rev. Mol. Cell Biol.* **9**, 781–795 (2008).
11. Gao, W., Chan, J. M. & Farokhzad, O. C. pH-Responsive Nanoparticles for Drug Delivery. *Mol. Pharm.* **7**, 1913–1920 (2010).
12. Su, H., Xu, G., Chen, H. & Xu, Y. Enriching Duckweed As an Energy Crop for Producing Biobutanol Using Enzyme Hydrolysis Pretreatments and Strengthening Fermentation Process Using pH-stat. *ACS Sustain. Chem. Eng.* **3**, 2002–2011 (2015).
13. Padan, E., Bibi, E., Ito, M. & Krulwich, T. A. Alkaline pH homeostasis in bacteria: New insights. *Biochim. Biophys. Acta - Biomembr.* **1717**, 67–88 (2005).
14. Lund, P., Tramonti, A. & De Biase, D. Coping with low pH: molecular strategies in neutrophilic bacteria. *FEMS Microbiol. Rev.* **38**, 1091–1125 (2014).
15. Foster, J. W. *Escherichia coli* acid resistance: tales of an amateur acidophile. *Nat. Rev. Microbiol.* **2**, 898–907 (2004).
16. Slonczewski, J. L., Fujisawa, M., Dopson, M. & Krulwich, T. A. Cytoplasmic pH Measurement and Homeostasis in Bacteria and Archaea. in *Advances in microbial physiology* **55**, 1–317 (2009).
17. Meylan, S. *et al.* Carbon Sources Tune Antibiotic Susceptibility in *Pseudomonas aeruginosa* via Tricarboxylic Acid Cycle Control. *Cell Chem. Biol.* **24**, 195–206 (2017).

18. Lobritz, M. A. *et al.* Antibiotic efficacy is linked to bacterial cellular respiration. *Proc. Natl. Acad. Sci.* **112**, 8173–8180 (2015).
19. Wencel, D., Abel, T. & McDonagh, C. Optical Chemical pH Sensors. *Anal. Chem.* **86**, 15–29 (2014).
20. Han, J. & Burgess, K. Fluorescent Indicators for Intracellular pH - Chemical Reviews (ACS Publications). *Chem. Rev.* **110**, 2709–2728 (2010).
21. Greenwald, E. C., Mehta, S. & Zhang, J. Genetically Encoded Fluorescent Biosensors Illuminate the Spatiotemporal Regulation of Signaling Networks. *Chem. Rev.* **118**, 11707–11794 (2018).
22. Szmecinski, H. & Lakowicz, J. R. Optical measurements of pH using fluorescence lifetimes and phase-modulation fluorometry. *Anal. Chem.* **65**, 1668–1674 (1993).
23. Miesenböck, G., De Angelis, D. A. & Rothman, J. E. Visualizing secretion and synaptic transmission with pH-sensitive green fluorescent proteins. *Nature* **394**, 192–195 (1998).
24. Poburko, D., Santo-Domingo, J. & Demaurex, N. Dynamic regulation of the mitochondrial proton gradient during cytosolic calcium elevations. *J. Biol. Chem.* **286**, 11672–84 (2011).
25. Johnson, D. E. *et al.* Red Fluorescent Protein pH Biosensor to Detect Concentrative Nucleoside Transport. *J. Biol. Chem.* **284**, 20499–20511 (2009).
26. Li, Y. & Tsien, R. W. pHTomato, a red, genetically encoded indicator that enables multiplex interrogation of synaptic activity. *Nat. Neurosci.* **15**, 1047–1053 (2012).
27. Shen, Y., Rosendale, M., Campbell, R. E. & Perrais, D. pHuji, a pH-sensitive red fluorescent protein for imaging of exo- and endocytosis. *J. Cell Biol.* **207**, 419–432 (2014).
28. Tantama, M., Hung, Y. P. & Yellen, G. Imaging Intracellular pH in Live Cells with a Genetically Encoded Red Fluorescent Protein Sensor. *J. Am. Chem. Soc.* **133**, 10034–10037 (2011).
29. Gandasi, N. R. *et al.* Survey of Red Fluorescence Proteins as Markers for Secretory Granule Exocytosis. *PLoS One* **10**, e0127801 (2015).
30. Sankaranarayanan, S., De Angelis, D., Rothman, J. E. & Ryan, T. A. The Use of pHluorins for Optical Measurements of Presynaptic Activity. *Biophys. J.* **79**, 2199–2208 (2000).
31. Boens, N. *et al.* Fluorescence Lifetime Standards for Time and Frequency Domain Fluorescence Spectroscopy. *Anal. Chem.* **79**, 2137–2149 (2007).
32. Lakowicz, J. R., Szmecinski, H., Nowaczyk, K. & Johnson, M. L. Fluorescence lifetime imaging of free and protein-bound NADH. *Proc. Natl. Acad. Sci. U. S. A.* **89**, 1271–5 (1992).

33. Wang, X. F., Uchida, T. & Minami, S. A Fluorescence Lifetime Distribution Measurement System Based on Phase-Resolved Detection Using an Image Dissector Tube. *Appl. Spectrosc.* **43**, 840–845 (1989).
34. Li, L. *et al.* Imaging the Redox States of Live Cells with the Time-Resolved Fluorescence of Genetically Encoded Biosensors. *Anal. Chem.* [acs.analchem.8b04292](https://doi.org/10.1021/acs.analchem.8b04292) (2019). doi:10.1021/acs.analchem.8b04292
35. Ge, L. & Tian, Y. Fluorescence Lifetime Imaging of p-tau Protein in Single Neuron with a Highly Selective Fluorescent Probe. *Anal. Chem.* [acs.analchem.8b03992](https://doi.org/10.1021/acs.analchem.8b03992) (2019). doi:10.1021/acs.analchem.8b03992
36. Kneen, M., Farinas, J., Li, Y. & Verkman, A. S. Green Fluorescent Protein as a Noninvasive Intracellular pH Indicator. *Biophys. J.* **74**, 1591–1599 (1998).
37. Nakabayashi, T., Wang, H.-P., Kinjo, M. & Ohta, N. Application of fluorescence lifetime imaging of enhanced green fluorescent protein to intracellular pH measurements. *Photochem. Photobiol. Sci.* **7**, 668 (2008).
38. Esposito, A., Gralle, M., Dani, M. A. C., Lange, D. & Wouters, F. S. pHlameleons: A Family of FRET-Based Protein Sensors for Quantitative pH Imaging †. *Biochemistry* **47**, 13115–13126 (2008).
39. Dean, K. M. *et al.* High-Speed Multiparameter Photophysical Analyses of Fluorophore Libraries. *Anal. Chem.* **87**, 5026–5030 (2015).
40. Houston, J. P. *et al.* Overview of Fluorescence Lifetime Measurements in Flow Cytometry. in *Methods in molecular biology (Clifton, N.J.)* **1678**, 421–446 (2018).
41. Kitko, R. D., Wilks, J. C., Garduque, G. M. & Slonczewski, J. L. Osmolytes Contribute to pH Homeostasis of Escherichia coli. *PLoS One* **5**, e10078 (2010).
42. Wilks, J. C. & Slonczewski, J. L. pH of the cytoplasm and periplasm of Escherichia coli: rapid measurement by green fluorescent protein fluorimetry. *J. Bacteriol.* **189**, 5601–7 (2007).
43. Kitko, R. D. *et al.* Cytoplasmic Acidification and the Benzoate Transcriptome in Bacillus subtilis. *PLoS One* **4**, e8255 (2009).
44. Isom, D. G. *et al.* Coordinated regulation of intracellular pH by two glucose-sensing pathways in yeast. *J. Biol. Chem.* **293**, 2318–2329 (2018).
45. Aresta-Branco, F. *et al.* Gel Domains in the Plasma Membrane of *Saccharomyces cerevisiae*. *J. Biol. Chem.* **286**, 5043–5054 (2011).
46. Kirkpatrick, N. D. *et al.* Endogenous Fluorescence Spectroscopy of Cell Suspensions for Chemopreventive Drug Monitoring. *Photochem. Photobiol.* **81**, 125–34 (2004).

47. Ravichandra, B. & Joshi, P. G. Gangliosides asymmetrically alter the membrane order in cultured PC-12 cells. *Biophys. Chem.* **76**, 117–132 (1999).
48. Cranfill, P. J. *et al.* Quantitative assessment of fluorescent proteins. *Nat. Methods* **13**, 557–562 (2016).
49. Storoni, L. C., McCoy, A. J. & Read, R. J. Likelihood-enhanced fast rotation functions. *Acta Crystallogr. Sect. D Biol. Crystallogr.* **60**, 432–438 (2004).
50. Shu, X., Shaner, N. C., Yarbrough, C. A., Tsien, R. Y. & Remington, S. J. Novel Chromophores and Buried Charges Control Color in mFruits. *Biochemistry* **45**, 9639–9647 (2006).
51. Emsley, P., Lohkamp, B., Scott, W. G. & Cowtan, K. Features and development of Coot. *Acta Crystallogr. Sect. D Biol. Crystallogr.* **66**, 486–501 (2010).
52. Adams, P. D. *et al.* PHENIX: A comprehensive Python-based system for macromolecular structure solution. *Acta Crystallogr. Sect. D Biol. Crystallogr.* **66**, 213–221 (2010).
53. Shaner, N. C. *et al.* Improved monomeric red, orange and yellow fluorescent proteins derived from *Discosoma* sp. red fluorescent protein. *Nat. Biotechnol.* **22**, 1567–1572 (2004).
54. Rajendran, M. *et al.* Imaging pH Dynamics Simultaneously in Two Cellular Compartments Using a Ratiometric pH-Sensitive Mutant of mCherry. *ACS Omega* **3**, 9476–9486 (2018).
55. Drobizhev, M., Tillo, S., Makarov, N. S., Hughes, T. E. & Rebane, A. Color Hues in Red Fluorescent Proteins Are Due to Internal Quadratic Stark Effect. *J. Phys. Chem. B* **113**, 12860–12864 (2009).
56. Mongeon, R., Venkatachalam, V. & Yellen, G. Cytosolic NADH-NAD⁺ Redox Visualized in Brain Slices by Two-Photon Fluorescence Lifetime Biosensor Imaging. *Antioxid. Redox Signal.* **25**, 553–563 (2016).
57. Hutchinson, C. L., Lakowicz, J. R. & Sevick-Muraca, E. M. Fluorescence lifetime-based sensing in tissues: a computational study. *Biophys. J.* **68**, 1574–1582 (1995).
58. Kuwana, E. & Sevick-Muraca, E. M. Fluorescence Lifetime Spectroscopy for pH Sensing in Scattering Media. *Anal. Chem.* **75**, 4325–4329 (2003).
59. Draxler, S. & Lippitsch, M. E. Lifetime-Based Sensing: Influence of the Microenvironment. *Anal. Chem.* **68**, 753–757 (1996).
60. Nakabayashi, T. *et al.* A Correlation between pH and Fluorescence Lifetime of 2',7'-Bis(2-Carboxyethyl)-5(6)-carboxyfluorescein (BCECF) In Vivo and In Vitro. *Chem. Lett.* **36**, 206–207 (2007).

61. Martinez, K. A. *et al.* Cytoplasmic pH Response to Acid Stress in Individual Cells of *Escherichia coli* and *Bacillus subtilis* Observed by Fluorescence Ratio Imaging Microscopy. *Appl. Environ. Microbiol.* **78**, 3706–3714 (2012).
62. Balaev, A. E., Dvoretzki, K. N. & Doubrovski, V. A. <title>Refractive index of <emph type="1">escherichia coli</emph> cells</title>. in (ed. Tuchin, V. V.) **4707**, 253–260 (International Society for Optics and Photonics, 2002).
63. Tregidgo, C., Levitt, J. A. & Suhling, K. Effect of refractive index on the fluorescence lifetime of green fluorescent protein. *J. Biomed. Opt.* **13**, 031218 (2008).
64. Padan, E., Zilberstein, D. & Rottenberg, H. The proton electrochemical gradient in *Escherichia coli* cells. *Eur. J. Biochem.* **63**, 533–41 (1976).
65. Navon, G., Ogawa, S., Shulman, R. G. & Yamane, T. High-resolution ³¹P nuclear magnetic resonance studies of metabolism in aerobic *Escherichia coli* cells. *Proc. Natl. Acad. Sci. U. S. A.* **74**, 888–91 (1977).
66. Maurer, L. M., Yohannes, E., Bondurant, S. S., Radmacher, M. & Slonczewski, J. L. pH regulates genes for flagellar motility, catabolism, and oxidative stress in *Escherichia coli* K-12. *J. Bacteriol.* **187**, 304–19 (2005).
67. Kannan, G. *et al.* Rapid acid treatment of *Escherichia coli*: transcriptomic response and recovery. *BMC Microbiol.* **8**, 37 (2008).
68. Slonczewski, J. L., Rosen, B. P., Alger, J. R. & Macnab, R. M. pH homeostasis in *Escherichia coli*: measurement by ³¹P nuclear magnetic resonance of methylphosphonate and phosphate. *Proc. Natl. Acad. Sci. U. S. A.* **78**, 6271–5 (1981).
69. Yaginuma, H. *et al.* Diversity in ATP concentrations in a single bacterial cell population revealed by quantitative single-cell imaging. *Sci. Rep.* **4**, 6522 (2015).
70. Imamura, H. *et al.* Visualization of ATP levels inside single living cells with fluorescence resonance energy transfer-based genetically encoded indicators. *Proc. Natl. Acad. Sci. U. S. A.* **106**, 15651–6 (2009).
71. Kaleta, C., Schäuble, S., Rinas, U. & Schuster, S. Metabolic costs of amino acid and protein production in *Escherichia coli*. *Biotechnol. J.* **8**, 1105–1114 (2013).
72. Bennett, B. D. *et al.* Absolute metabolite concentrations and implied enzyme active site occupancy in *Escherichia coli*. *Nat. Chem. Biol.* **5**, 593–9 (2009).
73. Yao, R. *et al.* Elucidation of the co-metabolism of glycerol and glucose in *Escherichia coli* by genetic engineering, transcription profiling, and (¹³C) metabolic flux analysis. *Biotechnol. Biofuels* **9**, 175 (2016).

74. Heikal, A. A., Hess, S. T. & Webb, W. W. Multiphoton molecular spectroscopy and excited-state dynamics of enhanced green fluorescent protein (EGFP): acid–base specificity. *Chem. Phys.* **274**, 37–55 (2001).
75. Li, W., Houston, K. D. & Houston, J. P. Shifts in the fluorescence lifetime of EGFP during bacterial phagocytosis measured by phase-sensitive flow cytometry. *Sci. Rep.* **7**, 40341 (2017).
76. Tang, S. & Yasuda, R. Imaging ERK and PKA Activation in Single Dendritic Spines during Structural Plasticity. *Neuron* **93**, 1315-1324.e3 (2017).
77. Chen, Y., Saulnier, J. L., Yellen, G. & Sabatini, B. L. A PKA activity sensor for quantitative analysis of endogenous GPCR signaling via 2-photon FRET-FLIM imaging. *Front. Pharmacol.* **5**, 56 (2014).
78. Colgan, L. A. *et al.* PKC α integrates spatiotemporally distinct Ca²⁺ and autocrine BDNF signaling to facilitate synaptic plasticity. *Nat. Neurosci.* **21**, 1027–1037 (2018).
79. Van der Krogt, G. N. M., Ogink, J., Ponsioen, B. & Jalink, K. A comparison of donor-acceptor pairs for genetically encoded FRET sensors: Application to the Epac cAMP sensor as an example. *PLoS One* **3**, (2008).
80. Laviv, T. *et al.* Simultaneous dual-color fluorescence lifetime imaging with novel red-shifted fluorescent proteins. *Nat. Methods* **13**, 989–992 (2016).
81. Marvin, J. S. *et al.* An optimized fluorescent probe for visualizing glutamate neurotransmission. *Nat. Methods* **10**, 162–170 (2013).
82. Takanaga, H., Chaudhuri, B. & Frommer, W. B. GLUT1 and GLUT9 as major contributors to glucose influx in HepG2 cells identified by a high sensitivity intramolecular FRET glucose sensor. *Biochim. Biophys. Acta - Biomembr.* **1778**, 1091–1099 (2008).

CHAPTER 4. TOWARDS THE DEVELOPMENT OF A RECEPTOR INTERNALIZATION ASSAY WITH PH-SENSITIVE FLUORESCENT PROTEINS

4.1 Introduction

4.1.1 Receptor trafficking and regulation

Inter and intracellular signaling are vital for the maintenance of cell health and communication¹⁻⁴. Families like G-protein coupled receptors (GPCRs) contribute to a number of physiological processes, including immune and nervous system regulation, as well as cell growth and proliferation^{5,6}. In fact, dysregulation in signaling cascades initiated by GPCRs can result in the metastasis of some cancers⁷. Cell surface receptors thus play a crucial role in the initiation and propagation of cell signaling. After stimulation by an agonist, receptors undergo conformational changes that translate intracellularly to secondary messengers that modulate cell cycle and function⁸. After prolonged stimulation, receptors are regulated in a number of ways: 1) Desensitization: Receptors become non-responsive to continued agonist stimulus, resulting in decreased intracellular response by second messengers. 2) Endocytosis or Internalization: Receptors are engulfed and removed from the cell surface for degradation in lysosomes or recycling back to the membrane^{5,9}. However, within these two categories lies a multitude of combinations. For example, receptors can resensitize after agonist-induced desensitization, or continue signaling during early endosomal processing. In some cases, such as the transporters aquaporin or GLUT4, receptors are expressed on the cell surface in negligible levels, and are transported to the cell membrane after stimulation by a complex and poorly understood coordination of secondary messengers and transport proteins^{10,11}. Thus, there remains a need to investigate the dynamic and variable flux in receptor trafficking and signaling control.

4.1.2 Glucose Transporter (GLUT) 4: Trafficking and role in neurodegeneration

In neurons, proper production and trafficking of mitochondria is vital for energy consuming action potentials and rapid neurotransmission. In fact, even acute disruptions in ATP supply cause immediate and drastic effects on neuron function¹². However, the unique shape and structure of these cells makes it difficult to effectively supply this energy throughout the cell. To achieve efficient signaling within the CNS, as well as communicate with peripheral organs, neurons must

extend out, sometimes developing long (1 m) axons and highly branched dendritic spines. As neurons need sufficient supply of mitochondria in both the soma as well as trafficked along axons and dendrites, failure in mitochondrial transport or electron chain dysfunction can lead to increased reactive oxygen species (ROS) resulting in insufficient ATP production and neuron degradation¹³. In fact, loss of neurons in the *substantia nigra* is one of the hallmarks of Parkinson's Disease pathology and has been correlated with impaired mitochondrial function¹⁴. However, it has been recently reported that attenuation of severe damage due to mitochondrial dysfunction is possible, at least temporarily, by redistribution of glycolysis metabolites and in PD models, neurons uptick glycolysis in an attempt to compensate for the loss in mitochondrial ATP production^{14,15}. In fact, diminished glucose uptake is observed in both Alzheimers and Parkinson's patients by F19-Positron Emission Tomography (PET), with research underway to determine if this hallmark could serve as a viable clinical diagnostic¹⁶. However, studying the biochemical mechanisms behind this switch is difficult, due to the lack of tools to spatially and temporally resolve key players and dynamics in both healthy and disease states.

Glucose transporters (GLUTs) play a key role in glycolysis, functioning as shuttles of glucose from high extracellular concentrations to low intercellular concentrations, feeding ready glycolytic machinery. These transporters differ in their glucose binding efficiency, expression and distribution, which is largely dependent on cell type and metabolic need¹⁷. For instance, GLUT1-3 are constitutively targeted to the membrane, with high affinity GLUT3 ($K_m \sim 1.5$ mM) mainly present in the brain where the glucose demand is consistently high. The activity of other glucose transporters, such as GLUT4, is modulated by extracellular stimuli¹⁸. In the presence of insulin, GLUT4 insertion in the extracellular membrane increases dramatically, with subsequent glucose transport increasing by as much as 40-fold. In the absence of insulin, basal levels of membrane-embedded GLUT4 plummet to almost negligible amounts. Though primarily expressed in muscle and adipose tissue, *in vivo* staining shows the importance of GLUT4 in activity-dependent glucose transport in neurons^{10,19}. However, it is largely debated how signaling from insulin-receptor binding is translated to GLUT4 expression on the plasma membrane. There are currently opposing theories; GLUT4 is packaged into vesicles in a static location until insulin binding to receptors, or a flux of vesicle endo- and exocytosis favors release after stimulus. Recently, the small G protein Rab10 has been linked to GLUT4 relocation. Studies show upwards of a 50% decrease in membrane localized GLUT4 in the absence of Rab10, in both cultured adipocytes as well as

knockout mice^{20,21}. Interestingly, Rab10 is also a substrate for leucine-rich repeat kinase 2 (LRRK2), a kinase well-studied for its role in Parkinson's Disease pathology²². Mutations in LRRK2 have been shown to increase enzyme activity, and inhibition of LRRK2 results in decreased levels of phosphorylated Rab10^{22,23}. With this direct correlation, it is reasonable to hypothesize LRRK2 malfunction would have a direct effect on both Rab10 localization in neurons as well as inherent ability to relocate GLUT4 to the plasma membrane. To date there are two generalized methods for tracking GLUT4 in live cells: 1) From receptor stimulus to downstream intracellular targets, and 2) From GLUT4 protein expression to plasma membrane fusion. Here we propose a method to combine these detection pathways. Using genetically encoded fluorescent tools to label GLUT4, as well as modulators Rab10 and LRRK2, we can broaden metabolic analysis both spectrally and temporally in healthy and disease state neurons.

4.1.3 Utilizing the SpyTag/SpyCatcher platform for monitoring receptor internalization

Developed by the Howarth laboratory, the SpyTag/SpyCatcher features a peptide-protein interaction that forms a spontaneous isopeptide bond when in close proximity and correct orientation (Figure 33)^{24,25}. Once formed, this covalent bond resists environmental degradation and has been used in several applications including enzyme stabilization and vaccine optimization^{26,27}. Similar to small peptide epitopes such as FLAG (8 amino acids) or myc (10 amino acids), SpyTag (13 amino acids) can easily be engineered into a protein of interest, with its larger protein counterpart SpyCatcher (138 amino acids) either expressed as a fusion with another protein of interest or coupled to a dye or fluorescent protein to monitor localization of SpyTagged domains after removal of unbound SpyCatcher²⁸. When expressed in cells, the SpyTag/SpyCatcher chemistry displayed slow kinetics, so a second generation SpyTag (SpyTag002) was optimized to increase SpyTag-Spycatcher reactivity for live cell applications²⁹. Recently, this platform was used to successfully label channelrhodopsins (ChR) expressed in HEK cells, as well as showed labeling of ChR expression in neurons does not significantly affect function *in vitro*²⁶. We decided to utilize this strategy to tag membrane bound receptors post-translationally to monitor their dynamics *in vitro*. A novel aspect to our approach is our use of fluorescent protein pH sensors that will also allow us to discriminate trafficking through early (near neutral pH) and late (acidic) endosomes.

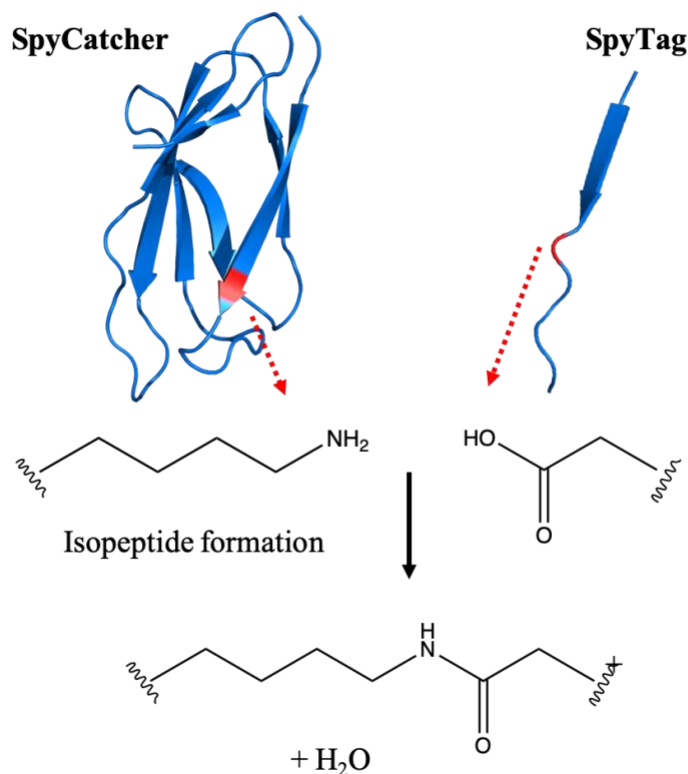


Figure 33 SpyTag-SpyCatcher chemistry

Isopeptide formation between Lys31 of the SpyCatcher protein and Asp117 of the SpyTag peptide can be utilized for post-translational modification of cellular proteins.

4.2 Materials and Methods

Unless otherwise stated, chemicals were purchased from Sigma Aldrich; molecular biology enzymes were purchased from New England Biolabs (NEB); plasmid templates were purchased from Addgene; cell culture media and supplements were purchased from Invitrogen. HEK-293a cells were purchased from ATCC.

4.2.1 Molecular Biology

pQE80L-SpyCatcher-ELP-GFP was digested with SacI and BamI for GFP removal. pHluorin2 was amplified from pME-pHluorin2-gpi using primers GTGTGCCGGGCGTTGGTGAGCTCATGGTcAGCAAGGGCGAGGAGCT (forward) and GCTTTGTTAGCAGCCGGATCCtcatcaTFACTTGTACAGCTCGTCCATGC (reverse) then added to template via Gibson assembly. mKeima was amplified from Addgene56018-

mKeimaRed-mito7 using primers GTGTGCCGGGCGTTGGTGAGCTCATGGTGAGTGTGATCGCTAAAC (forward) and GCTTTGTTAGCAGCCGGATCCtcatcaTTAACCGAGCAAAGAGTGGC (reverse) then added to template via Gibson assembly. A gBlock was ordered containing sequencing for a secondary spytag (SpyTag002), tandem BC2 tags (2xBC2), and primary spytag (SpyTag001), and amplified with primers CGGACGCGCGTTCGACAGACTATAAAGATGACGATGACGG (forward) and GTTCTTCGGCTTCGCGTAcTTGTTGCCAGTGAGAAACAG (reverse). The amplified tag was added to the N-terminus of GLUT4-mCherry by linearization of pLenti-myc-GLUT4-mCherry with AgeI and Gibson assembly with gblock amplified PCR product. SpyTag was added to the N-terminus of pCMV-hP2YR11 via Q5 mutagenesis with primers AAGCCGACGAAGGGTTCAGGGGGTGACGCCAGCATCGATATG (forward) and GTAGGCGTCCACCATCACAATGTGAGCTCCGGCGAATACCAGGCAGAAG (reverse). mTurquoise2 was added to the C-terminus of SpyTag-hP2YR11 by first amplifying mTurquoise2 from the vector pBAD-mTurquoise2 using primers gatattcgcttgatcgataccggtATGGTGAGCAAGGGCGAG (forward) and ctaatgtctagactcgagtcTTACTTGTACAGCTCGTCCATGC (reverse) and digesting both PCR product and template with AgeI and XbaI. Products were assembled using T4 ligation.

4.2.2 SpyCatcher protein production and purification

SpyCatcher-ELP-pHluorin2 and SpyCatcher-ELP-mKeima were transformed into BL21(DE3) E. coli cells and grown in Autoinduction Media (Formedium) at 37 °C in baffled flasks with continuous shaking overnight for 12-16 hours followed by 2-3 days of continuous shaking at ambient temperatures. Cells were pelleted at 6,000xg and stored at -80 °C until purification. His-tagged protein was purified by nickel-affinity chromatography using a HiTrap IMAC column (Amersham) according to manufacturer instructions. Purified protein was dialyzed against storage buffer (5 mM MOPS, 300 mM NaCl, 10% glycerol, pH 7.3), concentrated to 500 uL using a 10,000 MWCO Amicon Centrifugal Filter (Millipore), and stored at -20 °C for immediate use or -80 °C for extended storage.

4.2.3 Steady-State Fluorescence Spectroscopy

SpyCatcher-ELP-pHluorin2 was diluted to μM 1 in assay buffer containing 50 mM Tris, 50 mM Bis-Tris, 50 mM MOPS adjusted to pH 5.5, 7.5 or 9.0 with NaOH and HCl. Fluorescence was measured on a microplate reader (Biotek synergy H5). Excitation spectra were measured using a monochromator with a fixed emission at 510/9 nm and excitation scanned from 370-490 nm with a 9 nm excitation bandpass.

4.2.4 Mammalian Cell Culture, Transfection, and Live-Cell Imaging

HEK-293 cells were cultured at 37 °C in 5% CO₂ humidified air incubator in DMEM media containing 10% Cosmic calf serum (Hyclone). Cells were transfected using calcium phosphate and imaged after 2 days. Cells were imaged in high potassium imaging solution (mM: 1.25 NaH₂PO₄, 125 KCl, 2 CaCl₂, 1 MgCl₂, 10 glucose). mCherry fluorescence images were collected using 550/15 nm excitation, 570 nm longpass dichroic, and 585/20 nm emission filters. pHluorin2 fluorescence images were collected using 474/34 nm and 395/25 nm excitation, and 525/50 emission filter. mTurquoise2 fluorescence images were collected using 438/29 nm excitation, multiband dichroic, and 470/20 nm emission filters. 200-400 μM SpyCatcher-ELP-pHluorin2 was diluted to 20-40 μM in imaging solution directly onto cells and incubated at room temperature for 30 mins to 1 hr. Cells were washed gently 3-5x with imaging solution and imaged immediately after to localize staining.

4.3 Results

Glucose transporters are difficult to track as they are not constitutively expressed in large quantities on the plasma membrane and are instead trafficked intracellularly until insulin stimulation. Our long-term hypothesis is that PD associated mutations in LRRK2 kinase inhibit GLUT4 translocation to metabolically destabilize neurons through altered Rab10 signaling. Burchfield et al. showed successful labeling of GLUT4 using green fluorescent protein (GFP), however, as both the N and C terminus of the transporter are heavily involved in signaling, engineering of the GFP was done within an exterior loop³⁰. Thus, in this project we tested the SpyTag-SpyCatcher labeling strategy by engineering SpyTags into both an exterior loop of GLUT4 as well as an orthogonal approach labeling the free N-terminus of the unrelated purinergic

receptor P2YR11. For the label, we engineered two different SpyCatcher fusions to the ratiometric red fluorescent mKeima and green fluorescent pHluorin2 pH sensors.

4.3.1 Engineering SpyTag-GLUT4 for labeling with pH sensitive fluorescent protein fusion SpyCatcher-pHluorin2

We first tested whether fusion of the ratiometric pH sensitive pHluorin2 with SpyCatcher would alter its function *in vitro*. The pHluorin2 protein was fused to the C-terminus of the SpyCatcher protein with a flexible Elastin-Like Protein (ELP) linker to prevent the fluorescent protein domain from sterically inhibiting the SpyCatcher binding and chemistry³¹. After gel separation confirmed purified SpyCatcher-ELP-pHluorin2 was intact, we diluted the protein in buffer at pH 5.5, 7.5 and 9.0 and saw expected shifts in excitation peaks as a function of pH (Figure 2). We then moved forward with tagging the GLUT4 receptor for staining with SpyCatcher-ELP-pHluorin2. Burchfield et al. showed successful engineering of GFP in an exterior loop of the transporter GLUT4 which did not disrupt expression or signaling in mammalian cells³⁰.

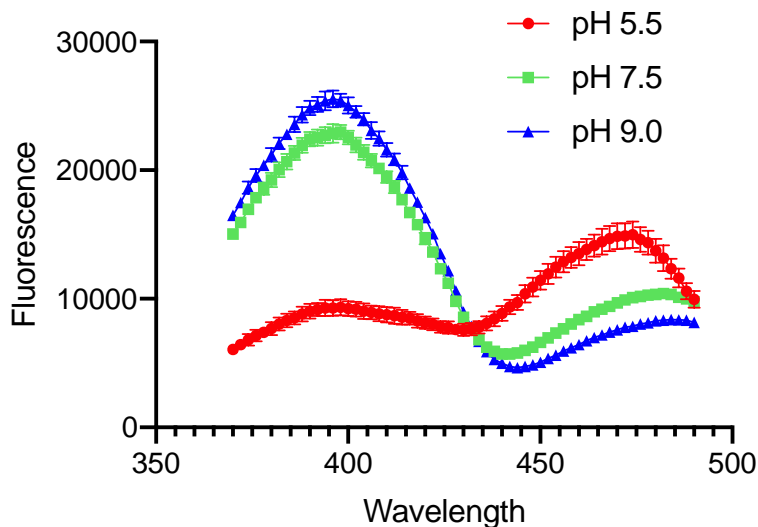


Figure 34 SpyCatcher-pHluorin fusion retains characteristic pH response *in vitro*

1 μ M protein was diluted in buffer at pH 5.5, 7.5 or 9.0 and showed expected changes in dual excitation peaks as a function of pH, with acidic conditions showing increased 475 nm excitation, and alkaline conditions showing increased 395 nm excitation.

We next engineered tandem SpyTags into the first luminal-extracellular loop of a rat GLUT4-mCherry fusion. The C-terminal red fluorescent mCherry provided a label to observe the total GLUT4 population without interfering with pHluorin2 green fluorescence. In preliminary studies, we found successful expression of SpyTag002-SpyTag001-GLUT4-mCherry in HEK293a cells (Figure 35). After staining with 20 μ M SpyCatcher-ELP-pHluorin2 for 1 hour at room temperature, pHluorin2 fluorescence was detected (Figure 35). The green fluorescence from pHluorin2 was weak, but it was above background and cannot be accounted for by spectral bleedthrough from the mCherry. The pHluorin2 green fluorescence co-localized onto the same cells exhibiting red fluorescence from GLUT4-mCherry but not onto neighboring cells lacking GLUT4-mCherry, indicating specific labeling (Figure 35, Figure 36). Furthermore, control experiments showed that SpyCatcher-ELP-pHluorin2 did not label untransfected cells. We hypothesized weak staining could be due to poor basal GLUT4 surface expression, which could be tested with an insulin dose response to see if GLUT4 membrane expression increases for subsequent staining with SpyCatcher; slow SpyTag/SpyCatcher chemistry even with optimized SpyTag002 present, which could make for overall poor *in vivo* application; or decreased accessibility due to engineering into an external loop. To test tag accessibility, we pursued an orthogonal approach appending the SpyTag sequence onto the N-terminus of a P2Y receptor protein.

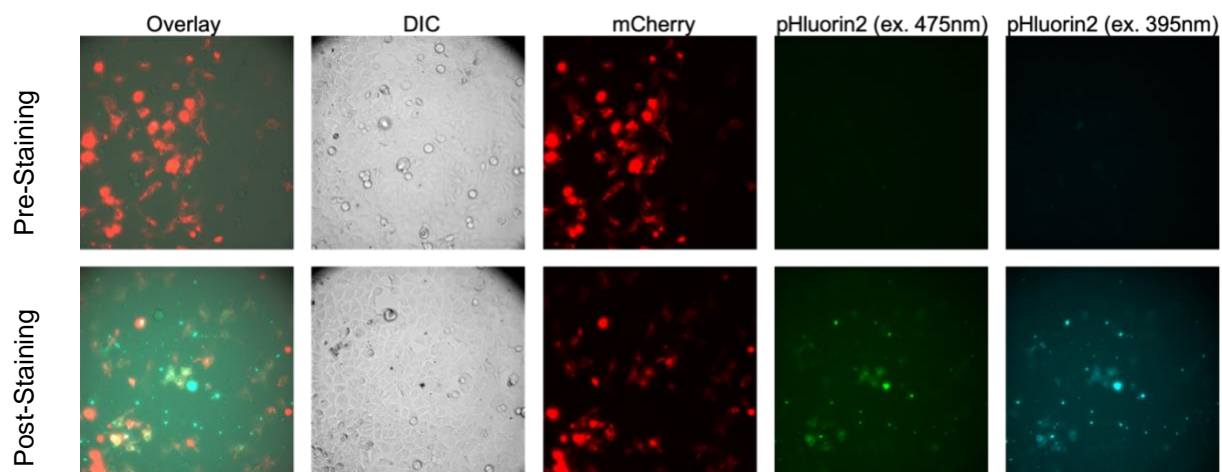


Figure 35 SpyTag-GLUT4-mCherry expression in HEK293a cells Before (upper panels) and after (lower panels) staining with 20 μ M SpyCatcher-ELP-pHluorin2 for 1 hour in ambient conditions. pHluorin2 is weakly detected but present after washing with imaging solution.

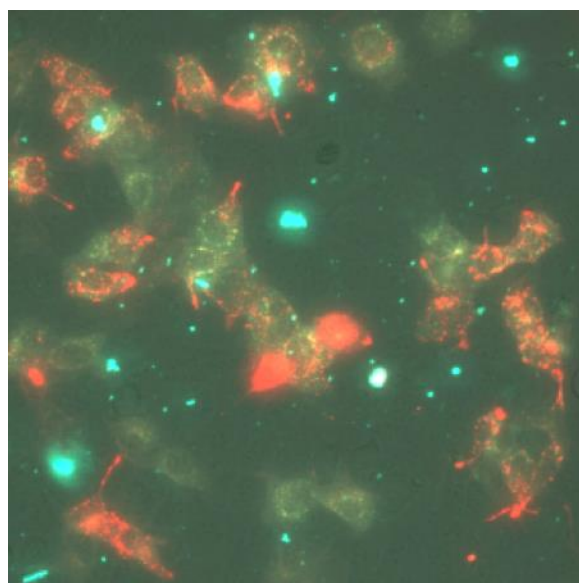


Figure 36 Zoom in of SpyTag-GLUT4-mCherry/SpyCatcher-ELP-pHluorin2 overlay Here we see localization of GLUT4 via mCherry fluorescence at the membrane as well as internally packaged (noted by internal red puncta). Importantly, after staining with SpyCatcher-ELP-pHluorin2, we do not see pre-existing GLUT4 in endosomes labeled with pHluorin2, as expected, and do see co-localization of SpyCatcher-ELP-pHluorin2/SpyTag-GLUT4-mCherry at the membrane.

4.3.2 Purinergic P2Y receptors and GPCR signaling control

Purinergic P2Y receptors (P2YR), a subset of G protein-coupled receptors (GPCRs), are activated by adenine and uridine nucleotides which lead to a number of downstream processes including cell growth and differentiation^{32,33}. In recent studies, increased P2YR11 gene amplification was seen in patients with narcolepsy, however, studies on P2Y11 mechanism and function in disease models is lacking. This is due in part by the inefficiency of targeted antibodies, as well as the absence of a murine homolog, making exploratory analysis in knock out mice impossible⁸. By developing optical tools to study P2YR11 trafficking and signaling, we can broaden our knowledge of P2Y function, as well as provide information broadly about receptor internalization as a method of GPCR control.

Activation of the P2Y11 receptor with ATP or UTP causes a canonical $G\alpha_q$ -dependent activation of phospholipase C- β (PLC β), producing second messengers that mobilize intracellular calcium³³. Upon desensitization, β -arrestin is recruited and receptors are quickly shuffled to early endosomes where they will follow two main trafficking pathways: 1. Receptors are dephosphorylated in the endosomal compartment, to then be recycled back to the plasma membrane, or 2. Receptors are internalized in lysosomes, inducing further acidification and receptor degradation³⁴.

G protein-dependent signaling by receptors was traditionally thought to be localized on the plasma membrane. However, over the past decade, studies have provided evidence that internalized GPCRs can *continue signaling*, even after removal from the cell membrane surface³⁵. By spatiotemporally resolving oscillations in P2Y activity due to persistence of ligand, desensitization of receptor, and further signaling after recruitment into endosomal vesicles, we can further our understanding of the complex dynamics in GPCR signaling and receptor internalization. Here we discuss a method for N-terminally tagging the P2Y11 receptor with a short, genetically encoded sequence, which covalently binds to a fluorescent fusion protein when introduced extracellularly. By fluorescently tagging the receptor after proper insertion in the membrane, we can track endocytosis and recycling kinetics, as well as co-express spectrally compatible downstream targets to monitor receptor signaling dynamics both imbedded in the membrane and after endosomal formation and binding with β -arrestins.

4.3.3 Engineering a SpyTag-P2YR11 for labeling with pH sensitive fluorescent protein SpyCatcher fusions

We first engineered the SpyTag001 peptide sequence on the free N-terminus of P2YR11, with the objective of specific receptor labeling using the SpyCatcher-ELP-pHluorin2 or SpyCatcher-ELP-mKeima. When added in μM concentrations, labeled receptors would covalently bind to SpyCatcher fusions, allowing receptor staining and thus tracking of the receptor as well as pH dynamics throughout endosomal processing or recycling. After transfection of the SpyTag-P2YR11 construct in HEK293a cells, we began a series of conditions to stain with purified SpyCatcher-pHluorin protein. Reported protocols call for staining at room temperature for 30 min – 1 hr with 25 μM SpyCatcher protein. Our goal was to both stain the receptor, and control endocytic events, therefore we attempted three temperature conditions. 1) 4°C for 1 hr to slow down endocytosis kinetics while staining, which could engulf our sensor before further manipulating extracellular stimulus. 2) Ambient conditions for 1 hr to repeat published protocols. 3) 37°C for 1 hr to assess whether increased temperature increased rate of reaction for SpyTag-SpyCatcher binding. At 4°C, we found overwhelming cell death, making cells unusable. Unsurprisingly, we saw greatest success with a 1 hr ambient incubation, with potential staining determined qualitatively, although very weak (Figure 37A-B). However, without a fluorescent label on the receptor, we were unable to determine expression levels of the transfected construct. To investigate our transfection efficiency, we first co-expressed mApple with SpyTag-P2YR11 and saw efficient mApple expression and signal. Confident in our transfection approach, we moved to engineer a spectrally compatible fluorescent protein on the C terminus of the SpyTag labeled receptor. SpyTag-P2YR11-mTurquoise2 showed successful expression and membrane labeling, however, after staining with both SpyCatcher-pHluorin or SpyCatcher-mKeima with 10-25 μM protein at room temperature or 37°C for 1 hr, we were unable to see localized staining (Figure 37C-F). After running the construct through a SignalIP server, correct cleavage after the engineered HA trafficking signal sequence was determined, however, there was also a 40% probability cleavage would occur after the SpyTag, removing the SpyTag altogether. Strategies were developed to attack this problem in two ways: 1) Repair the N terminus by adding a FLAG tag after the HA signal peptide to ensure proper cleavage and 2) The addition of an optimized SpyTag002 tag for increased efficiency of isopeptide bond formation. This increased potential

labeling targets from one to two, as well as extended the tag further into the extracellular space, potentially increasing opportunities for binding. Molecular biology for this strategy is underway.

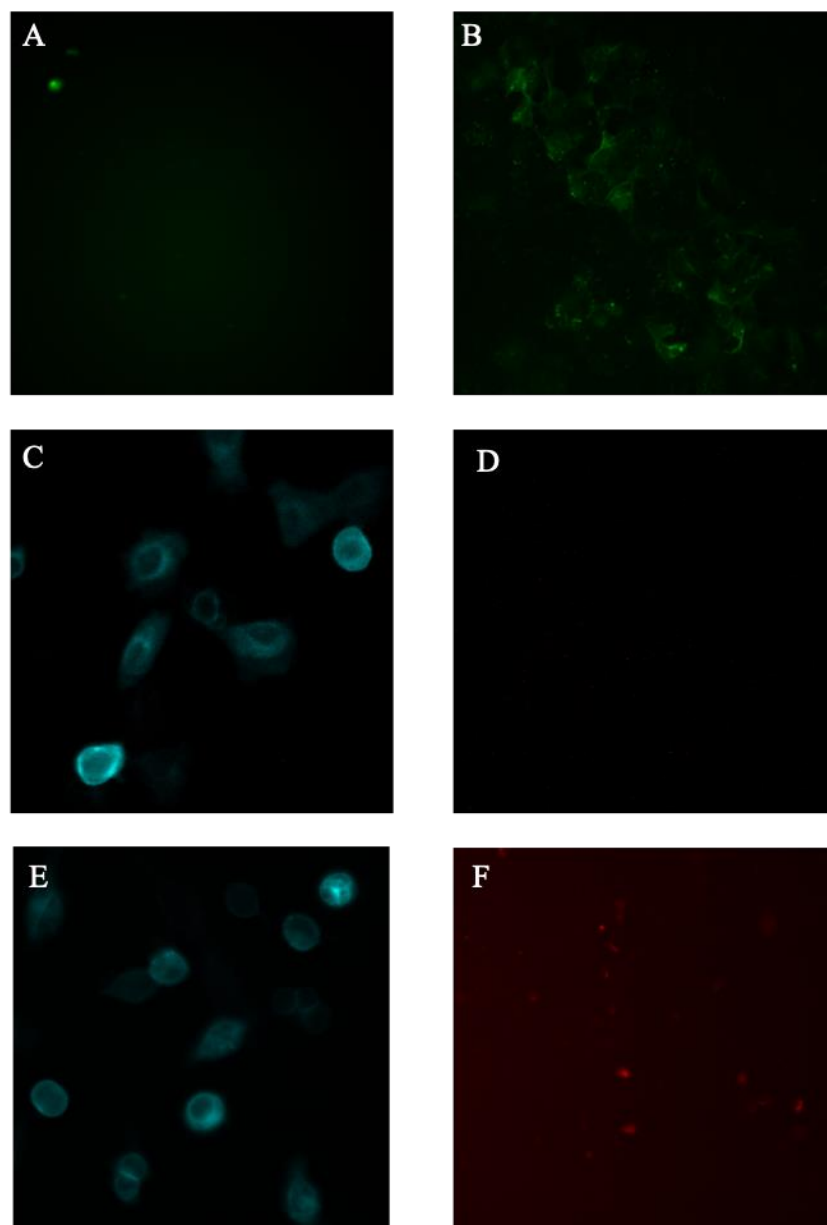


Figure 37 SpyCatcher staining of SpyTag-P2YR11 in HEK293a cells

A-B) HEK293a cells stained with 25 μ M SpyCatcher-pHluorin2 (emission 525nm) transfected with A) Vehicle and B) SpyTag-P2YR11. C-D) HEK293a cells transfected with SpyTag-P2YR11-mTurquoise2 pre-stain at C) 525 nm turquoise emission and D) 632 mKeima emission. E-F) SpyTag-P2YR11-mTurquoise2 transfected HEK293a cells post 1 hr incubation with 25 μ M SpyCatcher-mKeima at E) 525 nm turquoise emission and F) 632 mKeima emission. Although mTurquoise2 expression remained consistent, mKeima showed no co-localization and appeared to be absent after wash.

4.4 Conclusions and Future Directions

The SpyTag/SpyCatcher system to post-translationally label receptors in live-cell assays proved a potentially viable strategy. After tagging an extracellular loop of GLUT4 with dual SpyTag peptides, we saw weak but promising staining of SpyCatcher-pHluorin2 after co-incubation for one hour. Moving forward, we will further optimize our staining strategies to see clear tagging of the transporter with pHluorin2. Once optimized, it would also be interesting to combine this assay with fluorescent ATP sensors to see the effects of intra and extracellular ATP production as a function of GLUT4 localization to the membrane. Looking to proceed with an orthogonal tagging approach, we appended the SpyTag peptide onto the N-terminus of the purinergic receptor P2YR11. Recent studies showing overexpression of P2YR11 in patients with narcolepsy has prompted further investigation into its function, however, the lack of tools including a rodent genomic model make this difficult. After successfully expressing and locating SpyTag-P2YR11-mTurquoise in HEK293a cells, we saw minimal staining after several attempts using SpyCatcher-mKeima with varying incubation times, locations and temperatures. However, the SpyTag-P2YR11-mTurquoise labeled receptor showed signs of FP overexpression and variable membrane targeting. Moving forward, it should be determined if poor trafficking of P2YR11 is due to DNA overload during transfection, the appendage of a N-terminal tag or fusion with a C-terminal fluorescent protein. Once optimized, multiplex imaging with fluorescently labeled downstream signaling proteins such as cAMP or GRK2 sensors would be advantageous to monitor both endocytic receptor pathways as well as downstream signaling cascades in combination. Furthermore, as localization and organization of the glucose transporter GLUT4 is thought to be trafficked in part by the Rab GTPase Rab10, a substrate of the leucine rich repeat kinase LRRK2²³, coexpression of the red fluorescently labeled GLUT4 (GLUT4-mCherry) with cytosolically expressed green fluorescent labeled LRRK2 (LRRK2-eGFP) as well as the most commonly PD associated mutant LRRK2(G2019S)-eGFP could begin to tease apart this relationship. After co-expression has proven successful, we will test the location of GLUT4 in the presence or absence of insulin, with wild type and G2019S mutated LRRK2 to see the effects of LRRK2 on GLUT4 trafficking dynamics.

4.5 References

1. Elmore, S. Apoptosis: a review of programmed cell death. *Toxicol. Pathol.* (2007). doi:10.1080/01926230701320337
2. Ma, D. K. G., Stolte, C., Krycer, J. R., James, D. E. & O'Donoghue, S. I. SnapShot: Insulin/IGF1 Signaling. *Cell* (2015). doi:10.1016/j.cell.2015.04.041
3. Laplante, M. & Sabatini, D. M. MTOR signaling in growth control and disease. *Cell* (2012). doi:10.1016/j.cell.2012.03.017
4. Slack, C. *et al.* The Ras-Erk-ETS-Signaling Pathway Is a Drug Target for Longevity. *Cell* (2015). doi:10.1016/j.cell.2015.06.023
5. Cahill, T. J. *et al.* Distinct conformations of GPCR- β -arrestin complexes mediate desensitization, signaling, and endocytosis. *Proc. Natl. Acad. Sci.* **114**, 2562–2567 (2017).
6. Stoddart, L. A., White, C. W., Nguyen, K., Hill, S. J. & Pflieger, K. D. G. Fluorescence- and bioluminescence-based approaches to study GPCR ligand binding. *Br. J. Pharmacol.* **173**, 3028–3037 (2016).
7. Tomas, A., Futter, C. E. & Eden, E. R. EGF receptor trafficking: Consequences for signaling and cancer. *Trends Cell Biol.* **24**, 26–34 (2014).
8. Dreisig, K. & Kornum, B. R. A critical look at the function of the P2Y11 receptor. *Purinergic Signal.* **12**, 427–437 (2016).
9. Palacios, S., Lalioti, V., Martinez-Arca, S., Chattopadhyay, S. & Sandoval, I. V. Recycling of the Insulin-sensitive Glucose Transporter GLUT4. *J. Biol. Chem.* **276**, 3371–3383 (2001).
10. Ashrafi, G., Wu, Z., Farrell, R. J. & Ryan, T. A. GLUT4 Mobilization Supports Energetic Demands of Active Synapses. *Neuron* **93**, 606-615.e3 (2017).
11. Bryant, N. J., Govers, R. & James, D. E. Regulated transport of the glucose transporter GLUT4. *Nat. Rev. Mol. Cell Biol.* **3**, 267–277 (2002).
12. Zala, D. *et al.* Vesicular glycolysis provides on-board energy for fast axonal transport. *Cell* **152**, 479–491 (2013).
13. Demetrius, L. A. & Simon, D. K. An inverse-Warburg effect and the origin of Alzheimer's disease. *Biogerontology* **13**, 583–594 (2012).
14. Zhao, H. *et al.* Potential biomarkers of Parkinson's disease revealed by plasma metabolic profiling. *J. Chromatogr. B Anal. Technol. Biomed. Life Sci.* **1081–1082**, 101–108 (2018).

15. Anandhan, A. *et al.* *Metabolic Disorder Dysfunction in Parkinson's Disease: Bioenergetics, Redox Homeostasis and Central Carbon Metabolism HHS Public Access Author manuscript. Brain Res Bull* **133**, (2017).
16. Selnes, P. *et al.* Impaired synaptic function is linked to cognition in Parkinson's disease. *Ann. Clin. Transl. Neurol.* (2017). doi:10.1002/acn3.446
17. Navale, A. M. & Paranjape, A. N. Glucose transporters: physiological and pathological roles. *Biophys. Rev.* **8**, 5–9 (2016).
18. Vannucci, S. J. *et al.* GLUT4 glucose transporter expression in rodent brain: Effect of diabetes. *Brain Res.* **797**, 1–11 (1998).
19. Holman, G. D., Leggio, L. L. & Cushman, S. W. Insulin-stimulated GLUT4 glucose transporter recycling. A problem in membrane protein subcellular trafficking through multiple pools. *J. Biol. Chem.* **269**, 17516–17524 (1994).
20. Sano, H., Roach, W. G., Peck, G. R., Fukuda, M. & Lienhard, G. E. Rab10 in insulin-stimulated GLUT4 translocation. *Biochem. J.* **411**, 89–95 (2008).
21. Vazirani, R. P. *et al.* Disruption of adipose Rab10-dependent insulin signaling causes hepatic insulin resistance. *Diabetes* **65**, 1577–1589 (2016).
22. Atashrazm, F. *et al.* LRRK2-mediated Rab10 phosphorylation in immune cells from Parkinson's disease patients. *Mov. Disord.* **34**, 406–415 (2019).
23. Funk, N. *et al.* The Parkinson's disease-linked Leucine-rich repeat kinase 2 (LRRK2) is required for insulin-stimulated translocation of GLUT4. *Sci. Rep.* **9**, 1–16 (2019).
24. Bedbrook, C. N. *et al.* Genetically Encoded Spy Peptide Fusion System to Detect Plasma Membrane-Localized Proteins In Vivo. *Chem. Biol.* **22**, 1108–1121 (2015).
25. Veggiani, G. *et al.* Programmable polyproteins built using twin peptide superglues. *Proc. Natl. Acad. Sci. U. S. A.* **113**, 1202–7 (2016).
26. Keeble, A. H. *et al.* Protein–Protein Interactions Evolving Accelerated Amidation by SpyTag/SpyCatcher to Analyze Membrane Dynamics.
27. Wang, W. *et al.* Ferritin nanoparticle-based SpyTag/SpyCatcher-enabled click vaccine for tumor immunotherapy. *Nanomedicine Nanotechnology, Biol. Med.* **16**, 69–78 (2019).
28. Redington_2015_Secrets of a covalent interaction for biomaterials and biotechnology-SpyTag and SpyCatcher.
29. Keeble, A. H. *et al.* Evolving Accelerated Amidation by SpyTag/SpyCatcher to Analyze Membrane Dynamics. *Angew. Chemie - Int. Ed.* **56**, 16521–16525 (2017).

30. Burchfield, J. G. *et al.* Novel systems for dynamically assessing insulin action in live cells reveals heterogeneity in the insulin response. *Traffic* **14**, 259–273 (2013).
31. Gilbert, C., Howarth, M., Harwood, C. R. & Ellis, T. Extracellular Self-Assembly of Functional and Tunable Protein Conjugates from *Bacillus subtilis*. *ACS Synth. Biol.* (2017). doi:10.1021/acssynbio.6b00292
32. Khakh, B. S. & North, R. A. Neuromodulation by Extracellular ATP and P2X Receptors in the CNS. *Neuron* **76**, 51–69 (2012).
33. Erb, L. & Weisman, G. A. Coupling of P2Y receptors to G proteins and other signaling pathways. *Wiley Interdisciplinary Reviews: Membrane Transport and Signaling* (2012). doi:10.1002/wmts.62
34. Calebiro, D. & Godbole, A. Internalization of G-protein-coupled receptors: Implication in receptor function, physiology and diseases. *Best Practice and Research: Clinical Endocrinology and Metabolism* (2018). doi:10.1016/j.beem.2018.01.004
35. Kauppinen, R. A. & Nicholls, D. G. Synaptosomal bioenergetics: The role of glycolysis, pyruvate oxidation and responses to hypoglycaemia. *Eur. J. Biochem.* **158**, 159–165 (1986).

CHAPTER 5. APPLYING LANTHANIDE BINDING TAGS TO ENABLE THE USE OF FLUORESCENT PROTEIN SENSORS IN TR-LRET ASSAYS

5.1 Lanthanides as LRET donors

The introduction of genetically engineered fluorescent proteins has greatly enhanced the ability to detect both inter- and intra cellular dynamics, however, fluorescent proteins in the visible range are susceptible to signal contamination by autofluorescence both *in vitro* and *in vivo*. Additionally, background fluorescence from biological compounds such as flavins (FAD), pyridines (NAD) and collagen produce low signal to background ratios, reducing targeted detection sensitivity^{1,2}. Due to their unique spectral characteristics, lanthanide chelates have been utilized as donor modules for various biological sensors in both academic and commercial applications^{3,4}. Forbidden f-orbital transitions lead to long luminescence lifetimes (μ to ms), remarkably longer than fluorescent proteins or background fluorescence from matrix molecules (ns)^{5,6}. Long luminescence lifetimes have been exploited industrially, in fact, Homogeneous Time Resolved Fluorescence (HTRF) assays using lanthanide chelates have been developed by life sciences companies Cisbio and PerkinElmer. The commercially available TR-LRET Immunoassay kits LANCE® and DELFIA® have been optimized and distributed for a myriad of applications including GPCR functional and mechanistic assays, deconvoluting protein-protein interactions and large scale drug screening^{3,7-9}. While providing an efficient and user-friendly platform, these commercial assays are confined to a plate format, typically utilizing antibody labeling, with required lysis steps resulting in an inability to temporally resolve dynamic interactions *in vivo*. Therefore, optimizing time resolved assays for live cell microscopy using lanthanide chelates has been a subject of great interest.

The Imperiali group at MIT utilized the Ca^{2+} binding domain of the EF hand motif to optimize Terbium binding and excitation by positioning tyrosine and tryptophan residues as terbium antennas (Figure 38). These relatively short peptide sequences labeled Lanthanide Binding Tags (LBTs) have been thoroughly characterized, with apparent equilibrium dissociation constants in the nanomolar range¹⁰⁻¹². Typically consisting of six metal coordinating residues, this multi-dentate configuration creates a protective sphere around the ion, shielding it from potential decreased lifetime due to solvent quenching.

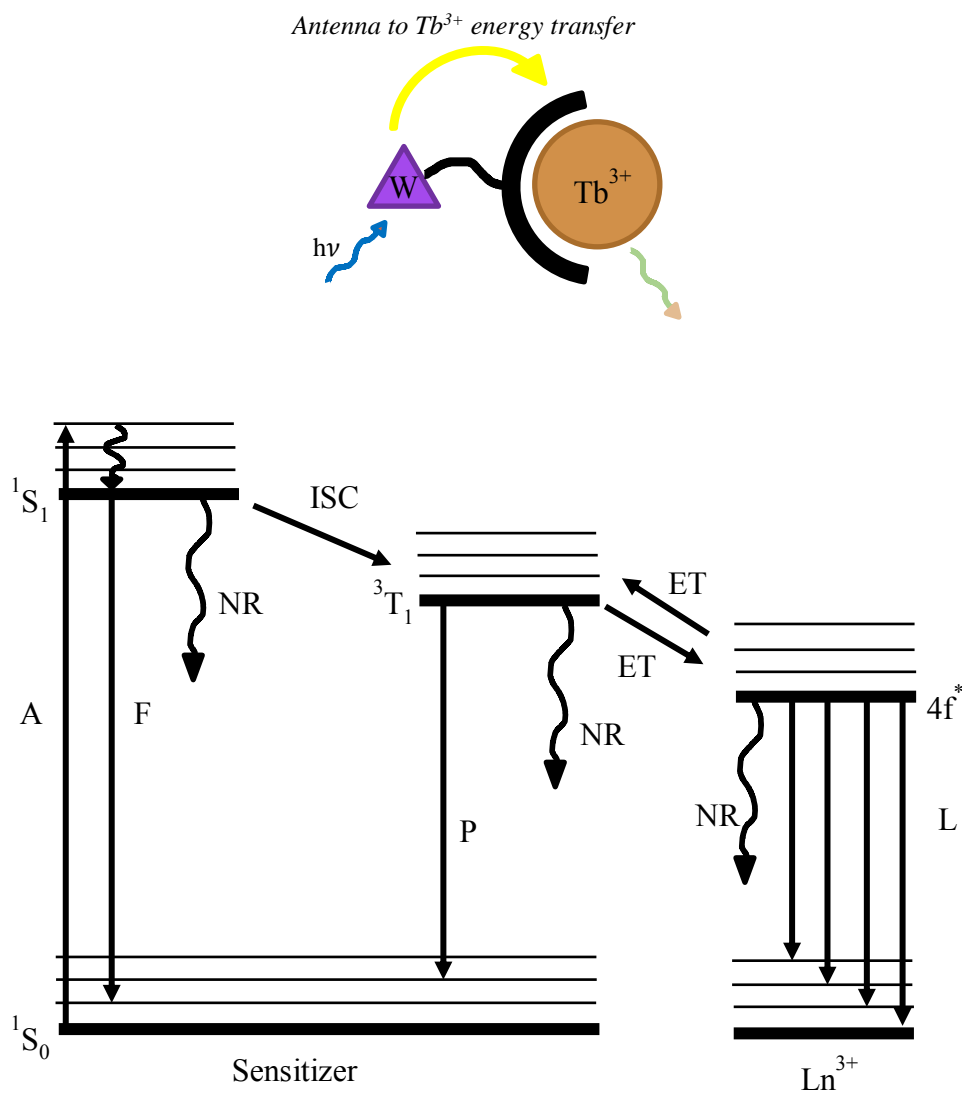


Figure 38 The 'antennae' effect. Lanthanide binding tags (LBTs) containing tryptophan residues act as lanthanide antennas, effectively transferring irradiated light to the metal ion. Energy (280 nm) absorbed by the Trp ligand sensitizer is transferred to $Ln(III)$ excited states.

Importantly, the LBT-Tb³⁺ complexes excite in the UV region, and do not overlap with most commonly utilized fluorescent proteins (ex: GFP variants), with excitation profiles in the 450-500 nm range¹³. Furthermore, these complexes exhibit long (μ s to ms) luminescence lifetime, orders of magnitude longer than the fluorescence lifetime of protein sensors (Figure 2). This extraordinarily long lifetime can thus be exploited for time resolved luminescence resonance energy transfer (LRET) by engineering these tags onto fluorescent protein targets^{10,14,15}. This relay relies on a non-radiative energy transfer from the Tb³⁺ bound tag to the fluorescent protein of interest. After a brief excitation pulse at 280nm, detection is delayed by a 50-150 μ s window to allow for the decay of inherent background fluorescence (nanoseconds) of other molecules in solution (Figure 39). This greatly decreases non-specific background signal, resulting in increased signal-to-background and sharper emission spectra (Figure 39). We hypothesized the addition of a LBT sequence could provide an easy method for non-radiative energy transfer to a fluorescent protein of our choosing. Easily genetically encoded, this tag could extend FP emission lifetime an order of magnitude, greatly decreasing background autofluorescence from matrix proteins and small molecules. We decided to test the addition of a luminescent lanthanide probe (LBT) onto eGFP as proof-of-concept to show LRET between an excited Tb-LBT chelate donor and a fluorescent protein acceptor. If it is possible to engineer long FP lifetimes with a lanthanide tag, we then hypothesized it could be possible to engineer conversion of a steady-state FRET based sensor into a time resolved LRET-FRET reporter. Fusion of the LBT onto the terminus of the donor FP could extend the donor FP lifetime, and thus extend the lifetime of the FRET relay. We chose the extensively characterized Protein Kinase A (PKA) FRET sensor AKAR as a proof-of-concept (Figure 40), with the goal of providing an easy way to extend FRET lifetime for applications in live-cell microscopy.

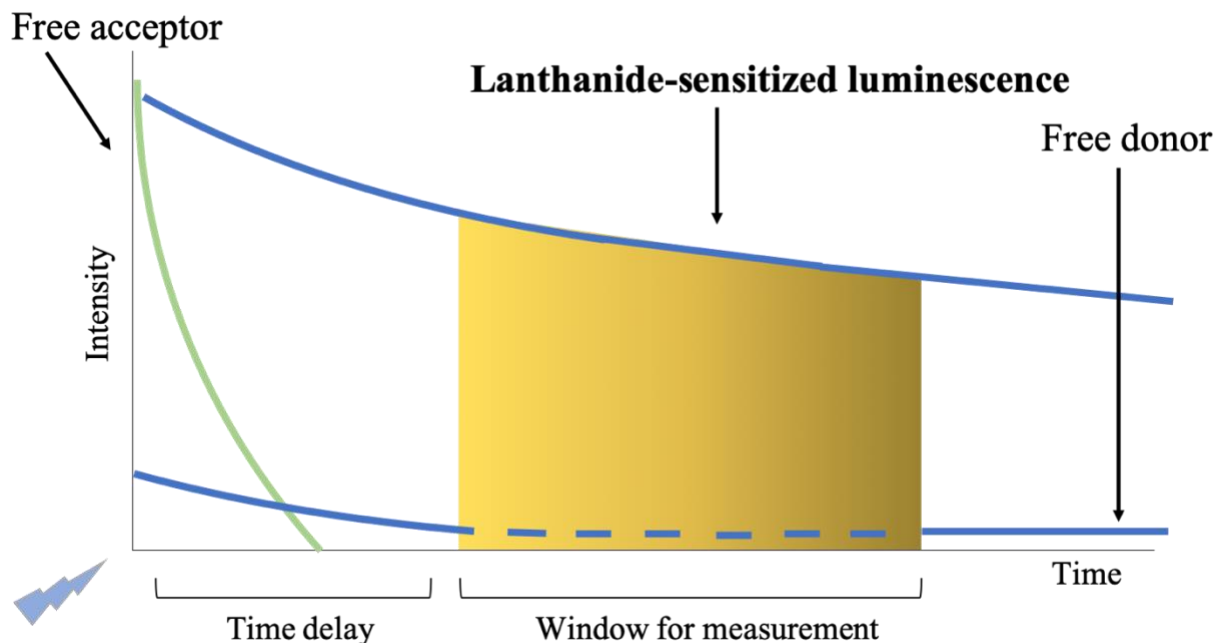


Figure 39 Lanthanide-sensitized luminescence

Short-lived fluorescence of matrix proteins and molecules, as well as direct excitation of the acceptor, is significantly diminished after a time delay between excitation of a lanthanide complex donor and recording of acceptor emission.

5.2 Protein kinase A (PKA) in GPCR signaling cascades

We chose the PKA FRET sensor AKAR2CR as a LRET-FRET proof of concept due to the broad importance of PKA in maintaining cellular health¹⁶⁻¹⁹. G-protein coupled receptors (GPCRs), the largest family of cell membrane receptors, are important for signaling in numerous cell types, including communication between neurons via synaptic transmission²⁰. When bound to their respective ligand, $G\alpha_s$ or $G\alpha_i$ coupled GPCRs activate or depress adenylyl cyclase (AC), whose downstream signaling modulates intracellular cyclic adenosine monophosphate (cAMP) levels. In times of increased cAMP concentrations, protein kinase A (PKA) binds two cAMP molecules, inducing a conformational change and freeing catalytic subunits to phosphorylate serine or threonine residues^{19,21}. Interestingly, substrates phosphorylated by PKA are variable, depending on subcellular location, and aberrant function has been implicated in diabetes, cancer and cardiovascular disease²². Therefore, understanding how PKA is localized subcellularly, as well as its substrate discretion is important in understanding broader GPCR and cAMP dependent signaling.

5.3 AKAR2-CR is a well-studied PKA sensor

The FRET-based PKA sensor AKAR2-CR was developed by tethering GFP (Clover) and RFP (mRuby2) fluorescent proteins together via a known PKA substrate sequence and a phosphopeptide binding domain (FHA1)²⁰. Once phosphorylated by PKA, the FHA1 domain binds to the phosphorylated substrate sequence, bringing the two fluorescent proteins in close proximity for FRET to occur (Figure 40). Thus, AKAR2-CR creates a viable PKA sensor that can be used for monitoring PKA activity both *in vitro* and *in vivo*.

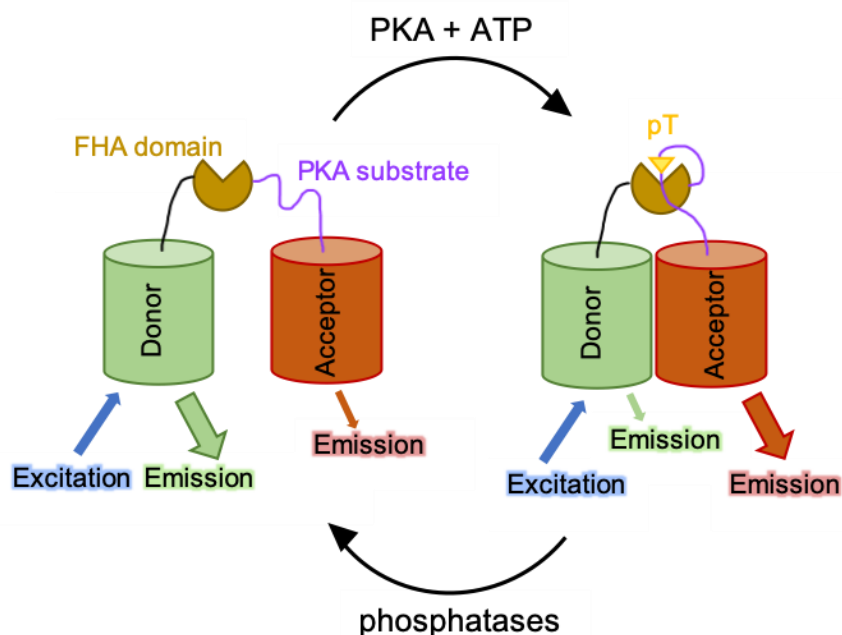


Figure 40 Reporting of PKA activity is possible using the AKAR2-CR FRET sensor. Under conditions of low activity, the PKA substrate is unstructured, resulting in low Clover-mRuby2 FRET. After phosphorylation by PKA, the PKA substrate sequence is bound by FHA1, shifting mRuby2 close to Clover for FRET to occur.

5.4 Engineering an LRET-AKAR2CR luminescent indicator for PKA activity

The terbium luminescence emission overlaps well with the excitation band for green fluorescent proteins, therefore, we sought to convert AKAR2-CR into a LRET sensor by appending an LBT to the GFP donor. We approached this in two steps. First, we established that it is viable to append an LBT to GFP to obtain measurable LRET sensitized emission, and we used this reduced system to choose the optimal LBT. Using the selected LBT, we then tested a proof-of-concept design for a time-resolved PKA sensor by appending the LBT sequence to both the Clover (donor) and mRuby (acceptor) fluorescent proteins of the AKAR2-CR sensor.

5.5 Methods

5.5.1 Materials

Unless otherwise stated, chemicals were purchased from Sigma Aldrich and Fischer Scientific; molecular biology enzymes were purchased from New England Biolabs (NEB). 75 mM ATP stocks in water were made and kept at -80 °C until use. cAMP dependent protein kinase A (PKA), catalytic subunit was purchased from Promega or NEB.

5.5.2 Molecular Biology

Lanthanide binding tag sLBT (YIDTNNDGWYEGDELLA) or dLBT (GPGYIDTNNDGWIEGDELYIDTNNDGWIEGDELLA)

were added to the N, C or both termini of eGFP in a pRsetB vector using the a Q5® Site-Directed Mutagenesis Kit (NEB) with primers found in Table 5. Wild-type (WT) AKAR2-CR was moved to a pRsetB vector from the pcDNA3 mammalian expression vector by PCR, with sLBTa added to the N-terminus of Clover or mRuby2 using primers found in Table 5. Replacement of Clover or mRuby2 with sLBTa was done using Q5® Site-Directed Mutagenesis.

Table 6 LBT FP Primer Design

Construct	Parent Vector	Forward	Reverse
sLBTa-eGFP	pRsetB-eGFP	GTACGAGGGTGACGAGTTGTTGGC AGCGGTGAGTAAGGGCGAGGAG	CAGCCGTCGTTGTTAGTGCAAT GTAGGTGGATCCTTATCGTCAT
sLBTb-eGFP	pRsetB-eGFP	GTACGAAGGTGATGAACTGCTGG CCTAAGAATTCTGAAGCTTGATCCG	CAGCCATCGTTGTTAGTATCAAT GTACTTGACAGCTCGTCCATG
dLBTa-eGFP	pRsetB-eGFP	GACGGCTGGATTGAGGGTGACGA GCTGTACATTGACACTAACCAACG	ATTATTAGTGCAATGTAGCCG GGTCCGGTGGGATCCTTATCGTC
AKAR2- sLBTaCR	pRsetB- AKAR2CR	GTATGAGGGTGAAGAGTTGTT GGCAATGGTGAGCAAGGGCGAG	CAGCCATCGTTGTTAGTGCAATGTA CGGATCCTTATCGTCATCGTC

5.5.3 Protein expression and purification

Plasmids were transformed into BL21(DE3) E. coli cells and grown in Autoinduction Media (Formedium) at 37 °C in baffled flasks with continuous shaking overnight for 12-16 hours followed by two days of continuous shaking at ambient temperatures. Cells were pelleted at 6,000xg and stored at -80 °C until purification. Pellets were resuspended in homogenization buffer (25 mM sodium phosphate, 500 mM NaCl, 10 mM Imidazole, 5% glycerol pH 7.5) and put through two freeze-thaw cycles by snap freezing with dry ice and thawing in a 37°C water bath. After the last thaw at 37°C, 1.0 mg/mL lysozyme, 0.1% Triton-X-100, 1 mM PMSF and 5 mM DTT were added to the suspended cells. The suspension was then rotated at 37°C for 30 minutes, followed by sonication (80% amplitude, 2 s pulse, 2s rest) for 5 minutes. Cellular debris was separated by centrifugation at 30,000xg for 30 minutes. The supernatant was passed through a 0.45µm filter and purified by nickel-affinity chromatography on ÄKTA using a HiTrap IMAC column (Amersham) according to manufacturer instructions. Protein elution was qualitatively determined by ÄKTA and a visible color change in collection tubes. 100 uL of each fraction was checked for peak fluorescence with pooled fractions consisting of greater or equal to 30% of the maximum

fluorescent well. Pooled purified protein was dialyzed against storage buffer (5 mM MOPS, 300 mM NaCl, 10% glycerol, pH 7.3) and concentrated to 500 uL using a 10,000 MWCO Amicon Centrifugal Filter (Millipore). Protein concentrations were determined using the Thermo Scientific™ Pierce™ BCA™ Protein Assay Kit, with mature fluorescent protein concentrations quantified by measuring the absorbance of the protein after 10 minute incubation in 1M NaOH at 450 nm ($44000 \text{ M}^{-1}\text{cm}^{-1}$) as previously described²³. Proteins were stored in 50-150 uL aliquots at -20 °C for immediate use or -80 °C for extended storage. Unless otherwise stated, protein stocks were kept in storage buffer before diluting for assay.

5.5.4 LBT-eGFP Time-Resolved Luminescence Assays

LBT-eGFP protein stocks were diluted to 1 μM in storage buffer with addition of 0, 1, 10, 100 or 1000 μM Terbium Chloride in water in a 96 well black bottom fluorescence plate. Samples were excited with fixed excitation of 280/9 nm using a xenon bulb. Emission measurements were taken between 300/9 nm – 700 nm in 5 nm increments after a 100 us delay (collection time 300 us, gain 100). TR-LRET was determined by the presence of a 510 nm peak, corresponding to eGFP emission. Comparisons were done between all constructs and controls in the presence of 100 μM Terbium Chloride. The LBT peptide [YIDTNNDGWYEGDELLA] was ordered and synthesized by GenScript, DPA and DTPA were both prepared in 1 M stocks with water. All controls were diluted (10 μM peptide, 1 mM DPA/DTPA) and assayed as described above. To test the off-rates of luminescence signal as a function of LBT-Tb³⁺ binding, the lanthanide chelate Diethylenetriaminepentaacetic Acid (DTPA) was prepared in 1 M stocks in water and diluted into LBT-eGFP samples to a final concentration of 10 mM and incubated for 20 minutes.

5.5.5 AKAR2-CR PKA Assay

PKA Assay was developed following manufacturer instruction. 2500 U (1 uL) of Promega cAMP dependent protein kinase (PKA) was added to a reaction containing 1 μM AKAR2-CR and 300 μM ATP in house made assay buffer (40 mM Tris pH 7.4, 20 mM Magnesium Acetate) in black bottom fluorescent 96-well plates. After excitation at 510 nm, emission at 528 nm (clover donor) and 620 nm (mRuby2 acceptor) was recorded every minute for 10 minutes. FRET was determined by dividing the total acceptor fluorescence at 620 nm by the donor fluorescence at 528 nm.

5.6 Results

5.6.1 LBT-eGFP as a TR-LRET model system

A model peptide sequence for lanthanide binding was chosen based on work done by the Imperali group at MIT. Through synthesis and screening of oxygen rich, tryptophan containing peptide sequences, they found that appending the sequence [YIDTNNDGWYEGDELLA] onto non-fluorescent targets such as ubiquitin showed selective and repeatable luminescence while not interfering with the expression, purification using Ni²⁺ resin, or ubiquitin activity *in vitro*¹². Importantly, the tryptophan in the 9th position acts as an ‘antennae’, which overcomes the low molar absorptivity of trivalent cations. Through site-directed mutagenesis we successfully engineered a single LBT tag (sLBT) [YIDTNNDGWYEGDELLA] onto the N (sLBTa) or C (sLBTb) terminus of enhanced green fluorescent protein (eGFP), as well as encoded at both termini simultaneously (sLBTab) (Table 5, Figure 41). By encoding this peptide tag with proven affinity for lanthanides, we hypothesized that after exciting the tryptophan at 280 nm, we would see a relay with non-radiative transfer from tryptophan to terbium to eGFP (Figure 42). The excitation and emission profiles of eGFP are shifted >200 nm from this excitation wavelength, greatly reducing direct eGFP excitation. However, even with a large Stokes shift between donor and acceptor, direct excitation of eGFP is possible due to increased energy of ultra-violet light. Here we hypothesized that the 100 μ s delay between excitation of tryptophan and recording of eGFP emission would greatly reduce any background from eGFP direct excitation, whose lifetime is in the nanosecond range. We then successfully expressed and purified tagged eGFP variants and tested their luminescence properties with increasing concentrations of terbium (0-1000 μ M), excitation at 280nm, and a 100 us delay before data acquisition. Compared to the untagged eGFP control, fluorescence peaks characteristic of eGFP were only present after dosing LBT-tagged constructs with terbium, with the single LBT N-terminal tagged sLBTa-eGFP as the strongest responder (Figure 43). As a control, both the peptide sequence alone, as well as the known terbium chelator dipicolinic acid (DPA) were tested in a similar fashion. Both the peptide and DPA showed expected terbium-chelate emission peaks after excitation by an antennae (490, 545 and 590 nm), however no signal was seen at 510 nm, the expected emission for eGFP (Figure 42). We then tested the luminescence off-rate after challenging terbium bound LBT-eGFP samples with the lanthanide chelator DTPA and recording the decay in gated luminescence every 2 minutes for 20 minutes. For all LBT-eGFP constructs, the signal fell to half-maximal values within the first 2

minutes, with almost no detection of luminescence observed after 16 minutes (Figure 44). We successfully showed LRET to a fluorescent protein target (eGFP) was possible by appending the LBT peptide to either termini, and moved forward with shifting a kinase FRET sensor to a time-resolved reporter.

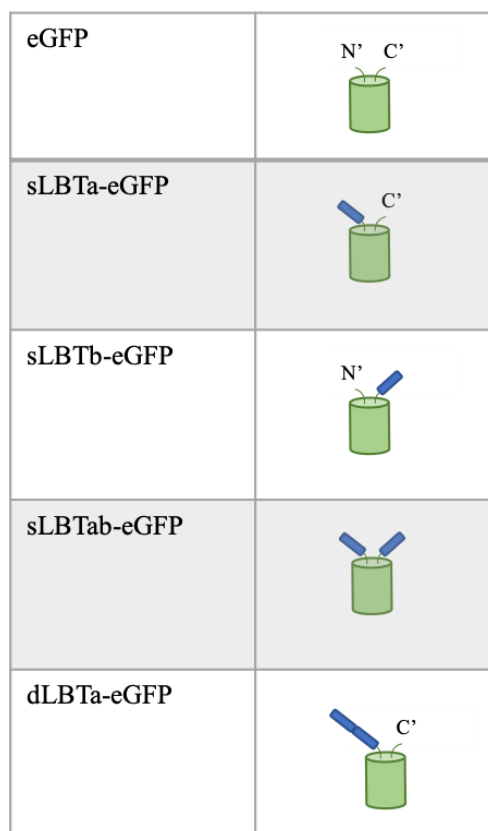


Figure 41 Schematic of LBT-eGFP constructs. We successfully tagged sLBT on the N, C and combined of eGFP, as well as a double lanthanide tag dLBT on the N-terminus of eGFP

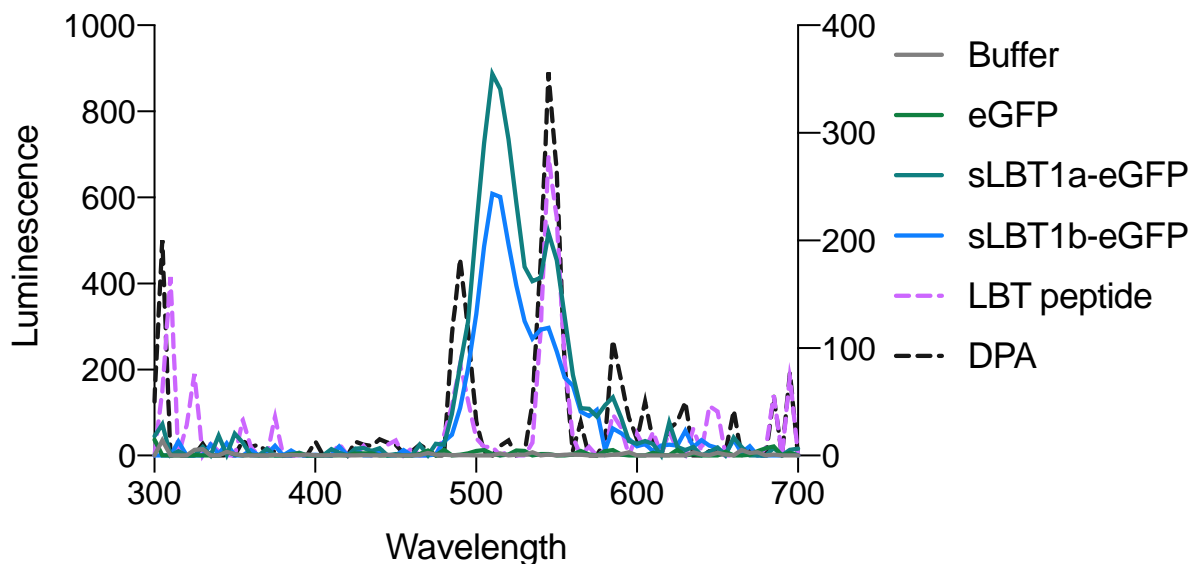


Figure 42 LBT-eGFP gated luminescence

After addition of $100 \mu\text{M Tb}^{3+}$ we saw eGFP emission after 280 nm excitation and 100 us delay on LBT tagged eGFP constructs. Importantly, Tb^{3+} -chelate peaks were also visible in LBT-eGFP constructs, which overlaid with Tb^{3+} -chelate controls Tb^{3+} -DPA and Tb^{3+} bound to LBT peptide alone

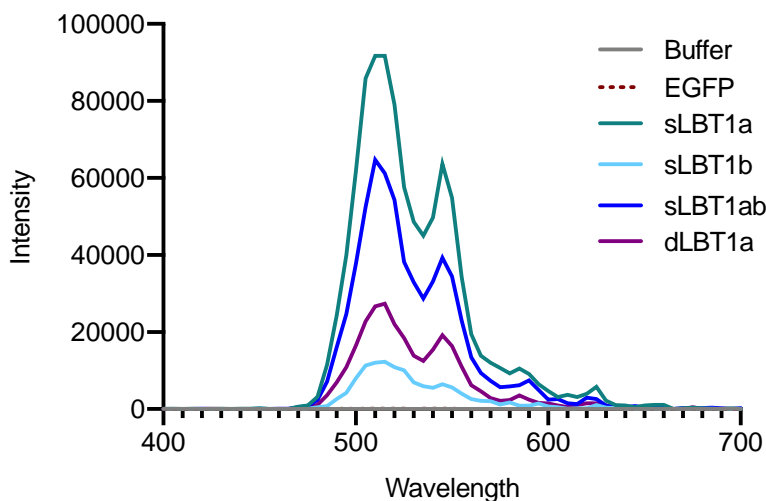


Figure 43 LBT-eGFP *in vitro* testing

Time-resolved spectroscopy of LBT-eGFP constructs overlaid for comparison after addition of $100 \mu\text{M}$ Terbium, excited at 280 nm and emission reading gated for 100 us. Importantly, eGFP control (green) shows no visible emission, while all LBT tagged constructs display LRET, with sLBTa-eGFP (single N-terminal tagged) producing strongest TR-LRET signal.

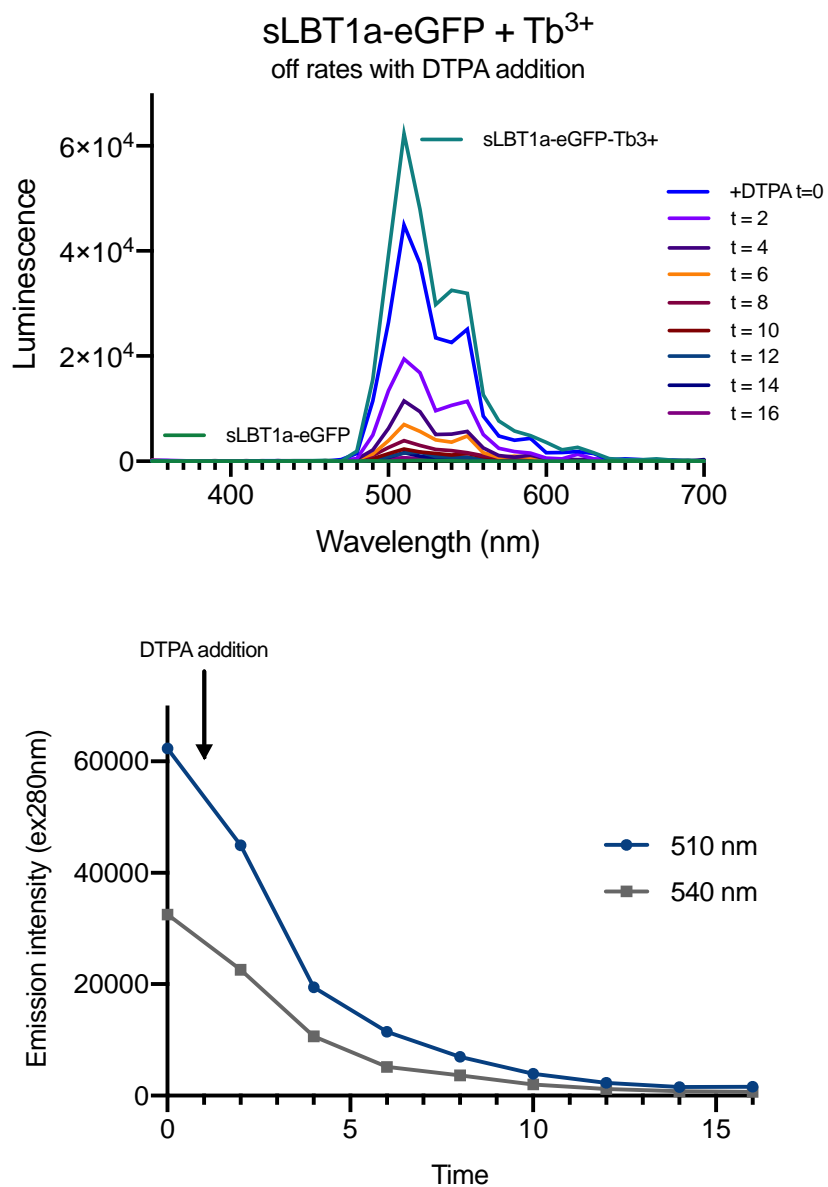


Figure 44 sLBTa-eGFP off-rates after addition of lanthanide chelator DTPA
Almost immediately after addition of 10 mM DTPA a decrease in time-gated eGFP emission was noticeable, with a four-fold signal decrease after 4 minutes incubation.

5.7 LBT-AKARCR as proof-of-concept

Terbium emission overlaps with both GFP and RFP excitation bands but is distinct from the GFP and RFP emission bands (Figure 45). After robust and repeatable detection of Tb³⁺-LBT LRET using a sLBTa-eGFP model, we moved forward with molecular biology strategies to append the LBT sequence on the N-terminus of either Clover (donor) or mRuby2 (acceptor) proteins (Figure 40) of the FRET PKA sensor AKAR2-CR. We also engineered a replacement approach, by placing the LBT sequence in lieu of either the Clover or mRuby2 proteins (Table 6).

We first wanted to demonstrate we could determine kinase activity in an *in vitro* assay following an established Promega protocol²⁴. After acquiring the catalytic domain of cAMP dependent protein kinase A (PKA), we prepared a buffer in-house according to manufacturer's instructions and made several attempts at replicating an AKAR2-CR FRET response in the presence of PKA and ATP. We first saw successful FRET in both phosphate and Tris buffering systems, although only when adding ATP before PKA (Figure 46). Moving forward with LBT tagged AKAR2-CR variants, we first tested LRET efficiency with increasing amounts of terbium in the presence of Tris buffer. We were able to see distinct Clover emission peaks in both the wild type and sLBTa tagged AKAR2CR, with a broad ~600 nm peak possibly indicative of mRuby2 emission (Figure 47-48). Interestingly, we saw distinctly stronger Clover and mRuby2 emission after 100 μ s delay in the LBT tagged AKAR2CR construct, however, this was only apparent in Tris buffering conditions. When we moved into PKA assay buffer, precipitation was noticed in well within minutes of terbium addition. Qualitatively, it appeared precipitation was less pronounced in wells containing the LBT tagged constructs, which could be due to chelation of terbium by the tag, decreasing excess concentrations which could be responsible for precipitation. Although several constructs were designed and made to test location of the LBT tag on the AKAR2CR construct (Table 6), the incompatibility of the LRET assay in simple kinase buffer and the unduly complex LRET sensitized emission spectra ultimately led to the termination of the project.

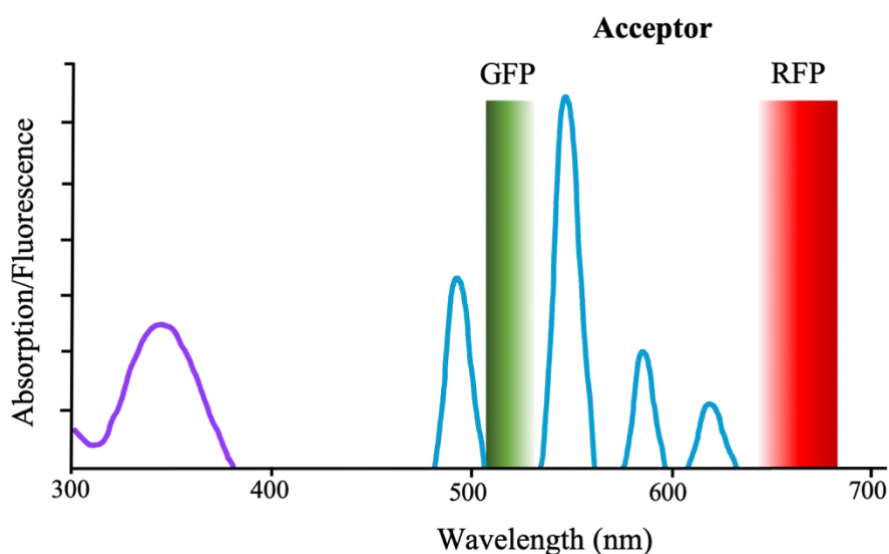


Figure 45 LBT-Tb³⁺ as a FRET donor

After excitation in the UV, the chelated terbium emits distinct peaks with narrow bandwidths at 490, 545, 590 and 615 nm. These long-lived emissions span across the visible range, allowing for spectral overlap with fluorescent proteins as potential luminescence resonance energy transfer (LRET) pairs.

Table 7 LBT AKAR2CR construct design

<i>Construct</i>	<i>Donor</i>	<i>Acceptor</i>
<i>AKAR2CR</i>	Clover	mRuby2
<i>AKAR2 sLBTaCR</i>	sLBTa-Clover	mRuby2
<i>AKAR2CsLBTaR</i>	Clover	sLBTa-mRuby2
<i>AKAR2CsLBTa</i>	Clover	sLBTa
<i>AKAR2sLBTaR</i>	sLBTa	mRuby2

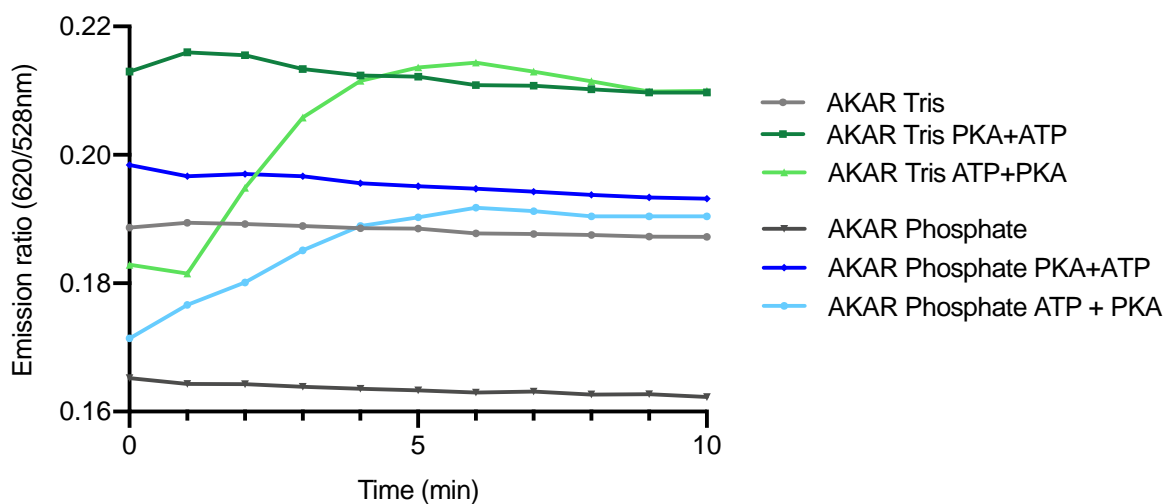


Figure 46 In vitro PKA assay with purified wild-type AKAR2-CR FRET sensor
Only after addition of ATP before PKA do we see an increase in mRuby2 fluorescence as a result of FRET.

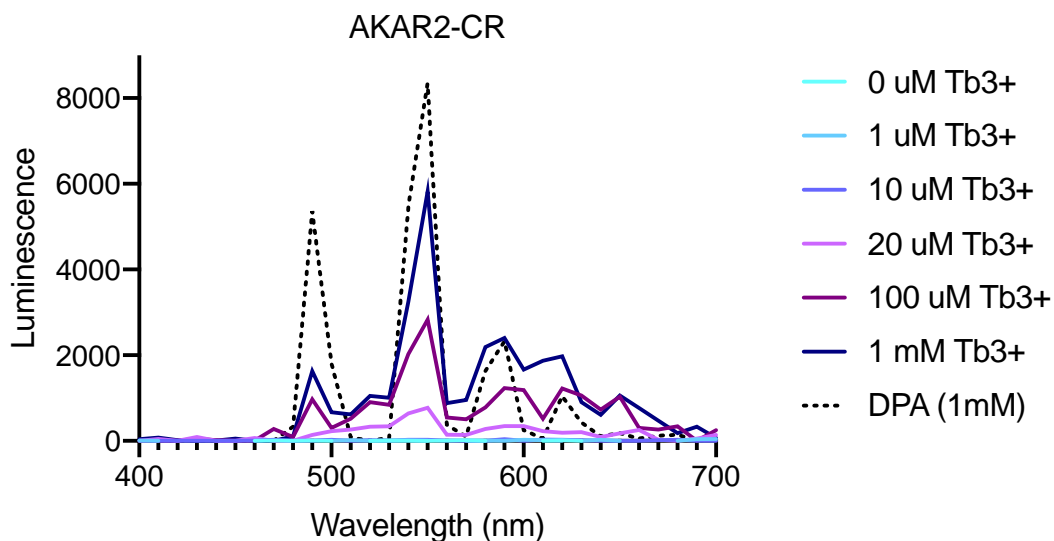


Figure 47 Wild type AKAR2CR LRET in Tris buffer
With the addition of Terbium, distinct long-lived Terbium luminescence is seen, with no indication of clover or mRuby2 emission.

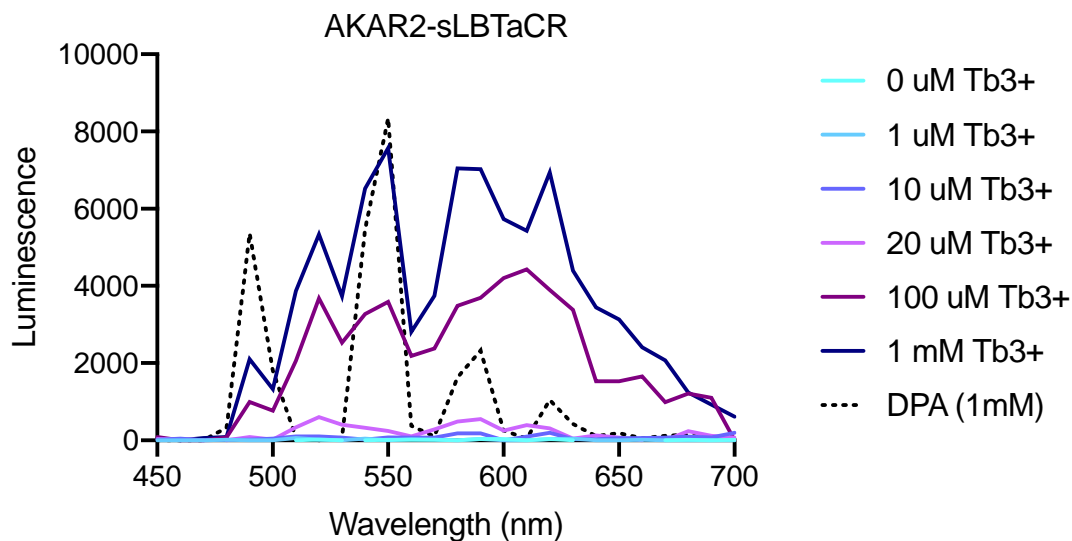


Figure 48 AKAR2-sLBTaCR LRET in Tris buffer

With the addition of the sLBTa tag (single, N-terminal tag) onto the N terminus of Clover, we see increasing 510 nm gated emission with increasing Terbium concentrations. A broad peak ~600 nm gain intensity with increasing terbium, which could be indicative of mRuby2 emission.

5.8 Conclusions

Using a GFP model, we appended an LBT peptide to the N and/or C terminus of eGFP, as well as a double LBT to the N-terminus. We were able to see Terbium dependent time gated luminescence of GFP in all constructs, with greatest LRET observed with the N-terminal tagged eGFP construct sLBTa-eGFP. We then decided to move forward utilizing the well-studied PKA FRET sensor AKAR2-CR for LRET PKA sensing by adding the sLBTa sequence to the N-terminus of Clover (donor) or mRuby2 (acceptor), as well as replacing either fluorescent protein with the sLBTa peptide sequence. After verifying wild-type AKAR2-CR sensitivity to PKA activity using a well-defined *in vitro* PKA assay, we were unable to reliably determine fluorescence or luminescence of constructs after the addition of terbium due to precipitation in wells. The inability to use the LBT-AKAR2-CR constructs in a simple *in vitro* assay, as well as the rapid off-rate kinetics of LBT-Tb³⁺ in the presence of a chelator, ultimately led to the decision to terminate the project.

5.9 References

1. Croce, A. C. & Bottiroli, G. New light in flavin autofluorescence. *Eur. J. Histochem.* (2015). doi:10.4081/ejh.2015.2576
2. Rocheleau, J. V., Head, W. S. & Piston, D. W. Quantitative NAD(P)H/flavoprotein autofluorescence imaging reveals metabolic mechanisms of pancreatic islet pyruvate response. *J. Biol. Chem.* (2004). doi:10.1074/jbc.M314005200
3. Höferl, M., Krist, S. & Buchbauer, G. Adaptation of DELFIA™ cortisol kit for determination of salivary cortisol concentration. *Arch. Pharm. (Weinheim)*. (2005). doi:10.1002/ardp.200500116
4. Meyer, J. & Karst, U. Enzyme-linked immunosorbent assays based on peroxidase labels and enzyme-amplified lanthanide luminescence detection. *Analyst* (2001). doi:10.1039/b008293g
5. Selvin, P. R. Principles and Biophysical Applications of Lanthanide-Based Probes. *Annu. Rev. Biophys. Biomol. Struct.* (2002). doi:10.1146/annurev.biophys.31.101101.140927
6. Bünzli, J. C. G. Lanthanide luminescence for biomedical analyses and imaging. *Chem. Rev.* (2010). doi:10.1021/cr900362e
7. Karvinen_2002_Homogeneous Time-Resolved Fluorescence Quenching Assay (LANCE) for Caspase-3.pdf.
8. Mathis, G. HTRF® technology. *Journal of Biomolecular Screening* (1999). doi:10.1177/108705719900400605
9. Zwier, J. M. *et al.* A fluorescent ligand-binding alternative using tag-lite technology. *J. Biomol. Screen.* **15**, 1248–1259 (2010).
10. Sculimbrene, B. R. & Imperiali, B. Lanthanide-binding tags as luminescent probes for studying protein interactions. *J. Am. Chem. Soc.* **128**, 7346–7352 (2006).
11. Rajendran, M., Yapici, E. & Miller, L. W. Lanthanide-based imaging of protein-protein interactions in live cells. *Inorganic Chemistry* (2014). doi:10.1021/ic4018739
12. Franz, K. J., Nitz, M. & Imperiali, B. Lanthanide-binding tags as versatile protein coexpression probes. *ChemBioChem* **4**, 265–271 (2003).
13. Bünzli, J.-C. G. & Eliseeva, S. V. Basics of Lanthanide Photophysics. in (2010). doi:10.1007/4243_2010_3
14. Wu, Q. *et al.* A cell-penetrating protein designed for bimodal fluorescence and magnetic resonance imaging. *Chem. Sci.* **6**, 6607–6613 (2015).

15. Rajapakse, H. E. & Miller, L. W. Time-resolved luminescence resonance energy transfer imaging of protein-protein interactions in living cells. *Methods Enzymol.* (2012). doi:10.1016/B978-0-12-388448-0.00025-5
16. Skeberdis, V. A. *et al.* Protein kinase A regulates calcium permeability of NMDA receptors. *Nat. Neurosci.* (2006). doi:10.1038/nn1664
17. Deming, P. B., Campbell, S. L., Baldor, L. C. & Howe, A. K. Protein kinase A regulates 3-phosphatidylinositide dynamics during platelet-derived growth factor-induced membrane ruffling and chemotaxis. *J. Biol. Chem.* (2008). doi:10.1074/jbc.M804448200
18. Goto, A., Kamioka, Y. & Matsuda, M. PKA modulation of Rac in neuronal cells. *Front. Cell. Neurosci.* (2014). doi:10.3389/fncel.2014.00321
19. Isobe, K. *et al.* Systems-level identification of PKA-dependent signaling in epithelial cells. *Proc. Natl. Acad. Sci.* (2017). doi:10.1073/pnas.1709123114
20. Chen, Y., Saulnier, J. L., Yellen, G. & Sabatini, B. L. A PKA activity sensor for quantitative analysis of endogenous GPCR signaling via 2-photon FRET-FLIM imaging. *Front. Pharmacol.* **5**, 56 (2014).
21. Manni, S., Mauban, J. H., Ward, C. W. & Bond, M. Phosphorylation of the cAMP-dependent protein kinase (PKA) regulatory subunit modulates PKA-AKAP interaction, substrate phosphorylation, and calcium signaling in cardiac cells. *J. Biol. Chem.* (2008). doi:10.1074/jbc.M802278200
22. Liao, J. J.-L. Molecular Recognition of Protein Kinase Binding Pockets for Design of Potent and Selective Kinase Inhibitors. *J. Med. Chem.* (2007). doi:10.1021/jm0608107
23. Tantama, M., Hung, Y. P. & Yellen, G. Imaging intracellular pH in live cells with a genetically encoded red fluorescent protein sensor. *J. Am. Chem. Soc.* **133**, 10034–10037 (2011).
24. Chang, Y. F. & Carman, G. M. Casein kinase II phosphorylation of the yeast phospholipid synthesis transcription factor Opi1p. *J. Biol. Chem.* (2006). doi:10.1074/jbc.M513064200